MONTHLY WEATHER REVIEW

VOLUME 93, NUMBER 12

DECEMBER 1965

NUMERICAL RESULTS FROM A NINE-LEVEL GENERAL CIRCULATION MODEL OF THE ATMOSPHERE[1]

JOSEPH SMAGORINSKY, SYUKURO MANABE, and J. LEITH HOLLOWAY, Jr.

Geophysical Fluid Dynamics Laboratory, Environmental Science Services Administration, Washington, D.C.

ABSTRACT

The "primitive equations of motion" are adopted for this study. The nine levels of the model are distributed so as to resolve surface boundary layer fluxes as well as radiative transfer by ozone, carbon dioxide, and water vapor. The lower boundary is a kinematically uniform land surface without any heat capacity. The stabilizing effect of moist convection is implicitly incorporated into the model by requiring an adjustment of the lapse rate whenever it exceeds the moist adiabatic value. The numerical integrations are performed for the mean annual conditions over a hemisphere starting with an isothermal atmosphere at rest. The spatial distribution of gaseous absorbers is assumed to have the annual mean value of the actual atmosphere and to be constant with time.

A quasi-equilibrium is attained about which a cyclic energy variation occurs with an irregular period of about 2 weeks. The dominant wave number of the meridional component of the wind is 5 to 6 in the troposphere but is reduced to about 3 in the stratosphere. The gross structure and behavior of the tropopause and stratosphere below 30 km. agree reasonably well with observation. The meridional circulation obtained from the computation has a 3-cell structure in the troposphere and tends toward a 2-cell structure with increasing altitude in the stratosphere. Although the level of the jet stream as well as that of the maximum northward transport of momentum coincides with observation, the intensity of the jet stream turns out to be much stronger than the observed annual mean. In the stratosphere the temperature increases with increasing latitude because of the effect of large-scale motion. The magnitude of the increase, however, is smaller than that observed.

A detailed study of the vertical distribution of the budget of kinetic energy, of available potential energy, of heat, and of angular momentum is made. The mechanism for maintaining the kinetic energy of the jet stream and of the stratosphere is discussed. It is concluded that in the model the kinetic energy in the stratosphere is maintained against its conversion into potential energy and dissipation through interaction with the troposphere, which is in qualitative agreement with the results derived from an analysis of the actual atmosphere. In the troposphere, the conversion of potential energy reaches a maximum at about the 500-mb. level. This energy is then transferred to the level of the jet stream and to the surface boundary layer by the so-called pressure interaction term, thus providing the source of kinetic energy for these two levels at which dissipation is predominant. As with the results of Phillips [27] and Smagorinsky [37], the ratio of eddy kinetic energy to zonal kinetic energy and that of eddy to zonal available potential energy are computed to be much smaller than those of the actual atmosphere.

[1] Preliminary results of this investigation were first presented at the International Symposium on Dynamics of Large-Scale Processes, Boulder, Colo., September 3–7, 1963.

CONTENTS

1. INTRODUCTION

The work to be reported upon in this paper represents the results of the initial phase of a comprehensive long-term research program in the dynamics of the general circulation. This program, conceived in its present form in 1958, is a natural outgrowth of the two principal antecedents: (1) Phillips's [27] two-level quasi-geostrophic model in a zonally periodic domain on a β-plane, which initially demonstrated the feasibility of numerically simulating the general circulation, and (2) Smagorinsky's [37] primitive equation two-level model with motion within a spherical zonal strip, which considerably generalized the hydrodynamic framework. These models have already provided extremely useful information regarding our ability to simulate some of the important gross properties of the general circulation and the processes by which they are maintained.

Both of these models had in common the gross oversimplification of the vertical structure of the atmosphere and all that it implies; namely, the necessity for strong parameterization of the planetary boundary layer, the radiative transfer, convective transfer, and the vertical static stability. The role of fronts was highly oversimplified, and the effects of the tropopause and the stratosphere were ignored. The interaction of the hydrologic cycle was for the most part also ignored.

The ultimate objective of this work is to understand the basic mechanisms responsible for maintaining the general circulation and the climatology of the atmosphere and to simulate the essential (macroscopic) features of the general circulation with a minimum of parametric constraints. It was, however, apparent that such a complete step at the outset would inevitably end in failure and would only be unraveled by going back to less complex versions. The strategy adopted anticipated such difficulties and took a long-range view. We first constructed with considerable care, and in fact programed, the most general of a hierarchy of models in order to uncover in some detail the body of physics needed, to determine where the obvious weaknesses were, and to give us some idea of the computational limitations we could expect. The perspective thus gained was invaluable. We then laid out a program of simplified models which can be constructed as a sub-set of the most general one. The main requirements were (1) that each model represent a physically realizable state, (2) that they could be constructed computationally by program bypasses, and (3) that they collectively would provide a step-by-step study of the behavior of new processes and their influence on the interactive system. Hence, many of the intermediate models in themselves may lack detailed similitude to the atmosphere but provide the insight necessary for careful and systematic scientific inquiry.

In this connection we have carried from our previous experience the practice of performing comprehensive dynamic diagnoses of the balances of energy, heat, and angular momentum. Although this requires what may appear to be an inordinate and incongruous effort, we feel that the apparent simulation of the synoptic manifestations does not in itself constitute an understanding. It is not inconceivable that the results superficially may be correct but for the wrong reason. Diagnostic integral techniques provide a very sensitive measure of the mechanistic similitude of the model to the atmosphere. In our view they provide the type of insight from numerical studies that one normally expects to derive from analytical studies.

An important characteristic of this model lies in the

computation of radiative transfer. It is clear that a simple parameterization of the calculation of radiative transfer requires that we implicitly presume a knowledge of the vertical thermal structure of the real atmosphere. To avoid the parameterization, we decided to compute the radiative flux as a function of an arbitrary vertical distribution of the atmospheric absorbers, such as water vapor, carbon dioxide, and ozone. For the sake of simplicity of computation we adopted a scheme which requires the results of low resolution measurements of absorptivity. Preceding the present study, extensive computations of thermal equilibrium were carried out by the use of this scheme. Refer to Manabe and Strickler [17] for the detailed description of these calculations.

One of the most important factors which influences, if not controls, the general circulation of the atmosphere is the process of condensation. The explicit incorporation of this process into the general circulation model, however, initially overcomplicates the scheme a great deal and makes the analysis of results more difficult. Therefore, we have introduced a simple process of moist convective adjustment as a substitute for the moist convection, the adjustment being carried out whenever the lapse rate exceeds the moist adiabatic value. It must be kept in mind, however, that although this process roughly corresponds to the stabilizing effect of moist convection, it does not simulate the northward transport of latent energy which could be of major importance. Therefore, this numerical study could be regarded as an intermediate step before we attempt to study the behavior of a more general model involving the process of condensation. We shall discuss the results obtained from the time integration of the general circulation with the hydrologic cycle in a paper which follows [18].

In dealing with a lower boundary of uniform heat capacity, there are two extreme choices in simulating the thermal properties. One can choose an ocean-covered earth of infinite heat capacity for which one must specify the quasi-equilibrium surface temperature. In this case, the temperature specified at the ocean boundary would all but control the latitudinal temperature gradient of the atmosphere by convection.

Another choice for the uniform lower boundary condition is a land surface with no heat capacity. In this case, the temperature of the earth's surface is determined by the heat balance among solar radiation, long-wave radiation, and the turbulent flux of energy from the earth's surface to the atmosphere. By adopting this lower boundary condition, we implicitly neglect the effect of the heat transport by ocean currents. The numerical experiment with this boundary condition constitutes a logical step before the study of the model with the effect of energy transport by ocean currents. Therefore, we adopted this latter boundary condition for the present study.

It was our intention to permit sufficient vertical resolution to:

(1) make unnecessary the Ekman approximation between the lowest level and the earth's surface—namely, the boundary layer is thin enough so that the rotational forces may be assumed negligible with respect to the viscous forces,

(2) have the upper level high enough to represent the main ultraviolet absorption of ozone,

(3) describe the gross thermal structure of the tropopause and stratosphere, and

(4) provide tropospheric resolution great enough to account for the major role of frontal dynamics and of condensation processes to be incorporated later.

2. SYSTEM OF PROGNOSTIC EQUATIONS

A. DYNAMIC AND THERMODYNAMIC EQUATIONS

Adopting pressure normalized by surface pressure as the vertical coordinate, we write the equations of motion on the stereographic map projection as follows (refer to the papers by Phillips [28], [30]):

$$\frac{\partial(P_*U)}{\partial t}=-m^2\left[\frac{\partial}{\partial X}\left(\frac{P_*U^2}{m}\right)+\frac{\partial}{\partial Y}\left(\frac{P_*UV}{m}\right)\right]-P_*\frac{\partial(\dot{Q}U)}{\partial Q}$$
$$+\left[2\Omega\sin\theta-\frac{1}{2a^2}(VX-UY)\right]P_*V$$
$$-mP_*\frac{\partial\phi}{\partial X}-mRT\frac{\partial P_*}{\partial X}+{}_HF_X+{}_VF_X \qquad (2A1)$$

$$\frac{\partial(P_*V)}{\partial t}=-m^2\left[\frac{\partial}{\partial X}\left(\frac{P_*UV}{m}\right)+\frac{\partial}{\partial Y}\left(\frac{P_*V^2}{m}\right)\right]-P_*\frac{\partial(\dot{Q}V)}{\partial Q}$$
$$-\left[2\Omega\sin\theta-\frac{1}{2a^2}(VX-UY)\right]P_*U$$
$$-mP_*\frac{\partial\phi}{\partial Y}-mRT\frac{\partial P_*}{\partial Y}+{}_HF_Y+{}_VF_Y \qquad (2A2)$$

The continuity equation is:

$$\frac{\partial P_*}{\partial t}=-m^2\left[\frac{\partial}{\partial X}\left(\frac{P_*U}{m}\right)+\frac{\partial}{\partial Y}\left(\frac{P_*V}{m}\right)\right]-P_*\frac{\partial\dot{Q}}{\partial Q} \qquad (2A3)$$

The hydrostatic equation combined with the equation of state is:

$$\frac{\partial\phi}{\partial Q}=-\frac{RT}{Q} \qquad (2A4)$$

The thermodynamical energy equation is:

$$\frac{\partial(P_*T)}{\partial t}=-m^2\left[\frac{\partial}{\partial X}\left(\frac{P_*UT}{m}\right)+\frac{\partial}{\partial Y}\left(\frac{P_*VT}{m}\right)\right]$$
$$-P_*\frac{\partial(\dot{Q}T)}{\partial Q}+\frac{R}{c_p}\cdot\frac{T\omega}{Q}+F_T+\frac{P_*\dot{q}}{c_p} \qquad (2A5)$$

The notations used in these equations are as follows:

X abscissa of stereographic rectangular coordinate
Y ordinate of stereographic rectangular coordinate
t time
U earth velocity component in X-direction

V earth velocity component in Y-direction
P atmospheric pressure
P_* atmospheric pressure at the lower boundary
T temperature
ϕ geopotential height of Q-surface
Q P/P_* (P: pressure) (see section 5 for definition of Q-level spacing)
$\dot{Q}$ dQ/dt
ω dP/dt
θ latitude
m map scale factor for stereographic projection
$\dot{q}$ rate of non-adiabatic heating
$\frac{{}_HF_X}{P_*}, \frac{{}_HF_Y}{P_*}$ rate of momentum changes due to Reynolds stress in the X- and Y-directions
$\frac{F_T}{P_*}$ rate of temperature change due to lateral subgrid-scale diffusion of heat
R gas constant of air
c_p specific heat of air at constant pressure
a radius of earth
Ω angular velocity of earth
$\frac{{}_VF_X}{P_*}, \frac{{}_VF_Y}{P_*}$ rate of momentum changes in the X- and Y-directions due to vertical diffusion

B. SUBGRID-SCALE MIXING

The momentum change due to the Reynolds stress and the temperature change due to subgrid-scale mixing may be separated into two parts, i.e.,

$$\mathbf{F}={}_H\mathbf{F}+{}_V\mathbf{F} \tag{2B1}$$

$$F_T={}_HF_T+{}_VF_T \tag{2B2}$$

where subscripts H and V denote the contribution of horizontal diffusion and vertical mixing, respectively. According to Smagorinsky [37], the non-linear lateral diffusion may be formulated on the basis of Heisenberg's similarity hypothesis. If we ignore the density variation on the constant Q-coordinate surface, we may take the viscous force due to lateral stress and the temperature change due to lateral diffusion to be

$${}_HF_X=m^3\left[\frac{\partial}{\partial X}\left(\frac{P_*K_HD_T}{m^2}\right)+\frac{\partial}{\partial Y}\left(\frac{P_*K_HD_S}{m^2}\right)\right] \tag{2B3}$$

$${}_HF_Y=m^3\left[\frac{\partial}{\partial X}\left(\frac{P_*K_HD_S}{m^2}\right)-\frac{\partial}{\partial Y}\left(\frac{P_*K_HD_T}{m^2}\right)\right] \tag{2B4}$$

$${}_HF_T=m^2P_*^\kappa\left[\frac{\partial}{\partial X}\left(P_*K_H\frac{\partial(T/P_*^\kappa)}{\partial X}\right)+\frac{\partial}{\partial Y}\left(P_*K_H\frac{\partial(T/P_*^\kappa)}{\partial Y}\right)\right] \tag{2B5}$$

where

$$D_T=\frac{\partial(mU)}{\partial X}-\frac{\partial(mV)}{\partial Y} \tag{2B6}$$

$$D_S=\frac{\partial(mV)}{\partial X}+\frac{\partial(mU)}{\partial Y} \tag{2B7}$$

$$K_H=2k_0^2\left(\frac{\Delta}{2m}\right)^2|D| \tag{2B8}$$

$$\kappa=R/c_p \tag{2B9}$$

In this equation, $|D|$ is the total deformation defined by

$$|D|=(D_T^2+D_S^2)^{1/2} \tag{2B10}$$

Δ is the grid length; k_0 is a non-dimensional parameter of order unity analogous to the Karman constant and is taken to be 0.4 in this paper. The frictional force due to vertical mixing is

$$\frac{{}_V\mathbf{F}}{P_*}=\frac{1}{\rho}\frac{\partial{}_V\boldsymbol{\tau}}{\partial Z}=-\frac{g}{P_*}\frac{\partial{}_V\boldsymbol{\tau}}{\partial Q} \tag{2B11}$$

where ρ and g are the density of air and the acceleration of gravity respectively. Based upon the mixing length hypothesis applied to the boundary layer, the upward flux of momentum is computed by using

$${}_V\boldsymbol{\tau}=\rho K_V\frac{\partial\mathbf{V}}{\partial Z} \tag{2B12}$$

and

$$K_V=l^2\left|\frac{\partial\mathbf{V}}{\partial Z}\right| \tag{2B13}$$

where l is the mixing length. As Rossby and Montgomery [32] suggested, we assumed the following simple law for the vertical variation of l:

$$l=k_0(Z+Z_0) \qquad Z\leq h \tag{2B14}$$

$$l=k_0(h+Z_0)\cdot\frac{H-Z}{H-h} \qquad h\leq Z\leq H \tag{2B15}$$

$$l=0 \qquad H\leq Z \tag{2B16}$$

where the roughness parameter $Z_0=1$ cm. According to Rossby and Montgomery [33], the thickness of the logarithmic boundary layer, h, is 50 to 100 m. In this experiment $h=75$ m. and $H=2.5$ km.

The upward flux of momentum ${}_V\boldsymbol{\tau}$ and heat ${}_VH$ at the earth's surface are

$$({}_V\boldsymbol{\tau})_{Q=1}=-\rho(h)\cdot C_D(h)\cdot|\mathbf{V}(h)|\cdot\mathbf{V}(h) \tag{2B17}$$

$$({}_VH)_{Q=1}=\rho(h)\cdot c_p\cdot C_D(h)\cdot|\mathbf{V}(h)|\cdot[T_*-T(h)/Q^\kappa(h)] \tag{2B18}$$

where C_D is the drag coefficient at the ground surface and is given by

$$C_D\equiv\left(k_0/\log_e\left(\frac{h}{Z_0}\right)\right)^2 \tag{2B19}$$

and T_* is the temperature of the earth's surface. Since the height of the lowest level of our model is designed to be 75 m., these fluxes are a function of the velocity and the temperature of this level. In order to incorporate the effect of free convection, a very large value of C_D is adopted

for the computation of vertical heat flux, $({}_{V}H)_{Q=1}$, when the stratification is unstable. The large coefficient prevents the large temperature gradient at the earth's surface which otherwise appears in lower latitudes.

C. BOUNDARY CONDITIONS

(1) *Lateral Boundary Conditions.*—At the lateral boundary, an insulated free-slip wall is assumed to exist. In other words, the exchange of momentum and heat with the equatorial boundary is zero and

$$V_n=0, \tag{2C1}$$

where V_n is the component of the wind normal to the wall.

(2) *Vertical Boundary Conditions.*—At the top and bottom of the atmosphere, the vertical Q-velocity is zero, i.e.,

$$\dot{Q}=0 \text{ at } Q=0, 1 \tag{2C2}$$

Also, at the top of the atmosphere, the vertical flux of momentum due to subgrid-scale mixing is zero, i.e.,

$$({}_{V}\tau)_{Q=0}=0 \tag{2C3}$$

This condition is automatically satisfied by applying equation (2 B 16).

The specification of ${}_{V}\tau$ and ${}_{V}H$ at the earth's surface ($Q=1$) has already been done in section B.

(3) *Boundary Condition for Radiative Transfer.*—At the top of the atmosphere, the downward long-wave radiation is assumed to be zero, and a solar constant of 2 ly./min. is adopted.

At the bottom of the atmosphere, the temperature of the earth's surface, T_*, is determined such that it satisfies the requirement of the heat balance at the earth's surface. If we assume that the heat capacity of the earth is zero, the balance equation of heat is

$$S_*+(DLR)_*=\sigma T_*^4+({}_{V}H)_{Q=1} \tag{2C4}$$

where S_* and $(DLR)_*$ are the net downward solar insolation and the downward long-wave radiation at the earth's surface, respectively, and σ is the Stefan-Boltzman constant. The solution of this equation yields a T_* which satisfies the heat balance condition at the earth's surface. Since we have eliminated the daily variation of temperature from our model by adopting the effective mean zenith angle of the sun, the assumption of no downward conduction into the soil may not produce any serious difficulties.

D. MOIST CONVECTIVE ADJUSTMENT

As explained in the introduction, we avoided the explicit incorporation of the condensation process for the sake of simplicity of the model. A complete lack of the condensation process, however, would make the atmospheric static stability too unrealistically unstable to compare the results of the experiment with geophysical data. In order to simulate the stabilizing effect of moist convection as simply as possible, a convective adjustment of the lapse rate to a critical value was made whenever the lapse rate exceeded that value, with the requirement that the total potential energy be unaltered. Implicitly, it is assumed that the kinetic energy of moist convective eddies produced as a result of the overturning of air is dissipated into heat as soon as it is produced. The moist-adiabatic lapse rate, which is dependent upon the ambient temperature of the air, is adopted as the critical lapse rate for the adjustment. It must be emphasized that, in the present model, the effect of lateral transport of latent energy is completely neglected. Refer to reference [18] in which this effect is incorporated by making the mixing ratio of water vapor an independent variable of the model.

E. RADIATIVE TRANSFER

The temperature change due to radiative transfer is computed as a function of the vertical distribution of atmospheric absorbers as well as of temperature. The atmospheric absorbers which are taken into consideration are water vapor, carbon dioxide, ozone, and clouds. For simplicity of computation, low resolution measurements of band absorptivity are used instead of the line intensity data. The details of the computation scheme have been described previously by Manabe and Strickler [17]. Hence only a brief outline of the computation method is given here.

In the thermodynamical equation, the heat source term $\dot{q}$ may be separated into three parts, i.e.:

$$\dot{q}=\dot{q}_{LR}+\dot{q}_{SR}+\dot{q}_{C} \tag{2E1}$$

where $\dot{q}_{SR}$ and $\dot{q}_{LR}$ are the heating due to the absorption of solar radiation and of long-wave radiation, respectively; and $\dot{q}_{C}$ is the heating due to condensation. (In this study we do not incorporate the effect of $\dot{q}_{C}$ explicitly. Instead, we adopted the simple process of moist-convective adjustment which was described in section 2D.) $\dot{q}_{LR}$ is computed by use of the following equation:

$$\dot{q}_{LR}=\frac{g}{P_*}\frac{\partial F_Q}{\partial Q} \tag{2E2}$$

where F_Q is the net upward flux of long-wave radiation at level Q and is obtainable as a function of the vertical distribution of absorbers and temperature. $\dot{q}_{SR}$ is represented by:

$$\dot{q}_{SR}=-\frac{g}{P_*}\left[\frac{\partial S_Q}{\partial Q}-\frac{\partial RS_Q}{\partial Q}\right] \tag{2E3}$$

where S_Q is the downward insolation at level Q, and RS_Q is the reflected upward solar radiation at the same level. In order to avoid the complication in the heat balance of the earth's surface due to the daily variation of solar insolation, it was assumed that the zenith angle of the sun is constant with time. The effective mean cosine of the zenith angle ζ is computed by

$$\overline{\cos\zeta}=\left(\int^{Daytime}\cos\zeta dt\right)\Big/\int^{Daytime}dt \tag{2E4}$$

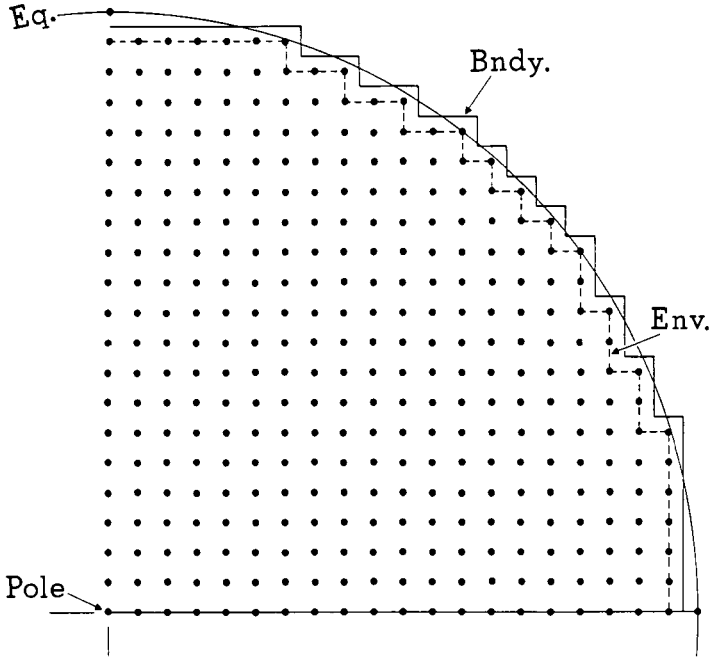

FIGURE 2F1.—Map of the grid points on which the computations were performed showing one quarter of the stereographic projection plane of the Northern Hemisphere ($N=20$). The free-slip, insulated boundary (Bndy.) is located one-half-grid-point distance outside the envelope (Env.) of the southernmost grid points in the Northern Hemisphere, not including the four points on the Equator (Eq.) at the intersections of the coordinate axes.

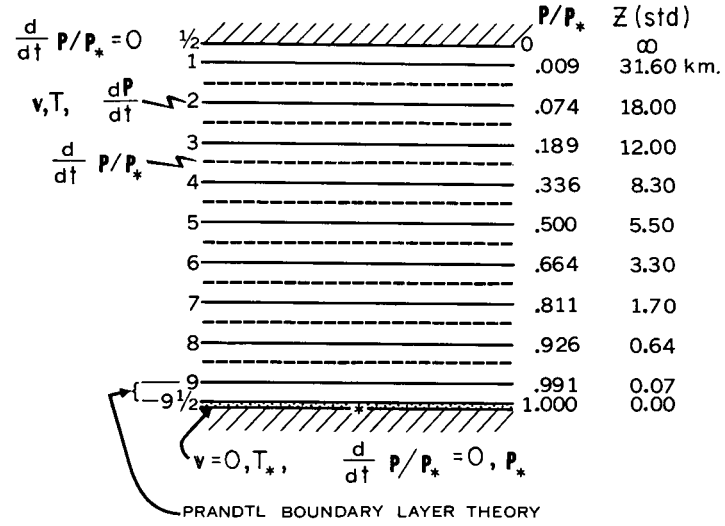

FIGURE 2F2.—Diagram of Q levels and their approximate heights. Notations are made as to where the model variables are predicted.

The absorptivities of gaseous absorbers under different pressures, and the reflectivities as well as absorptivities of high, middle, and low clouds adopted for this study are described in the paper by Manabe and Strickler [17]. Refer to the same paper for the climatological vertical distributions of water vapor, carbon dioxide, ozone, and clouds. All the above and the surface albedo are specified as a function of latitude only.

F. COMPUTATIONAL SPACE MESH

The hydrodynamical equations of the general circulation model are solved for a rectangular grid on a stereographic map projection of the Northern Hemisphere, tangent to the earth at the north pole. The positive X-axis of the Cartesian grid is directed along the Greenwich meridian. The number of points between the north pole and the equator, N, is all the additional information required to specify the grid uniquely. In the experiment reported on here we have taken $N=20$ which corresponds to an earth distance between grid points of about 320 km. at the equator, 540 km. at 45°, and 640 km. at the pole.

In order to restrict this study to the Northern Hemisphere an insulated, free-slip boundary is constructed just one-half-grid-point distance outside the envelope of the southernmost grid points in the hemisphere. An exception is made at the coordinate axes where the boundary is one-half grid point inside the hemisphere. This boundary never extends farther than 2° north at $N=20$. Refer to figure 2F1 for a diagram of one quadrant of the grid including this boundary.

The so-called "σ-system" of Phillips [28] is used for the vertical coordinate; that is, data levels are defined as being at specified fractions of the surface pressure P_* rather than at fixed pressures. Furthermore, contrary to normal procedure with this σ-system, the nine data levels used in this model are not evenly spaced with respect to pressure but are arranged so as to give maximum resolution in pressure at the extremes of the atmosphere, namely near the ground and in the stratosphere. The fractions used, denoted as Q values, are defined as

$$Q_k=\sigma_k^2(3-2\sigma_k) \tag{2F1}$$

where

$$\sigma_k=\frac{2k-1}{18},\ (k=1, 2, \cdots, 9) \tag{2F2}$$

The pressure at a given data level k is given by:

$$P_k=P_*\cdot Q_k \tag{2F3}$$

Values of Q_k and Δ_{Q_k} are listed in Table 2F. The Δ_{Q_k} values in this table are computed as the difference between Q values at half levels centered on full levels. The values of Q at half levels are computed from σ values

TABLE 2F.—*Q levels used in model*

Level	σ	Q	ΔQ
1	1/18	0.008916	0.034294
2	3/18	.074074	.091907
3	5/18	.188615	.133059
4	7/18	.336077	.157750
5	9/18	.500000	.165980
6	11/18	.663923	.157750
7	13/18	.811385	.133059
8	15/18	.925926	.091907
9	17/18	.991084	.034294

halfway between the σ values corresponding to full levels.

A diagram of these Q levels and their approximate heights is shown in figure 2F2. The horizontal component of the wind, temperature, and ω are predicted on full levels whereas $\dot{Q}$ is computed on half levels. Surface pressure and temperature are forecast on level 9½ where $Q=1.0$.

3. INITIAL CONDITIONS AND TIME INTEGRATION

The initial condition adopted for the time integration is a resting isothermal atmosphere at 289°K. In order to save computation time, the integration from 0 days to 78 days was performed by use of a coarse grid system ($N=10$); further integrations were then continued by use of the finer grid system ($N=20$). Refinement of the grid was performed by linearly interpolating wind velocity, temperature, and pressure. During the initial period of investigation, a Hadley regime emerges. A circumpolar westerly vortex develops in the upper part of the atmosphere and an easterly vortex appears near the earth's surface, while a single cell meridional circulation predominates. At 78 days of the $N=10$ calculation the meridional temperature gradient of 45°C. does not yield baroclinic instability because the horizontal resolution is inadequate. However, about eight days after the refinement to $N=20$ (a total lapse time of 86 days), waves start to develop in the surface pressure pattern, indicating the beginning of baroclinic instability. In the following two weeks, westerly waves are formed and the polar High penetrates into low latitudes of the subtropics at various longitudes and forms several subtropical Highs. Meanwhile, the westerly flow extends to the earth's surface in middle latitudes and the single Hadley cell evolves into a three-cell meridional circulation.

The evolution from an isothermal atmosphere into the stratosphere-troposphere system is very similar to the results of the time integration preformed by Manabe and Strickler [17] without the effect of large-scale motion. Refer to figure 1 of their paper for further details of this evolution. Usually, it takes 200 days before a state close to thermal equilibrium is reached. However, the cloud distribution of the model was changed at 176 days of our time integration in order to bring it to closer correspondence to the real atmosphere. It was therefore necessary to continue the computation to 300 days by which time statistical equilibrium was well established. Figure 3.1 shows the time series of the hemispheric mean temperature for the period from 175 to 300 days. The 70-day period of 231–300 days was adopted for our detailed analysis. Based upon the time series of temperature shown in figure 3.1, it may be concluded that we reached a state close enough to the state of thermal equilibrium before the beginning of this period.

In order to evaluate the degree of convergence toward the state of quasi-equilibrium, the hemispheric mass-weighted integrals of various quantities other than

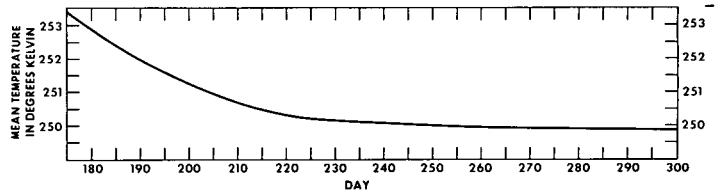

FIGURE 3.1.—Time variation of hemispheric mean temperature for the period of 175–300 days.

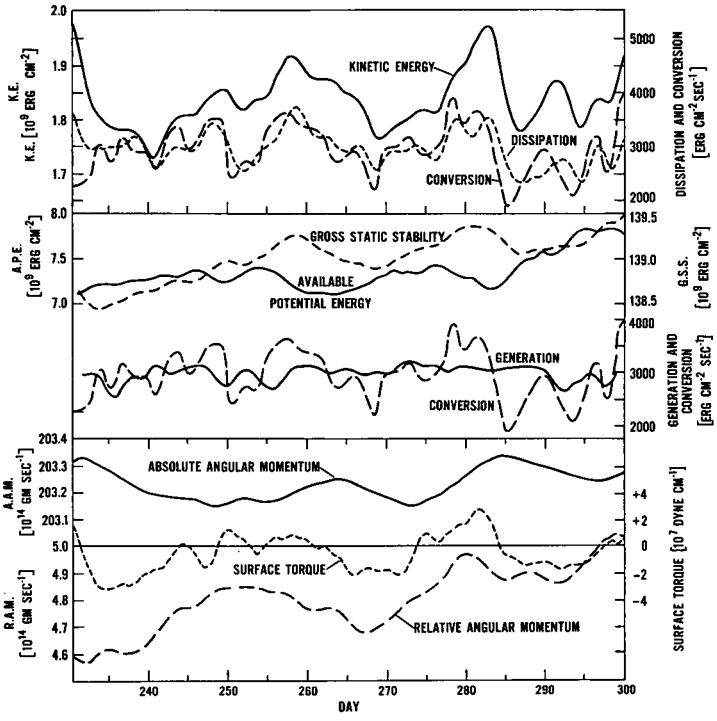

FIGURE 3.2.—In the upper part of the figure, the solid line shows the time variation of the hemispheric mean of kinetic energy for the period of 231–300 days, and the long-dashed and short-dashed lines show the time variation of the hemispheric mean of conversion and of dissipation, respectively. In the middle part of the figure, the time variation of total available potential energy and gross static stability are shown by solid and dashed lines respectively. The rate of generation (source) and conversion of available potential energy are also shown by solid and dashed lines respectively. In the lower part of the figure, the solid line and long-dashed line show the time series of the hemispheric mean of absolute angular momentum and of relative angular momentum for the period of 231-300 days, respectively. The short-dashed line shows the time variation of the hemispheric mean of surface torque.

temperature were also obtained for each time step in the integration. It turned out that these integrals are very useful as indicators of the consistency of the model. The upper part of figure 3.2 shows the time variation of kinetic energy, that of conversion from potential to kinetic energy, and that of dissipation of kinetic energy for the 70-day period chosen for our analysis. Since the magnitude of the conversion term varies violently with time in the model, the variation with period shorter than 1 day is removed by a running mean. Note the variation of kinetic energy is consistent with the difference

TABLE 3.1.—*Hemispheric budget of kinetic energy for 231–300-day period*

Mean conversion of potential energy	2901 erg cm.$^{-2}$ sec.$^{-1}$
Mean dissipation of kinetic energy	2939 erg cm.$^{-2}$ sec.$^{-1}$
Mean rate of change of kinetic energy	4 erg cm.$^{-2}$ sec.$^{-1}$

TABLE 3.2.—*Hemispheric budget of available potential energy for 231–300-day period*

Mean net generation of available potential energy	3003 erg cm.$^{-2}$ sec.$^{-1}$
Mean conversion of available potential energy	2901 erg cm.$^{-2}$ sec.$^{-1}$
Mean rate of change of available potential energy	114 erg cm.$^{-2}$ sec.$^{-1}$

TABLE 3.3.—*Hemispheric budget of absolute angular momentum for 231–300-day period*

Mean surface torque	0.057×10^{8} dyne/cm.
Mean change of absolute angular momentum	0.0056×10^{8} dyne/cm.

between the dissipation and conversion. Also, we computed the budget of kinetic energy for this 70-day period by performing the time integration of conversion and dissipation. Table 3.1 shows the result. These results suggest that the hemispherical integral of the contribution of the inertial terms almost vanishes as it should despite the truncation error of our time integration.

In the middle part of figure 3.2, the time variation of available potential energy as defined by equation (AII8), of the net generation and of conversion as defined by equations (AII11) and (AII10) are shown. According to this figure, the rate of net generation of available potential energy varies little with time partly because cloudiness is independent of time in the present model. Again, the difference between conversion and net generation approximately corresponds to the variation of available potential energy which is out of phase with that of kinetic energy (and gross static stability). Table 3.2 shows the budget of available potential energy during the 70-day period. These results suggest that, in our finite-difference system, the budget of available potential energy is consistently maintained.

In the lower part of figure 3.2 the time variation of the hemispheric integral of absolute angular momentum and that of surface torque are shown. Again, we notice that there is a rather good correspondence between the change of absolute angular momentum and surface torque, though the correspondence is not as good as in the case of the budget of kinetic energy. The budget of absolute angular momentum for this 70-day period is tabulated in table 3.3.

This result suggests that there is a fictitious source of angular momentum in our model. If one compares its magnitude with the latitudinal distribution of surface torque shown in figure 6A2, one finds that the relative magnitude of this fictitious source is practically negligible. The mean value for the area of negative torque is about 3.5×10^{8} dyne/cm., whereas the magnitude of fictitious torque is 5×10^{6} dyne/cm. Therefore, we shall disregard this discrepancy in further discussions.

4. STATE OF QUASI-EQUILIBRIUM

In this section, detailed descriptions of the state of quasi-equilibrium obtained from the time integration are made. As we mentioned in the previous section, the 70-day period of 231–300 days was chosen for this analysis. Figures and numerical results which are discussed in this and following sections were obtained for this period except for the case specified otherwise. Data were stored once a day and averaged.

Since on the stereographic projection adopted for our time integration few grid points lie on common latitude circles, it was necessary to perform a linear interpolation to obtain the zonal mean of any quantity at a given latitude. In order to avoid the error produced by interpolation, the zonal mean of product terms such as the transport of angular momentum, heat, and kinetic energy, which are discussed in the following sections, were computed by the processes described below.

(1) Compute the product terms using the same finite-difference method as was adopted for the time integration of the model.

(2) Obtain the average value of the products thus computed for each of a number of narrow latitude belts.

A. ZONAL MEAN TEMPERATURE

In figure 4A1, zonal mean temperatures obtained at three latitudes from the numerical integration of our model are shown on an adiabatic diagram together with the observed annual mean temperatures. According to this comparison, the general features of the stratosphere-troposphere system are simulated very well by our general circulation model. The pole-to-equatorial difference of the height of the tropopause in the model is about 7 km. which is somewhat smaller than, but not far from, the observed difference of about 10 km. In the numerical integration, a stable layer appears at high latitudes because of the stabilizing effect of baroclinic waves, northward advection of heat by the large-scale eddies, and the large albedo of the polar cap. Recently, Manabe and Strickler [17] computed the vertical distribution of the temperature of the atmosphere in thermal equilibrium for various albedos of the earth's surface. (Refer to fig. 11 of that paper.) Although they performed the computation for the case of large albedo, the temperature inversion on the earth's surface did not appear. These results suggest that not only the large surface albedo but also the effect of large-scale motion, particularly that of the horizontal advection of heat by the large-scale eddies, is indispensable for the maintenance of the polar inversion. Though the stable layer of the polar region, which is obtained in the present computation, is in qualitative agreement with the observed features, its static stability is less than that of

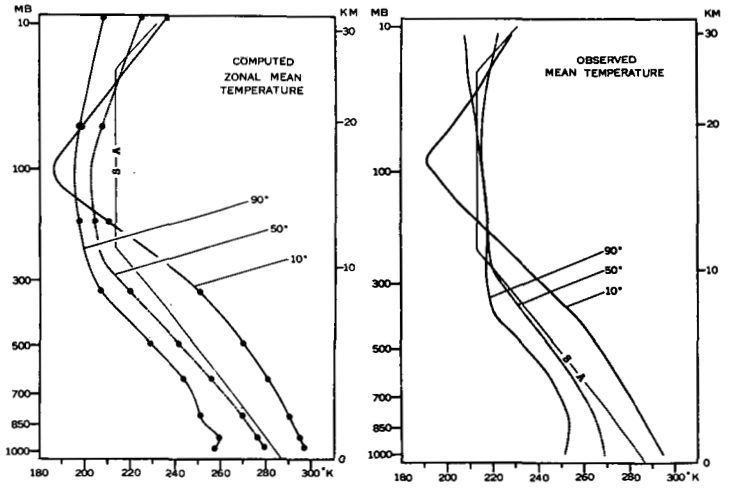

FIGURE 4A1.—The vertical distributions of zonal mean temperature obtained from our computation for various latitudes and that of the actual atmosphere are shown on the left- and right-hand sides of the figure, respectively. Light solid line marked S-A indicates the ICAO standard atmosphere.

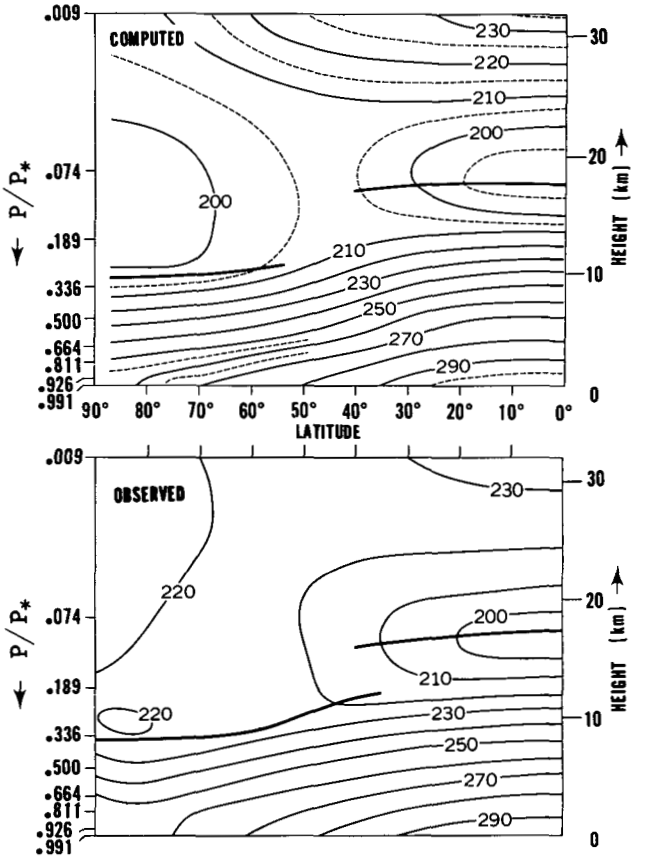

FIGURE 4A2.—The latitude-height distribution of the zonal mean temperature obtained from our computation and that of the actual atmosphere are shown in the upper and lower parts of the figure, respectively. The observed distribution is based on the results obtained by Peixoto [26] for the troposphere and by Oort [24] and Kochanski [10] for the stratosphere. The tropopause is indicated by a heavy line broken in middle latitudes.

the actual atmosphere. Further study is desirable before we can decide on the exact cause of this discrepancy.

Figure 4A2 shows the latitude-height distribution of zonal mean temperature obtained from our model compared with that of the actual atmosphere. In general, the similarity between the two distributions is remarkable, particularly near the earth's surface and in the upper stratosphere. In our model, the pole-to-equatorial temperature difference is about 42° C. at the earth's surface and coincides well with the observed difference. However, in the upper troposphere of middle latitudes, the latitudinal gradient of the temperature of our model is much larger than observed, and this is one of the major discrepancies between our model and the actual atmosphere. In the lower stratosphere of the model, the temperature increases by about 14° C. from the equator to middle latitudes, but decreases again with a further increase of latitude with the result that the net increase of temperature from equator to pole is only 5° C. It is encouraging, however, that we get significant latitudinal increase of temperature in the lower latitudes. At the top model level in the upper stratosphere ($P/P_*=0.009$), the decrease of temperature from equator to pole is about 28° C. which is close to the observed decrease of annual mean temperature (24° C.). In general, the thermal structure of our model atmosphere looks very similar to that of the observed winter atmosphere in spite of the fact that the annual mean solar insolation was given.

In their study of thermal equilibrium, Manabe and Strickler [17] obtained the state of the radiative equilibrium of the stratosphere overlying the troposphere with a realistic distribution of temperature. (Refer to fig. 13 of their paper.) According to this figure, the equilibrium temperature of the stratosphere increases slightly with increasing latitude for a July case, but the equilibrium temperature obtained for January decreases monotonically with increasing latitude. Therefore, the decrease of tropopause height with increasing latitude is significantly less than that obtained from the present study. The improvement accomplished by the present study is due to the incorporation of the effect of large-scale motion. Refer to section 5 (Heat Balance) for the discussion of this effect.

B. MEAN FLOW FIELD

In figure 4B1, the zonal mean of zonal current obtained from the present computation is compared with that of the actual atmosphere. The data obtained by Buch [4], and Oort [24] are used for determining the observed annual mean. The distributions for January and July are taken from the results obtained by Kochanski [10] for 80° W. longitude. According to this comparison, the latitude of maximum west wind in the upper troposphere of the model coincides well with the observation. The intensity of the jet, however, is much stronger than the observed annual mean. By the thermal wind relationship, this result is consistent with the excessive latitudinal

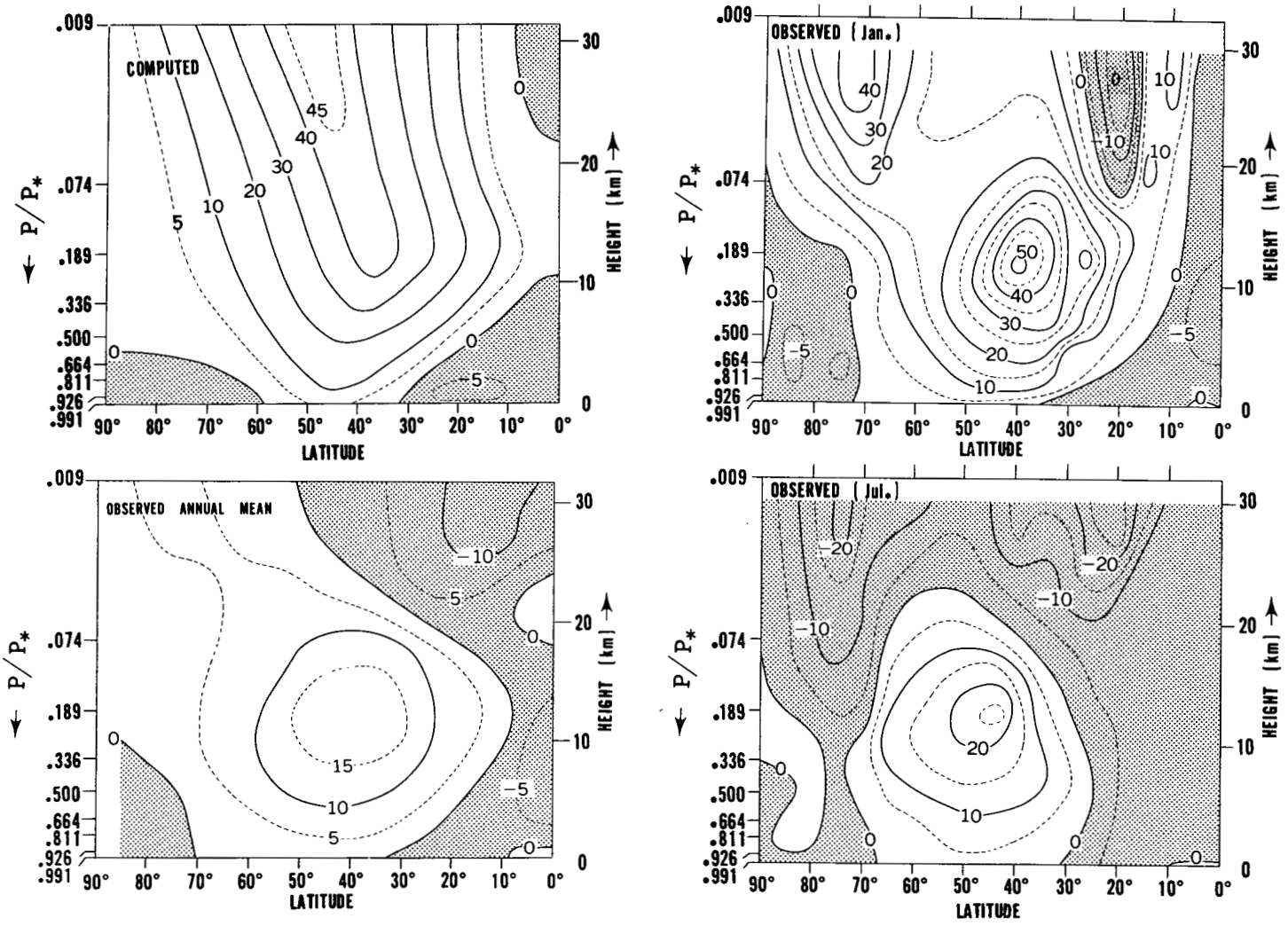

FIGURE 4B1.—In the upper left, the zonal mean of the zonal current of the model atmosphere obtained from our computation is shown In the lower left, the annual mean of the observed wind obtained by Buch [4] and Oort [24] is shown. The intensity of the zonal current at 80° W. obtained by Kochanski [10] for both January and July is shown in the upper right and lower right, respectively. (Units: m./sec.)

gradient of temperature in the upper troposphere of the model atmosphere which was pointed out in the previous section. A similar tendency appears in the results obtained by Smagorinsky [37] and Phillips [27]. One of the reasons may be the absence of a hydrologic cycle in the model. We shall discuss this possibility in a companion paper [18].

Another possibility is that the observed annual mean is derived from an atmosphere subjected to the annual variation of solar radiation including a polar night. On the other hand, our calculations represent the response to the annual mean solar radiation. There may be a fundamental fallacy in comparing these two. It is noteworthy that the maximum intensity of the annual mean zonal current is much less than the average of the maximum intensity at 80° W. in July and in January. In general, the computed distribution is close to the observed distribution in January though the tilt of the axis of the maximum westerlies in the stratosphere is much less than observed. In the tropical upper stratosphere of the model atmosphere, a weak easterly current appears. Its intensity, however, is much weaker than the observed intensity which prevails in tropical latitudes. Refer to figure 4C2 for the longitudinal distribution of these easterlies.

Next, we shall examine the structure of the mean meridional circulation, since it plays a major role in the general circulation of the atmosphere. In figure 4B2, are shown the zonal mean of the meridonal wind component and that of the vertical wind component obtained from our model. According to this figure, a three-cell circulation appears in the troposphere. In the stratosphere, the circulation tends toward two cells with increasing altitude; that is, the direct polar cell is squeezed out by a poleward expansion of the equatorial Hadley cell. Accordingly, the axis of maximum meridional velocity tilts northward in the stratosphere. Mintz and Lang [19] computed the distribution of the meridional component of the wind for the troposphere based upon an angular momentum balance

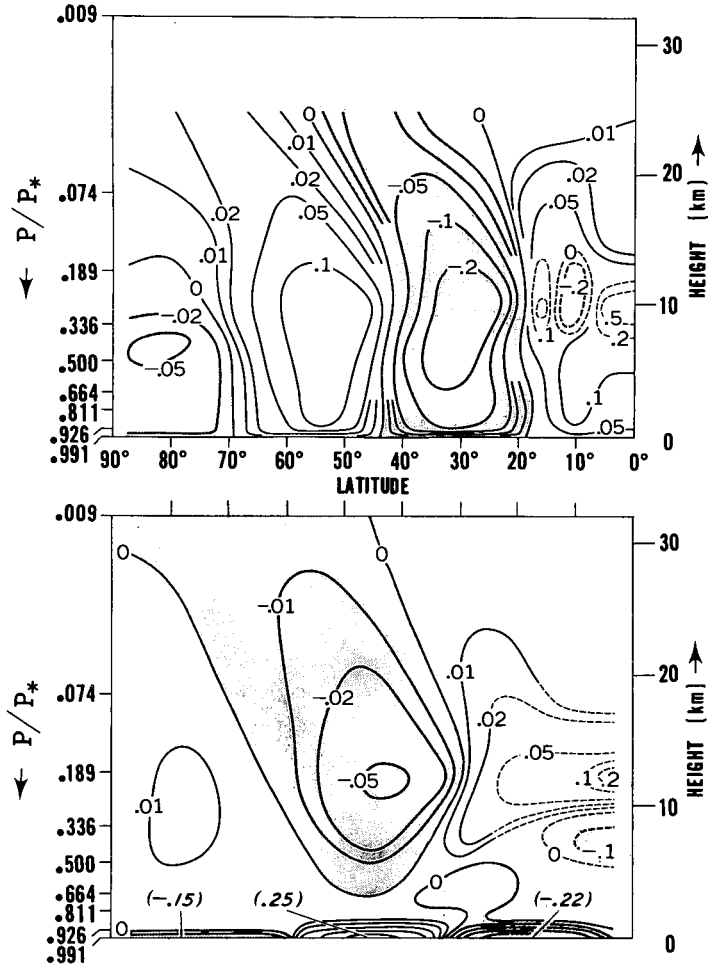

FIGURE 4B2.—The zonal mean of the vertical component of the wind (cm./sec.) and of the meridional component of the wind (m./sec.) of the model atmosphere are shown in the upper and lower parts of the figure, respectively. Positive values are upward and northward.

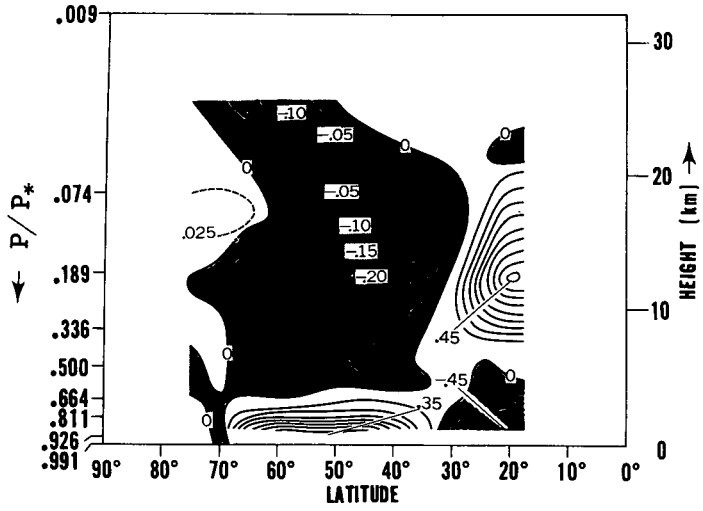

FIGURE 4B3.—The meridional component of the wind (m./sec.) obtained from the requirement of momentum balance of the actual atmosphere. The distribution in the stratosphere (30-mb., 50-mb., and 100-mb. level) was obtained by Teweles [41] and that in the troposphere was obtained by Mintz and Lang [19].

requirement. More recently, Teweles [41] applied a very similar technique to the stratosphere. Figure 4B3 shows the combined results. The axis of the maximum meridional component of the wind also tilts northward in the stratosphere, however the degree of tilt is somewhat larger in the actual atmosphere than computed in our model. (Refer also to the distribution of vertical motion obtained by Miyakoda [21] for winter.)

Another characteristic feature of our results is the narrow belt of strong meridional wind component near the earth's surface. A somewhat similar belt is noticeable in the results of Mintz and Lang [19]. As the result of this phenomenon, the meridional circulation cell obtained by the model is highly eccentric. It is clear from our study of the momentum balance in section 6, that the eccentricity of the meridional circulation depends upon the assumed distribution of the vertical mixing coefficient. This is because the change in angular momentum in the Ekman boundary layer resulting from the surface torque must mainly be compensated by the change of relative angular momentum due to the meridional circulation. Further study of observational data is necessary for a more definitive evaluation of the simulated meridional circulation.

C. SYNOPTIC MANIFESTATIONS

Figure 4C1 displays an example of the synoptic distribution of temperature, pressure, and wind in our model atmosphere. In this figure the synoptic distributions of the geopotential lines and isotherms are shown by solid and dashed lines respectively, and the areas of southerly flow are shaded. These shaded areas or the geopotential gradient at these levels remind us of the actual situation which prevails during the winter. According to figure 4C2, which shows one example of the calculated synoptic distribution of the zonal wind component at $P/P_*=0.009$, a very strong zonal wind develops in middle latitudes. On the other hand, patches of easterly wind appear at low latitudes. According to figure 4B1, the calculated zonal mean easterly wind is much weaker than observed. It is encouraging, however, that some easterly wind even appears in the simulated tropical stratosphere.

In figure 4C1, the maps of the tropospheric levels show the same features as those observed in the actual atmosphere: for example, the tilt of the troughs with respect to the meridians and the lag of the thermal trough behind the trough of geopotential height. This is obviously necessary for a correct transfer of angular momentum and heat. According to figure 4C3, the occlusion of isotherms into low centers develops at various places. Also at a low level a high pressure belt develops in the subtropics as is found in the actual atmosphere. Figure 4C4 shows the zonal mean of surface pressure in our

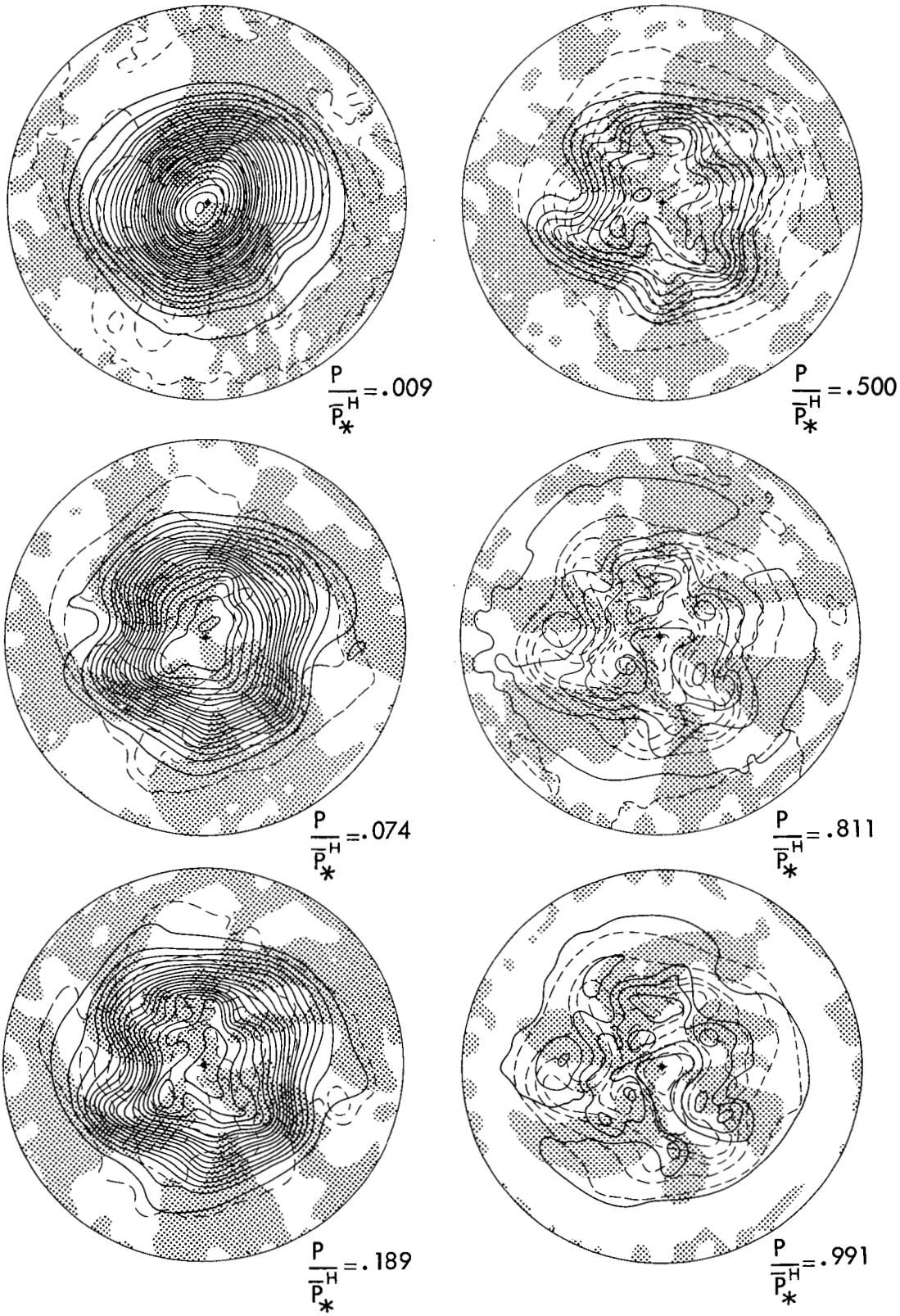

FIGURE 4C1.—In each map, the solid and dashed lines show the contour heights of isobaric surfaces (every 100 m.) and isotherms (every 5° C.) on the 259th day, respectively. The areas of southerly flow are shaded.

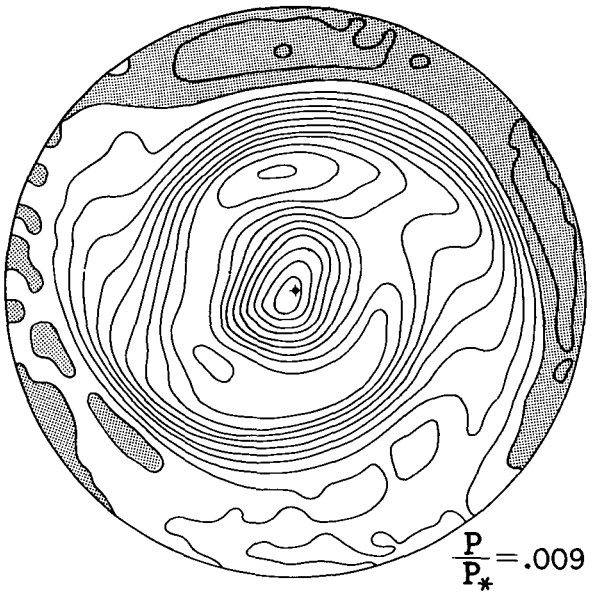

FIGURE 4C2.—Distribution of the intensity of zonal wind at the first model level ($P/P_*=0.009$) on the 259th day. The contour interval is 5 m./sec. The areas of easterlies are shaded.

FIGURE 4C3.—Surface isobars (every 5 mb.) and surface isotherms (every 5° K.) on the 259th day are shown by solid and dashed lines, respectively.

model.[2] The latitude of the subtropical High and that of the lowest zonal mean pressure coincide well with observation. The magnitude of latitudinal variation of pressure turned out to be somewhere between the observed value of the Northern Hemisphere and that of the

[2] The mean surface pressure of the model atmosphere is about 28 mb. lower than observed because the model has the same mass of air as the actual atmosphere but it has no mountains.

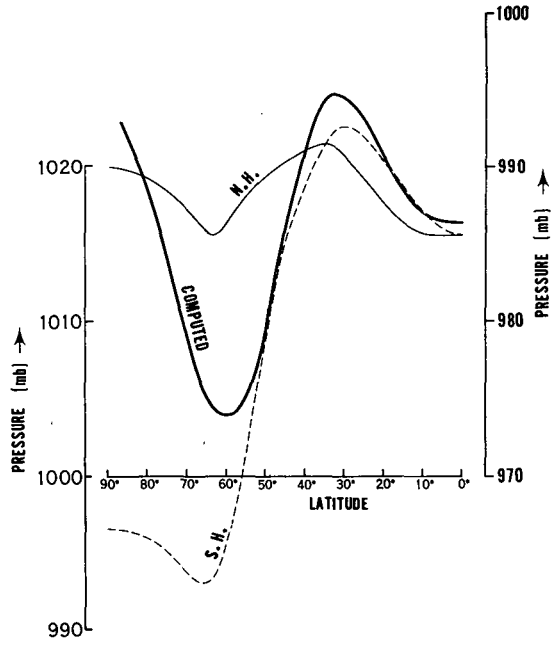

FIGURE 4C4.—The latitudinal distribution of the zonal mean of surface pressure. Computed distribution is shown by a thick solid line (scale on right), and observed distributions for the Northern and Southern Hemispheres are shown by thin solid and thin dashed lines, respectively (scale on the left).

Southern Hemisphere. Further improvement in the similitude of the surface pressure field may be accomplished by considering global motions and admitting land-sea contrast. Recently, Mintz [20] successfully simulated the distribution of the zonal mean of surface pressure in both hemispheres by taking into consideration the effect of the land-sea distribution.

The synoptic distributions of vertical motion are shown in figure 4C5. Above the level of the tropopause, the intensity of the vertical motion decreases sharply with increasing height. (Note that the contour intervals are not the same for all maps.) Some features of the large-scale vertical motion in the troposphere, however, are identifiable in the stratosphere despite the strong damping.

D. HARMONIC ANALYSIS

In figure 4D1 the energy spectra of the calculated and observed meridional and zonal components are shown. As indicated by the synoptic charts, the meridional component of the wind in our model atmosphere has a maximum energy at wave number 6 in the troposphere, and this wave number of maximum energy decreases with increasing altitude in the stratosphere. As the right-hand side of the figure indicates, the same wave numbers prevail in the actual troposphere. In the troposphere the energy spectrum of the zonal component of the wind of our model atmosphere has relatively large values at wave numbers from 1 to 4, whereas a sharp maximum exists at wave number 1 in the actual atmosphere. This discrepancy is partly a result of ignoring

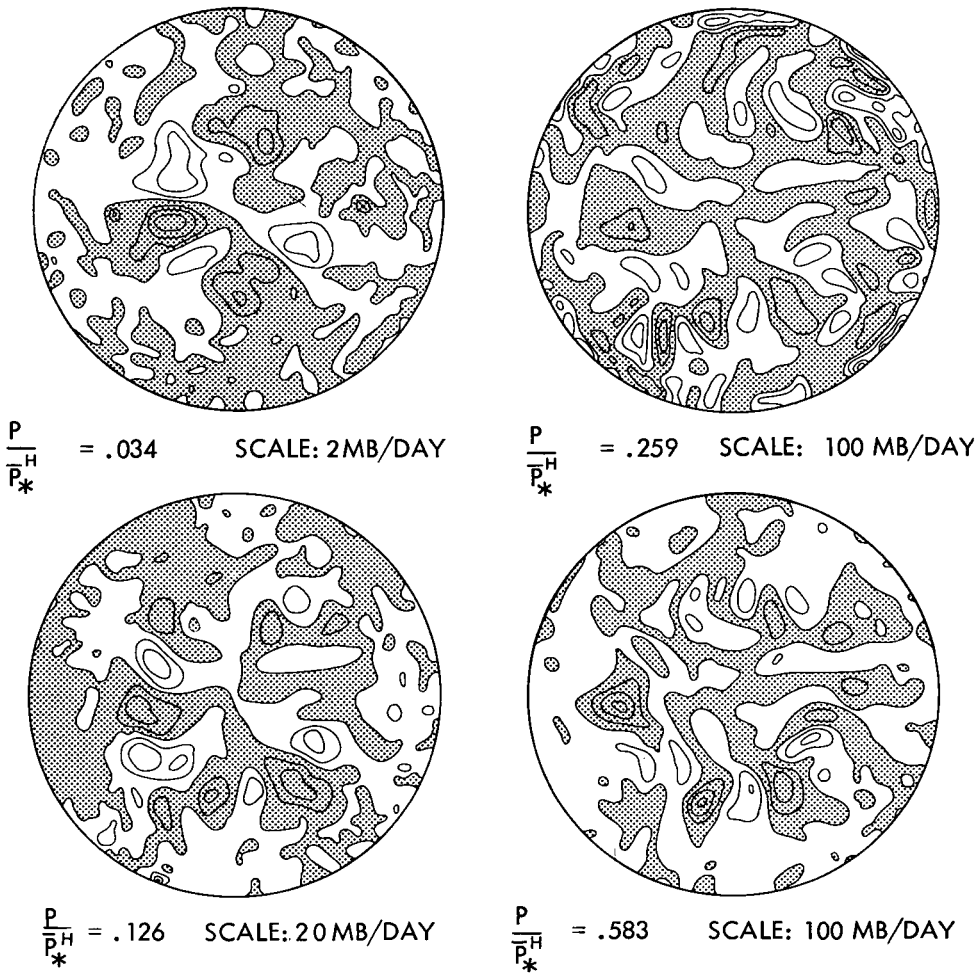

FIGURE 4C5.—The distribution of $\dot{Q}$ on the 259th day. The areas of positive $\dot{Q}$ (downward motion) are shaded. Note that the scale (contour interval) is different for different levels.

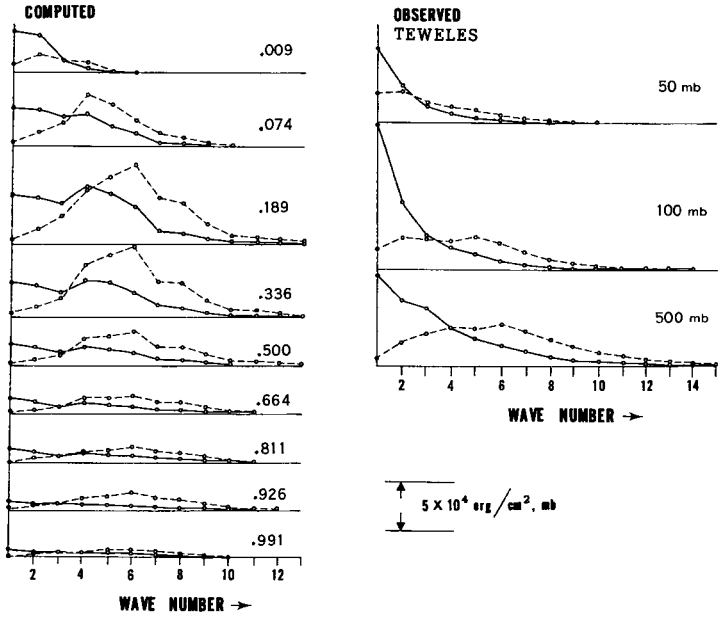

FIGURE 4D1.—The vertical distribution of the energy spectra of the zonal and meridional wind components are shown by solid and dashed lines, respectively. The computed values are hemispheric means and the observed data are the average between 15° N. and 80° N. The numbers beside the computed distributions are $P/P*$ ratios.

the effects of the land-sea distribution and the effects of mountains. If the flow circling around the pole has some eccentricity due to the lack of uniformity of the earth's surface, the eccentricity of the zonal current is regarded as an eddy of wave number 1. It is interesting, however, that the energy spectrum of the meridional component of wind is quite different from that of the zonal components of wind for both the actual atmosphere and the model. In the model, the energy in low wave numbers is probably transferred from that in higher wave numbers by the non-linear interaction between waves.

In order to examine the vertical variation of wave numbers further, the hemispheric mean effective wave number $\bar{n}$ at various altitudes is computed for the model and for the actual atmosphere. $\bar{n}$ is defined as follows:

$$\bar{n}=\left(\int n dE(n)\right)\Big/\left(\int dE(n)\right) \qquad (4D)$$

where $E(n)$ is the energy spectrum. The spectra obtained by Teweles [41] for the period from July 1957 to June 1958 are used for obtaining $\bar{n}$ for the actual atmosphere. Figure 4D2 shows the results. The $\bar{n}$ of the meridional wind component of the model is close to observation, the

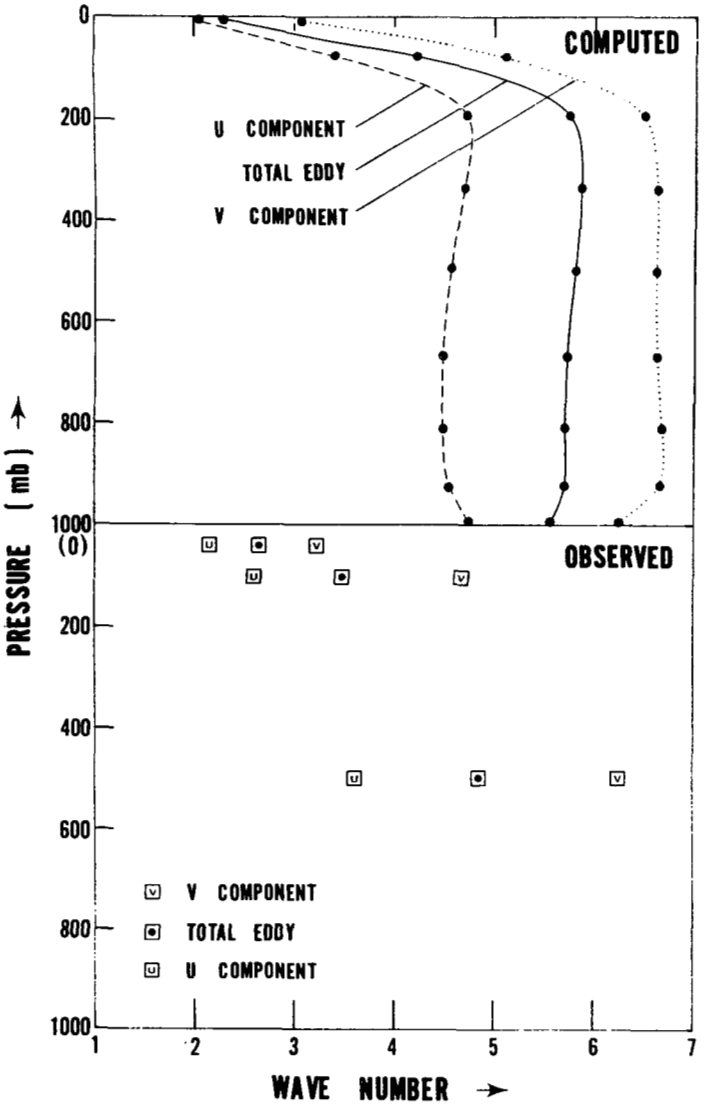

FIGURE 4D2.—The vertical variation of energy-weighted wave number $\bar{n}$. Dotted, dashed, and solid lines show the vertical distributions of the effective wave number $\bar{n}$ of the meridional wind component (hemispheric mean), of the zonal wind component, and of the total wind component, respectively. In the lower part of the figure is shown the vertical variation of $\bar{n}$ computed from the results of the harmonic analysis of the observed wind field, which was performed by Teweles [41] for the period July 1957 to June 1958. The domain of averaging ranges from 15° N. to 80° N.

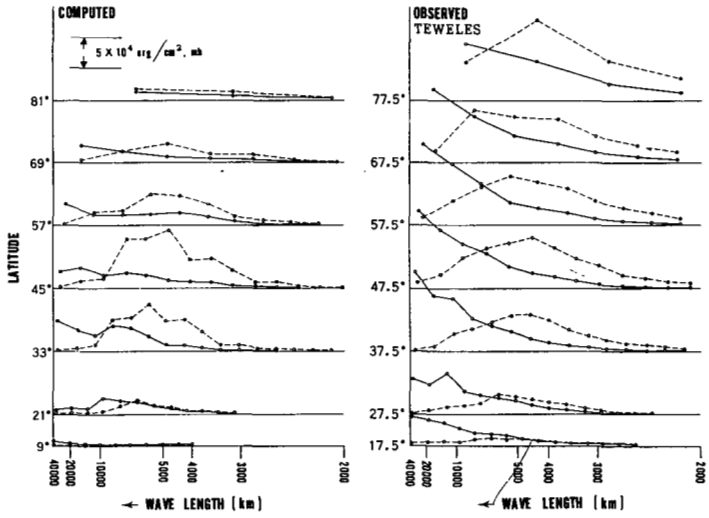

FIGURE 4D3.—The latitudinal variation of the effective mean wavelengths of the zonal wind component and of the meridional wind component are shown by solid and dashed lines, respectively.

difference being only ⅓ of a wave number. On the other hand the $\bar{n}$ of the zonal wind component of the model is larger than that of the actual atmosphere by about one wave number. The general height dependence of $\bar{n}$, however, is simulated very well. As we shall show later, the kinetic energy of the stratosphere is maintained by energy from the troposphere supplied mainly by the pressure interaction term. According to Charney and Pedlosky [5], the damping of the pressure interaction term with altitude is proportional to the stability of the layer, to wave number, and to the degree of baroclinic instability. Thus the theory is consistent with the fact that long waves predominate in the stratosphere. This subject will be discussed further in the section on the balance of kinetic energy.

For reference, the latitudinal variation of the energy spectra is shown in figure 4D3. For convenience in comparison, the spectrum is plotted versus wavelength instead of wave number. In high latitudes the eddy kinetic energy of the actual atmosphere is much larger than that of our model atmosphere. Again, this discrepancy may partly be due to the eccentricity of the circumpolar vortex in the observed atmosphere. It is noteworthy that the characteristic wavelength increases slightly with decreasing latitude for both the actual atmosphere and our model.

E. DISTRIBUTION OF KINETIC ENERGY

In this section we shall examine the latitude-height distribution of eddy kinetic energy. Figure 4E1 shows the vertical distribution of the hemispheric mean eddy kinetic energy of our model atmosphere. In the same figure we also show values of the hemispheric mean eddy kinetic energy for the actual atmosphere obtained by various authors. According to this comparison, the observed values are much larger than the calculated ones. Although they may be somewhat overestimated because of the geostrophic assumption, there must be other reasons for this discrepancy. The level of the maximum eddy kinetic energy lies at approximately 200 mb. in the model atmosphere and coincides with that in the actual atmosphere.

The latitude-height distribution of eddy kinetic energy is shown in figure 4E2. The latitude of the maximum of eddy kinetic energy falls approximately at 40° N. and coincides with that of the maximum zonal velocity. In figure 4E3 the latitudinal distribution of eddy kinetic energy at the 500-mb. level obtained by Saltzman [35], is compared with our results. In high latitudes the eddy kinetic energy of the actual atmosphere is much larger

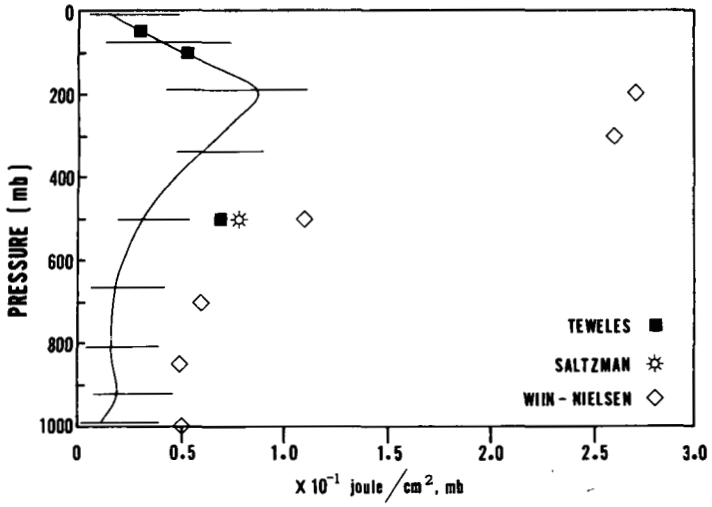

FIGURE 4E1.—The vertical distribution of the hemispheric mean of eddy kinetic energy is shown as a function of altitude. The area mean of eddy kinetic energy obtained by Wiin-Nielsen [43], Teweles [41], and Saltzman [35] for the actual atmosphere are also plotted for the sake of comparison. The latitudinal ranges of the area means for these studies [43, 41, and 35] are 16.75°–88.75° N., 15°–80° N., and 15°–80° N., respectively.

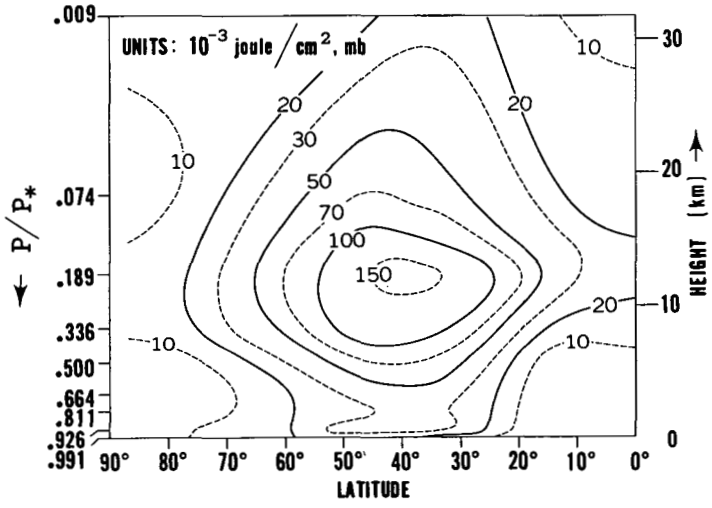

FIGURE 4E2.—Latitude-height distribution of eddy kinetic energy obtained by the model.

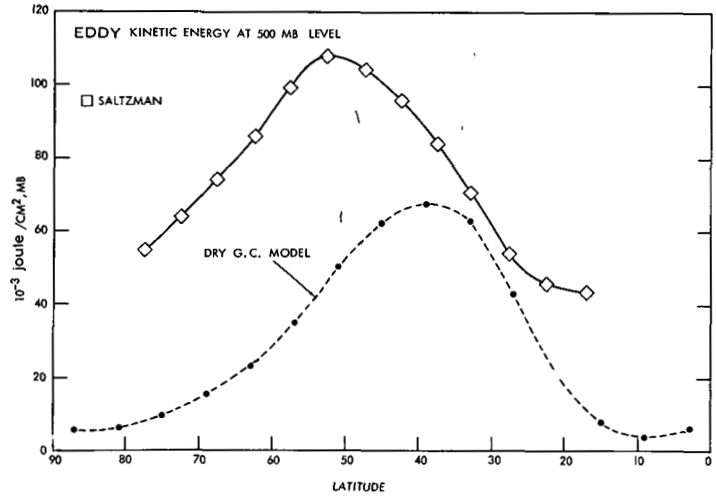

FIGURE 4E3.—The latitudinal distribution of eddy kinetic energy at the 500-mb. level. The annual mean value obtained by Saltzman [35] for 1951 is also plotted for comparison.

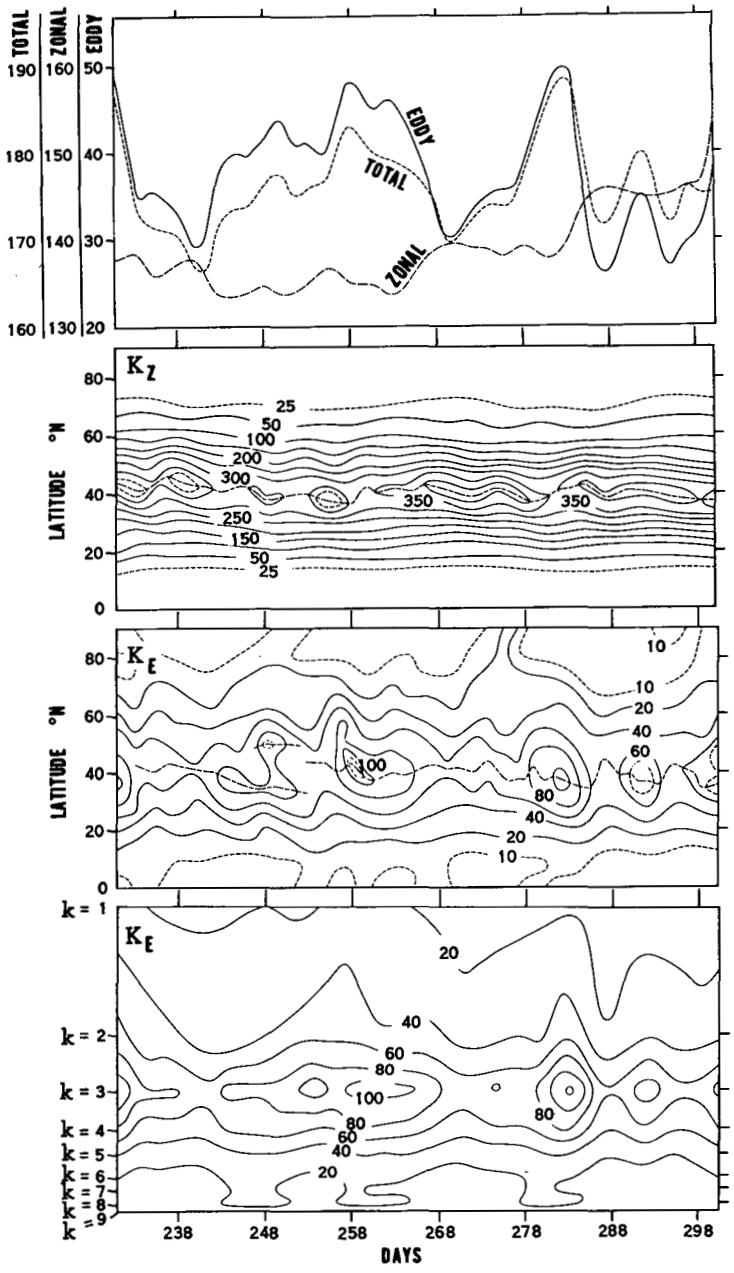

FIGURE 4E4.—In the top of the figure the time variations of total kinetic energy, of zonal kinetic energy, and of eddy kinetic energy for the period of 231–300 days are shown by short dashed, dashed, and solid lines, respectively. (Units: joule/cm.²) In the center, the time variation of latitudinal distributions of both zonal and eddy kinetic energy are shown (units: joule/cm.²). At the bottom, the time variation of the vertical distribution of eddy kinetic energy is shown. The units are 10^{-3} joule cm.$^{-2}$ mb.$^{-1}$ (Hemispheric mean).

than that of our model probably because of the irregularity and the eccentricity of the circumpolar vortex caused by the kinematic and thermal asymmetries of the lower boundary, i.e., land and sea.

The upper part of figure 4E4 shows the time variation of the total kinetic energy, the zonal kinetic energy, and the eddy kinetic energy. As expected, during the 70-day period chosen for our extensive analysis, the variation of zonal kinetic energy is mainly out of phase with that of

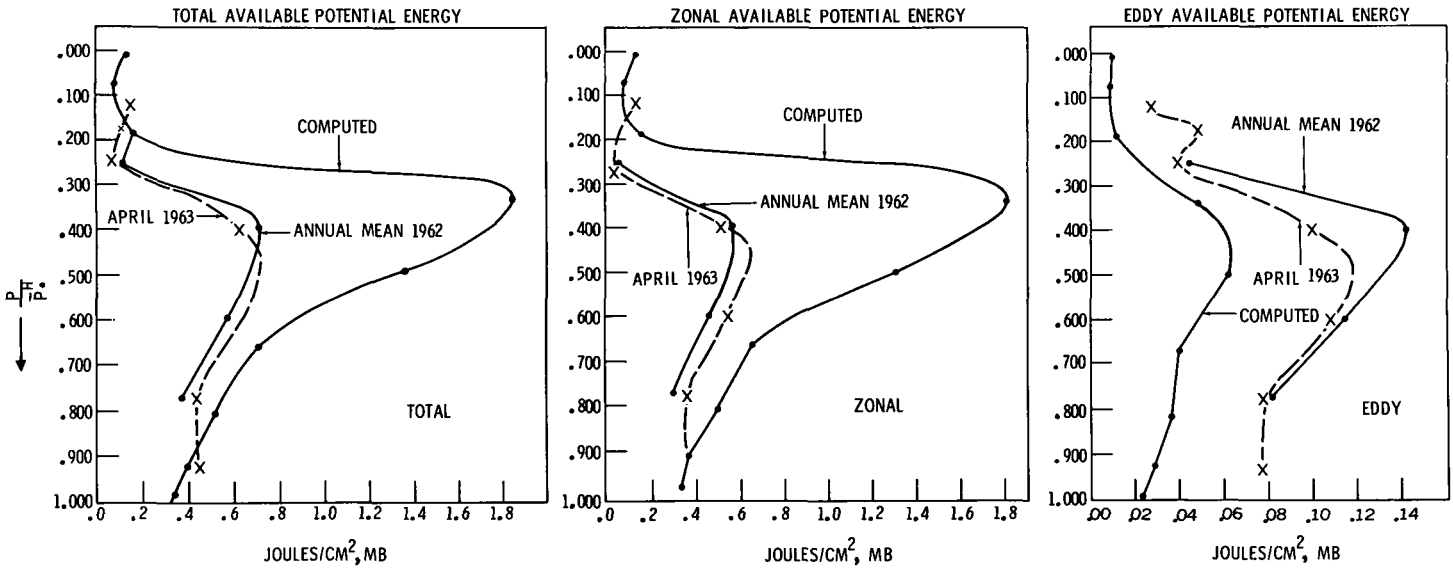

FIGURE 4F1.—The vertical distribution of total, zonal, and eddy available potential energy are shown in the left, center, and right side of this figure, respectively. The corresponding distributions obtained by Wiin-Nielsen [43] for April 1963 and the whole year of 1962 are also shown.

eddy kinetic energy. Since the variation of eddy kinetic energy is much larger than that of the zonal kinetic energy, the time variation of the eddy kinetic energy and that of the total kinetic energy are very similar. Although the magnitude of the kinetic energy varies with a period of approximately two weeks as Smagorinsky [37] pointed out in his earlier work, it is not possible to find a distinct period. In the center of the figure, the time variation of the latitudinal distribution of zonal and eddy kinetic energy are shown. The latitude of maximum energy changes with time. The range of fluctuation, which is several degrees of latitude, is somewhat smaller than the range observed in the actual atmosphere.

In the lower part of this figure, the time variation of the vertical distribution of eddy kinetic energy is shown. This result shows that the level of maximum eddy kinetic energy hardly changes with time during this portion of the numerical simulation.

F. DISTRIBUTION OF AVAILABLE POTENTIAL ENERGY

According to Lorenz [15], simplified versions of the total, the zonal, and the eddy available potential energy may be defined as the mass integral of A_T, A_Z, and A_E defined as follows:

$$A_T=\tfrac{1}{2}\gamma[T'']^2 \tag{4F1}$$

$$A_Z=\tfrac{1}{2}\gamma[(\overline{T}^{\lambda})'']^2 \tag{4F2}$$

$$A_E=A_T-A_Z \tag{4F3}$$

where $(\ )''$ denotes the deviation of the temperature on an isobaric surface from its hemispherical mean, and

$$\gamma=-\frac{R}{\dfrac{\partial\overline{\theta}^{H}}{\partial P}}\frac{1}{P}\left(\frac{P_{00}}{P}\right)^{\kappa}=-\frac{R}{P\left(\dfrac{\partial\overline{T}^{H}}{\partial P}-\kappa\dfrac{\overline{T}^{H}}{P}\right)} \tag{4F4}$$

where θ is the potential temperature of the air and P_{00} denotes the base pressure, 1000 mb., and $\overline{(\ )}^{H}$ and $\overline{(\ )}^{\lambda}$ denote the hemispheric mean and zonal mean respectively.

In figure 4F1, the vertical distributions of total, zonal, and eddy available potential energy obtained from our computation are shown together with those computed from actual data by Wiin-Nielsen [43]. In general, the zonal available potential energy obtained from our model is much larger than that of the actual atmosphere (annual mean value). This large available potential energy is consistent with the very large latitudinal temperature gradient of the upper troposphere which appeared in our calculation (see section 4A). On the other hand, the eddy available potential energy of our model atmosphere is significantly smaller than that of the actual atmosphere (annual mean value). This discrepancy may result partly from the lack of mountains and of land and sea contrast. In other words, the asymmetries of the lower boundary create the eccentricity in the latitudinal gradient of temperature and alter the partitioning of the available potential energy in favor of the eddy potential energy. Furthermore, the magnitude of the energy components is sensitive to the horizontal resolution of the model and the magnitude of the subgrid-scale mixing coefficient. One must also expect that the eddy amplitudes will depend on whether or not heat may be transferred in latent as well as sensible form.

The level of maximum zonal available potential energy lies at about the 350-mb. level, which is somewhat higher than in the real atmosphere (400 mb.). Again, this is

consistent with the model error in the latitudinal temperature gradient. The maximum eddy available potential energy lies at approximately 400 mb., which is reasonably close to the pressure of the observed maximum.

5. HEAT BALANCE

The study of heat balance of the atmosphere has been performed by many authors (e.g. Houghton [7], London [14], Ohring [23], Manabe and Möller [16], and Davis [6]). In this section, detailed investigation of the heat balance of the model atmosphere is made and compared with that of the actual atmosphere. Based upon this comparison, the causes of the coincidences or discrepancies of the various features of the thermal structure of the model atmosphere with the observed features are discussed.

A. HEMISPHERIC MEAN OF HEAT BALANCE COMPONENTS

The hemispheric means of various heat balance components at the top and bottom of the model atmosphere are compared in table 5A with those obtained by London [14] for the actual atmosphere. The coincidence between them is encouraging and is the natural consequence of the successful simulation of the temperature field as a whole. Note that all the net radiation received by the earth's surface is transferred to the atmosphere in the form of sensible heat because of the lack of evaporation.

TABLE 5A.—*Hemispheric mean of heat balance components (units are ly./min.)*

		Model atmosphere	Actual atmosphere
Top of the atmosphere	Net solar radiation	−0.329	−0.324
	Net long-wave radiation	.329	.324
Earth's surface	Net solar radiation	−.232	−.237
	Net long-wave radiation	.081	.090
	Turbulent energy flux	.154	.147

B. LATITUDINAL DISTRIBUTION OF HEAT BALANCE COMPONENTS

The latitudinal distribution of net upward radiative fluxes at the top of the atmosphere and those of net upward radiative fluxes and turbulent energy fluxes at the earth's surface are shown in figure 5B1. For the sake of comparison, the corresponding quantities obtained by London [14] for the actual atmosphere are plotted in the same figure. The general agreement between the net fluxes of our model and those of the actual atmosphere is very good. In figure 5B2, the northward flux of energy expected from the radiative imbalance of the earth-atmosphere system is shown together with the northward fluxes obtained by Houghton [7] and London. According to this figure, the total northward transport of energy of our model turned out to be somewhat smaller than the annual mean flux obtained by either Houghton [7] or London [14] mainly because of the slight difference in the latitudinal gradient of net outgoing radiation. As we described in section 4A,

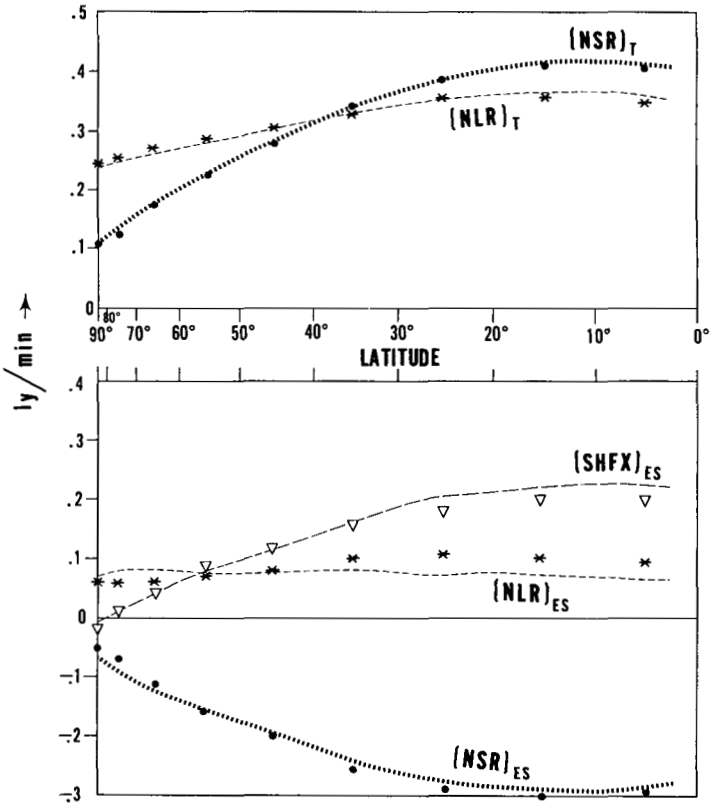

FIGURE 5B1.—The upper half of the figure shows curves of the latitudinal distribution of net upward long-wave radiation $(NLR)_T$ and that of net downward solar radiation $(NSR)_T$ at the top of the atmosphere. The lower half of the figure shows the latitudinal distribution of the net upward long-wave radiation $(NLR)_{ES}$, of net upward solar radiation $(NSR)_{ES}$, and of the upward turbulent flow of heat $(SHFX)_{ES}$ at the earth's surface. The corresponding quantities obtained by London [14] are plotted in the same figure as stars, dots, and triangles for comparison.

the latitudinal gradient of temperature obtained from our model is significantly larger than the annual mean gradient of the actual atmosphere and this is responsible for the present discrepancy.

In the lower part of figure 5B2, the northward eddy flux of heat obtained from our model is shown together with those obtained by Starr and White [39] for the annual mean and Peixoto [26] for winter. According to this comparison, the computed eddy flux is significantly larger than observed. This result does not necessarily contradict the results shown in the upper part of this figure. Since the effect of the northward transport of latent energy is not incorporated in this model, it may be reasonable to have a large eddy flux of sensible heat despite the relatively small energy flux required from radiative imbalance. This will be discussed further in a companion paper [18] on general circulation simulations with a simple hydrologic cycle.

The latitudinal distributions of various heat balance components in the atmosphere are plotted in figure 5B3. In general, the heating effect of convection from the earth's surface is mostly compensated for by the cooling

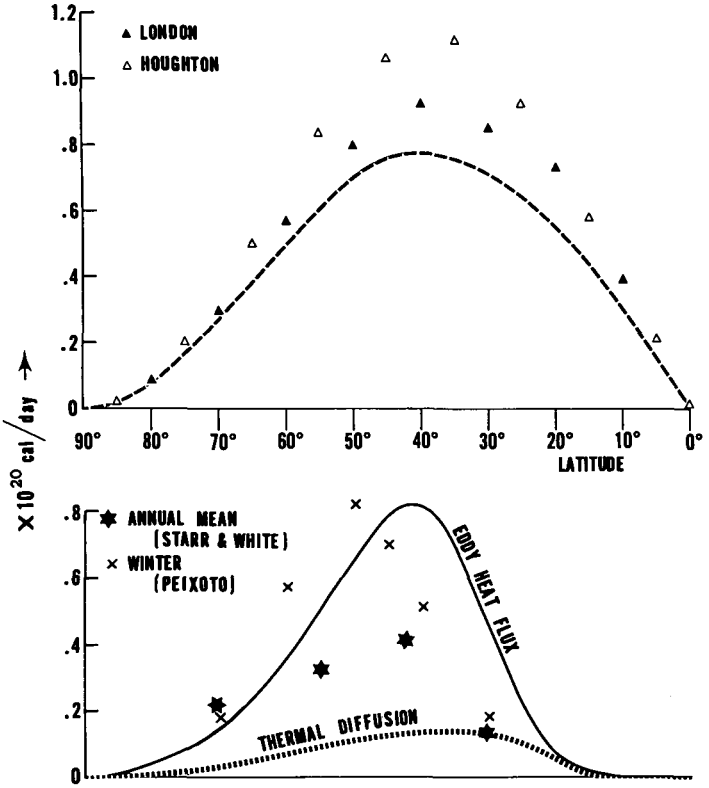

FIGURE 5B2.—In the upper part of the figure, the northward flux of the total energy expected from radiative imbalance is shown by a dashed line. Also, the flux obtained by Houghton [7] and that computed from the results of London [14] for the actual atmosphere are plotted. In the lower part of the figure, the northward flux of heat due to large-scale eddies and that due to subgrid-scale diffusion are shown by solid and dotted lines, respectively. The northward flux of heat due to large-scale eddies in the actual atmosphere for winter (Peixoto [26]) and the annual mean (Starr and White [39]) are also plotted.

effect of radiation. The remaining imbalance is taken up by the effect of large-scale motions. In the Tropics, the cooling resulting from the meridional circulation plays an important role; in the middle latitudes the effect of the meridional circulation and that of the eddies more or less compensate each other; and in higher latitudes the heating produced by the convergence of eddy flux of sensible heat predominates. Accordingly, the net effect of the large-scale motion is cooling at low latitudes and heating at high latitudes. Note that the temperature change caused by the meridional circulation and by the eddies involves the effect of adiabatic heating as well as that of the convergence of sensible heat transport. The subgrid-scale transport of sensible heat plays a minor role in the heat budget.

C. VERTICAL DISTRIBUTION OF HEAT BALANCE COMPONENTS

In figure 5C1 are shown the calculated vertical distributions of the hemispheric mean values of various heat balance components. According to this figure, the stratosphere as a whole is in almost complete radiative equilibrium while in the troposphere the hemispheric mean temperature is maintained as the balance among convective heating, radiative cooling, and the somewhat smaller effect of large-scale motions. In figure 5C2, the vertical distributions of heat flux resulting from the meridional circulation and large-scale eddies are shown together with the temperature change caused by adiabatic expansion and divergence of heat flux. As one might expect from the theory of baroclinic instability, the large-scale eddies transport heat upward except in the stratosphere and tend to stabilize the static stability of the troposphere and counteract the net effect of radiation and convection. The hemispheric mean temperature change caused by the meridional circulation is relatively small.

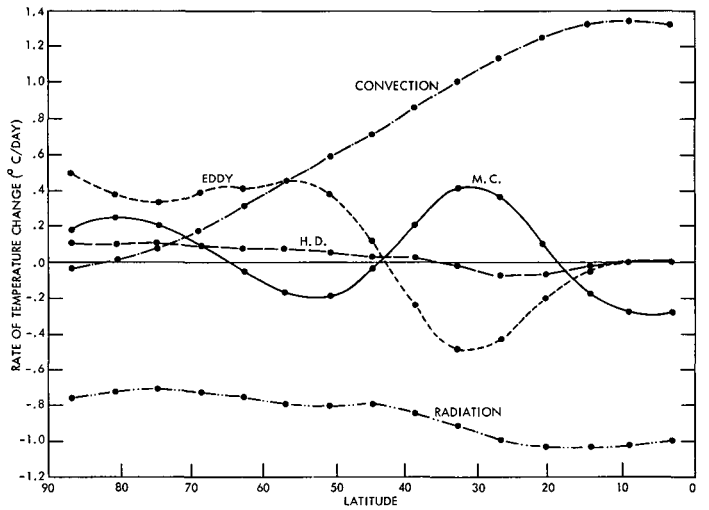

FIGURE 5B3.—The latitudinal distribution of temperature change due to convection, radiation, meridional circulation (M.C.), large-scale eddies (EDDY), and horizontal subgrid-scale mixing (H.D.) are shown.

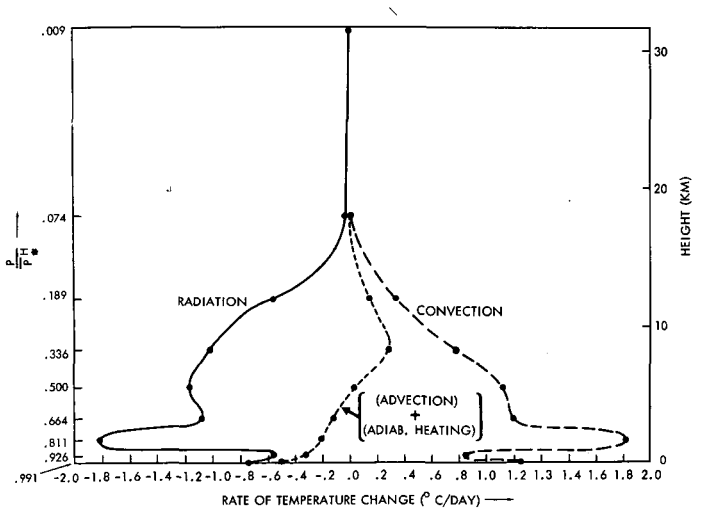

FIGURE 5C1.—The simulated vertical distribution of the hemispheric mean of the temperature change due to radiation, convection, and large-scale motion (advection and adiabatic heating) are shown.

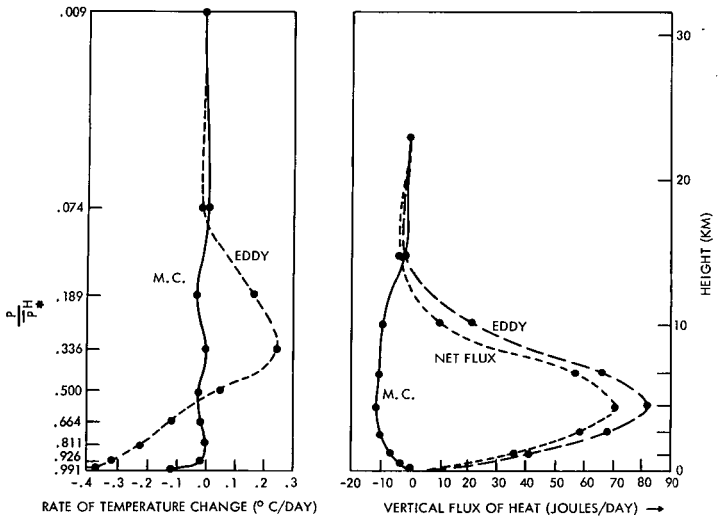

FIGURE 5C2.—On the left side of the figure are shown the vertical distributions of the rate of net temperature change (on the constant Q-surfaces) due to adiabatic expansion and divergence of heat flux by the meridional circulation (M.C.) and by large-scale eddies (EDDY). On the right side, the vertical distributions of heat flux on constant Q-surfaces due to meridional circulation (M.C.), large-scale eddies (EDDY), and to both (NET FLUX) are shown. Units: joules cm.$^{-2}$ day,$^{-1}$ right side. Upward flux is positive.

D. LATITUDE-HEIGHT DISTRIBUTION OF HEAT BALANCE COMPONENTS

Figure 5D1 shows the latitude-height distribution of net temperature change caused by radiation. Comparing this result with the corresponding distribution obtained by London [14] for the actual atmosphere, one can find many common features, i.e., the rapid decrease with increasing altitude of radiative cooling of the upper troposphere, the relatively large cooling in the tropical troposphere, and the strong cooling in the low cloud layer. This strong cooling due to the existence of low cloud is somewhat exaggerated in our calculation since we assumed the low clouds to be too thin. In the stratosphere weak heating occurs at low latitudes and cooling at higher latitudes. Similar features appeared in the heat balance computations performed by Ohring [23], Manabe and Möller [16], Davis [6], and Kennedy [9] for the actual atmosphere. The rate of cooling in high latitudes for the computed stratosphere is much smaller than that obtained in any of these studies. The failure to get a sufficiently warm stratosphere in higher latitudes (see section 4A) is the major reason for this discrepancy. (The cooling rate obtained by Ohring [23] and Davis [6] in the higher latitude stratosphere is somewhat larger than that obtained by Manabe and Möller [16] or by Kennedy [9] mainly because of their assumption of a humid stratosphere in higher latitudes.)

In the middle and lower parts of figure 5D1 are shown the latitude-height distribution of the rate of temperature change due to solar radiation and that due to long-wave radiation. In the top stratospheric level, heating resulting from the absorption of solar ultraviolet radiation by ozone

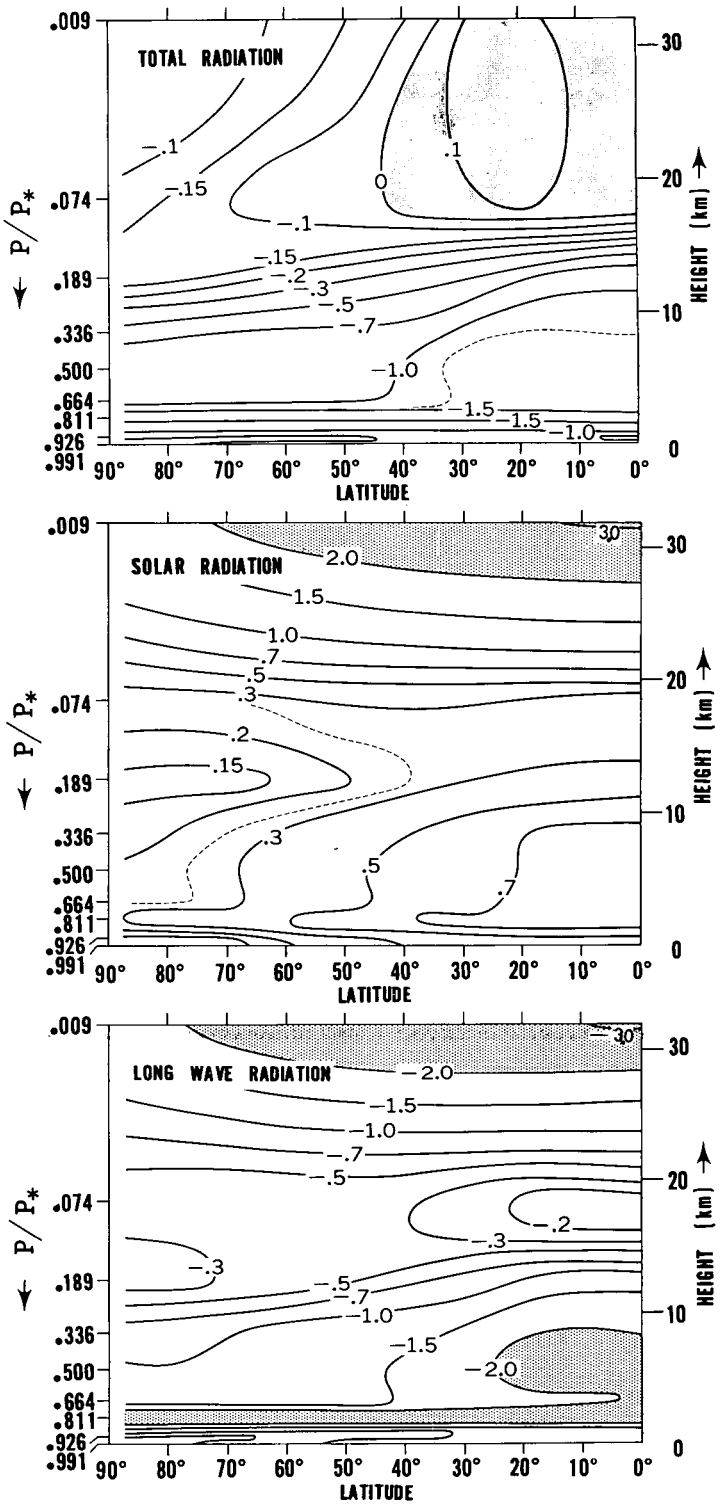

FIGURE 5D1.—Upper, middle, and lower parts of the figure give the latitude-height distributions of calculated temperature change (°C./day) due to the net rate of radiation, the solar radiation only, and long-wave radiation only.

is compensated for by the cooling caused by the long-wave radiation of carbon dioxide and water vapor. Around the level of the tropopause, both the effect of solar radiation and that of long-wave radiation are small, and they are in rather delicate balance. In the troposphere, the

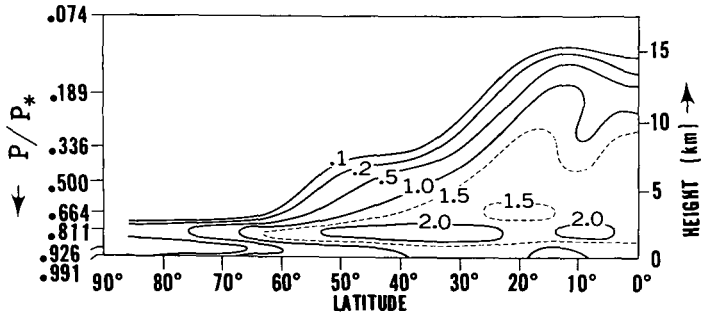

FIGURE 5D2.—The latitude-height distribution of calculated net temperature change (°C./day) due to conduction from the earth's surface and to the moist adiabatic adjustment.

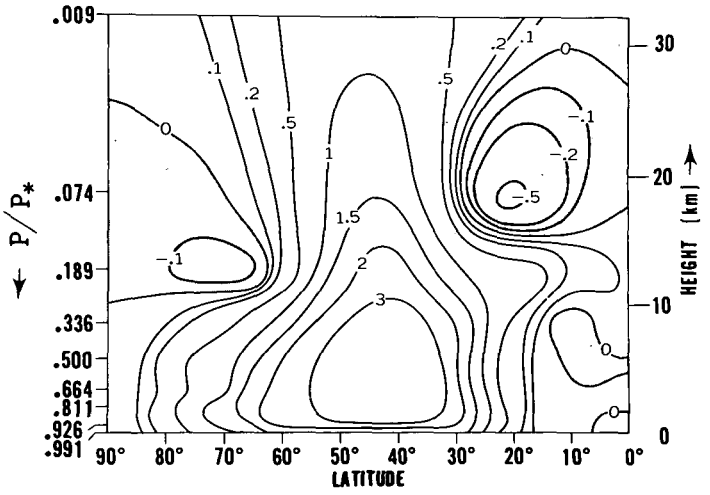

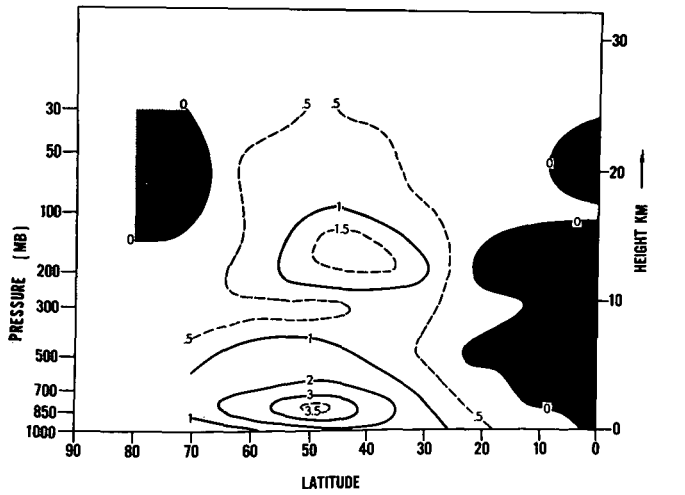

FIGURE 5D3.—The upper part of the figure shows the latitude-height distribution of the calculated poleward eddy transport of heat on isobaric surfaces. In the lower part of the figure the northward heat transport obtained by Starr and White [39] for the year 1950 is shown. Units are 10^{17} joule mb.$^{-1}$ day.$^{-1}$

cooling due to the long-wave radiation of water vapor outweighs the heating due to the solar radiation absorption by water vapor. The net radiative cooling in the troposphere is compensated for by convective heating originating from the earth's surface. Refer to the paper by Manabe and Strickler [17] for the details of the vertical distribution of the contributions of various gases.

The latitude-height distribution of the rate of temperature change due to conduction at the earth's surface and moist convective adjustment is shown in figure 5D2. As one would expect, the thickness of the moist convective layer is deeper in the Tropics than in high latitudes. The depth of this layer is about 12 km. in the Tropics and monotonically decreases with increasing latitude. In our model, the moist convective adjustment is very active in subtropics where the observed rainfall is at a minimum. This unreasonable result is the direct consequence of the adjustment process which disregards the effect of relative humidity on the moist convective process. We will be able to discuss this matter in more detail in the following companion paper [18] on the general circulation model with a hydrologic cycle.

So far we have examined the latitude-height distribution of temperature change due to radiation and convective adjustment. Another important factor is the effect of large-scale eddies. Figure 5D3 shows the latitude-height distribution of the northward transport of heat both in our model and in the actual atmosphere. In the real atmosphere, the area of the maximum transport of heat appears in the lower and upper part of the mid-latitude troposphere, whereas our model has a maximum in the lower troposphere but fails to have another maximum in the upper troposphere. In the tropical troposphere of our model atmosphere, extremely weak southward transport appears. Recently Starr and Wallace [40] pointed out the existence of a counter-gradient flux of heat in the tropical troposphere. Since the magnitude of the negative flux obtained from our computation is very small, this coincidence with observation may not be significant.

The latitude-height distribution of the calculated vertical heat flux is shown in figure 5D4 together with that of the actual atmosphere obtained by Jensen [8] for April. According to this figure, the upward flux of heat predominates in the troposphere except in the Tropics where a very weak downward flux of heat appears. In the stratosphere of our model atmosphere, the area of downward eddy heat transport occupies most of the area. Similar features are noticeable in the results of Jensen [8].

The net effect of these eddy fluxes of heat (including the effect of adiabatic heating or cooling caused by eddies) upon the rate of temperature change is shown in figure 5D5. In middle latitudes large-scale eddies make a significant contribution toward stabilizing the atmosphere. According to our results, the height of maximum stabilization decreases with increasing latitude. In higher latitudes it is very close to the earth's surface and contributes significantly to the maintenance of the inversion in the lower troposphere of high latitudes. Despite this stabilizing effect, the calculated area of stable layer in high latitudes is much smaller than the observed area. The existence of a relatively warm sea surface around the polar cap may be partly responsible for the maintenance of the strong inver-

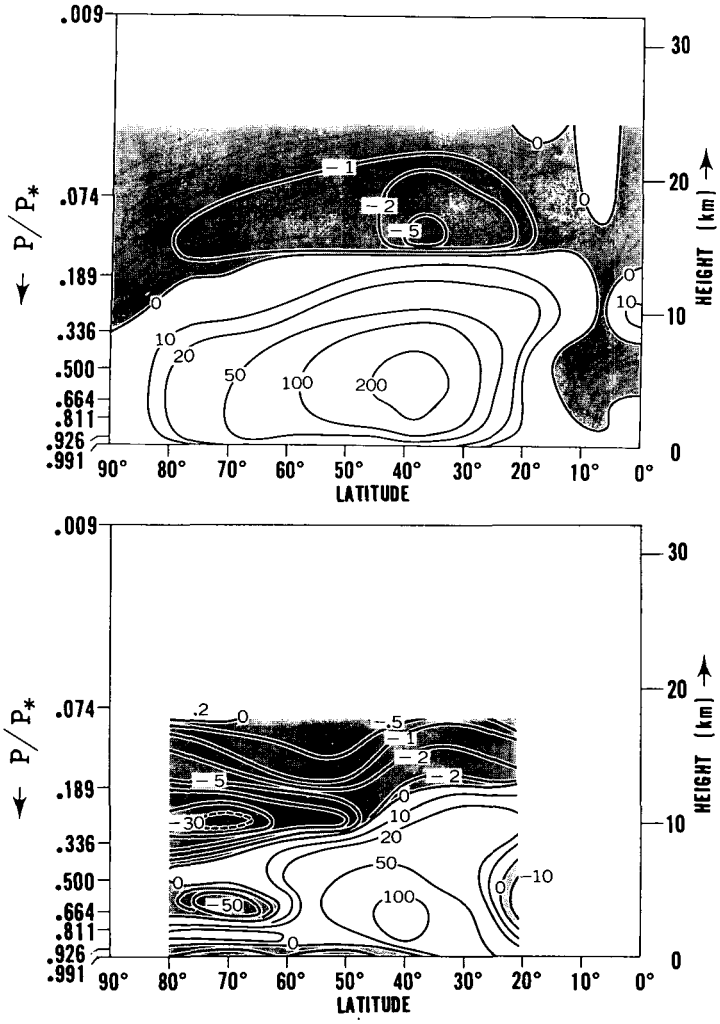

FIGURE 5D4.—The upper part of the figure gives the latitude-height distribution of the calculated vertical eddy flux of heat on isobaric surfaces. The lower part gives that obtained by Jensen [8] for the actual atmospheric transient eddy component for April. Units are joule cm.$^{-2}$ day.$^{-1}$

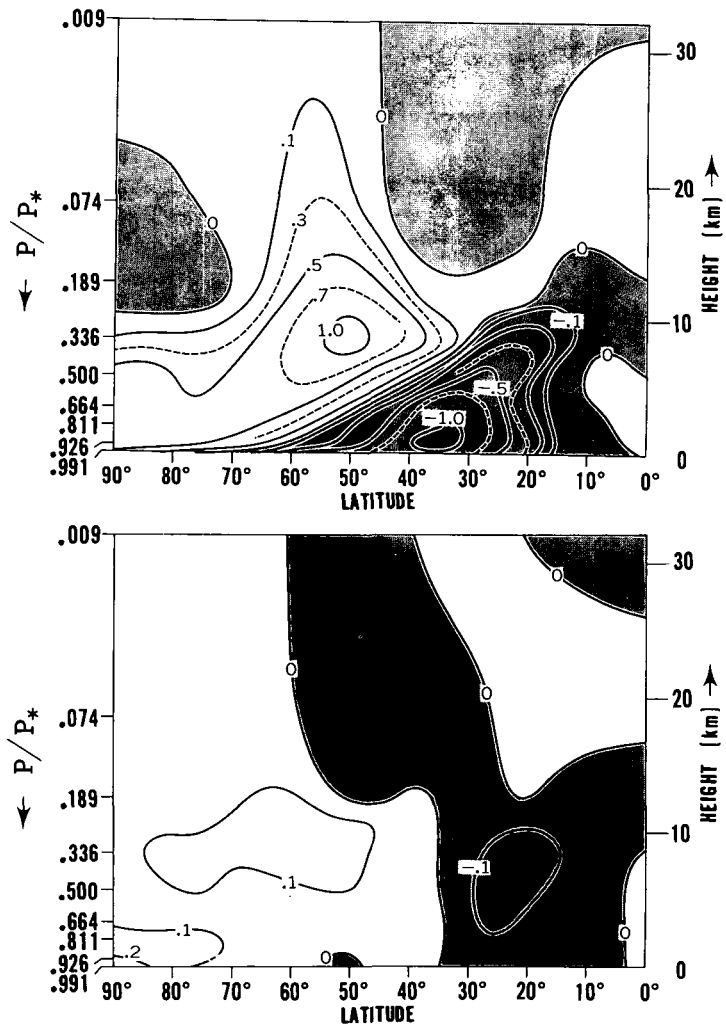

FIGURE 5D5.—The latitude-height distributions of the rate of temperature change (°C./day) due to large-scale eddies and subgrid-scale mixing are shown in the upper and lower parts of the figure, respectively.

sion in the actual winter atmosphere. Further study on this subject is desirable.

Next we shall examine the heat balance of the stratosphere. Figure 5D6 shows the latitudinal distribution of the rates of temperature change due to various heat balance components at model level 2 ($P/P_*=0.074$) in the stratosphere. According to this figure, the direct meridional circulation in lower latitudes contributes to the latitudinal increase of temperature there. The large-scale eddies transport heat northward (counter-gradient in lower latitudes) and help maintain the high temperatures in higher latitudes. The net effect of the large-scale eddies is cooling in the subtropics and heating in high latitudes. The magnitude of this effect, however, is far from sufficient to produce the observed temperature reversal in the stratosphere because of the counteracting effect of the polar cell. The temperature of this level increases about 14° C. from the equator to middle latitudes, but decreases with increasing latitude in the higher latitudes. Accordingly, the net increase of computed temperature from equator to pole is only 5° C., which is much smaller than the observed annual mean increase of 20° C. For comparison, the annual mean rate of radiative temperature change obtained for the observed distribution of temperature is shown by the triangle symbols in figure 5D6. The cooling rate in the higher latitudes is much larger for the actual atmosphere than for the model atmosphere because of the higher observed temperatures in high latitudes. In summary, there is some tendency toward a latitudinal increase of temperature in the model's stratosphere, but further refinement of the model is needed to simulate the full magnitude of this property.

6. ANGULAR MOMENTUM BALANCE

A. LATITUDINAL DISTRIBUTION OF ANGULAR MOMENTUM BUDGET

The distributions of northward transport of angular momentum which are due to large-scale eddies, meridional

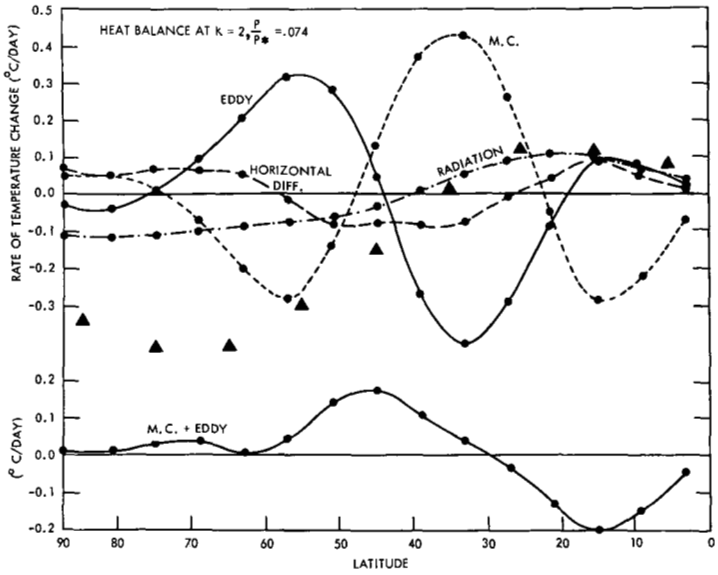

FIGURE 5D6.—In the upper part of the figure, the latitudinal distributions of the rate of temperature change due to various heat balance components at the second model level ($k=2$, $P/P_*=0.074$) are shown. The triangles show the annual mean rate of radiative temperature change at this level computed for the observed temperature distribution. In the lower part of the figure, the net temperature change due to large-scale eddies and the meridional circulation is shown.

circulation, and subgrid-scale mixing are shown in figure 6A1 together with the eddy transport of the actual atmosphere obtained by Starr and White [39] and Buch [4]. According to this figure, the calculated latitude of maximum eddy transport is about 30° N. and coincides with that of the actual atmosphere. The magnitude of the maximum eddy flux, however, is somewhat larger than that of the actual atmosphere. The contribution of subgrid-scale mixing turned out to be about ¼ of that of the large-scale eddies. Figure 6A2 is presented to show how the angular momentum balance is maintained at each latitude by the above mechanisms. According to this figure, the positive angular momentum, which is supplied from the earth's surface in tropical latitudes and in very high latitudes, is transported into middle latitudes mainly by the large-scale eddies, and the accumulated momentum is returned to the earth's surface there. In middle latitudes, the westerly momentum is supplied by the convergence of absolute angular momentum by the large-scale eddies, and in the subtropics it is supplied by the meridional circulation.

B. LATITUDE-HEIGHT DISTRIBUTION OF ANGULAR MOMENTUM BUDGET

In figure 6B1 the latitude-height distribution of the northward eddy transport of angular momentum obtained from our model is compared with the observed transport obtained by Buch [4] Oort [24]. According to this figure, the height and latitude of the maximum northward eddy transport coincide very well with those of the actual atmosphere. The negative eddy transport in high latitudes,

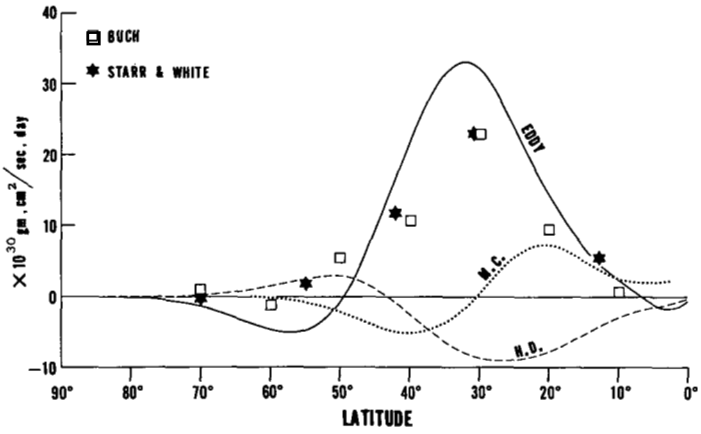

FIGURE 6A1.—The latitudinal distribution of northward transport of angular momentum due to various components. The transports due to meridional circulation, large-scale eddies, horizontal subgrid-scale mixing are shown by dotted, solid, and dashed lines, respectively. The annual mean values of momentum flux obtained by Starr and White [39] and those obtained by Buch [4] are plotted by stars and squares, respectively.

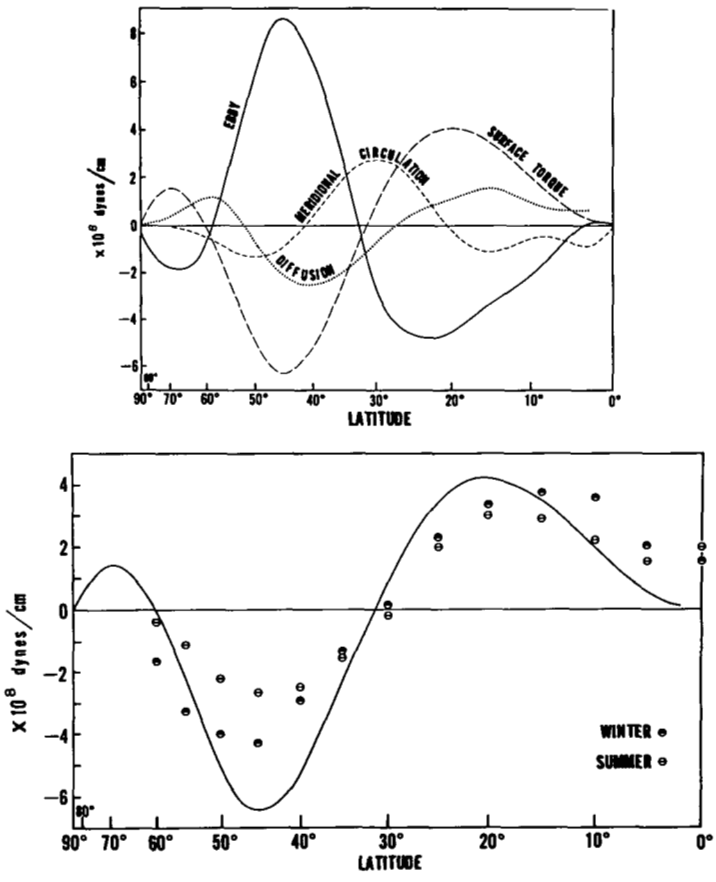

FIGURE 6A2.—The rates of the change of angular momentum due to meridional circulation, large-scale eddies, subgrid-scale diffusion, and surface torque are shown as functions of latitude. In the lower part of this figure the distribution of computed surface torque (solid line) is contrasted with the estimate of surface torque by Priestley [31] for the actual atmosphere (coded circles). The Priestley data are means for two hemispheres averaged by seasons.

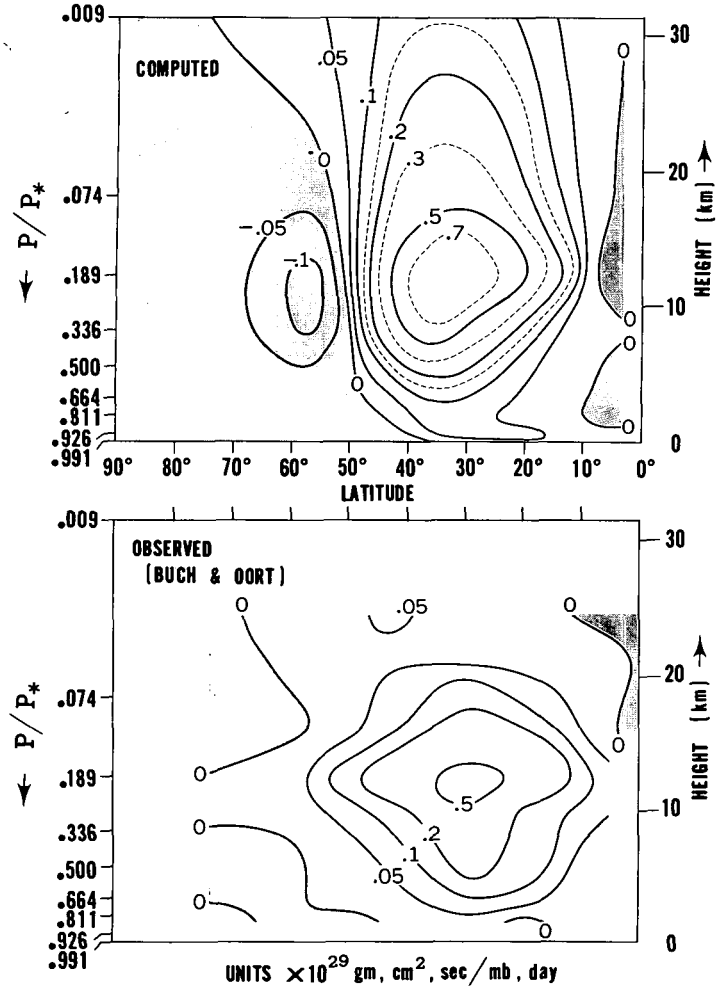

FIGURE 6B1.—The upper part of the figure shows the calculated latitude-height distribution of northward transport of angular momentum due to large-scale eddies. The lower part shows the corresponding distribution obtained by Buch [4] and Oort [24] for the actual atmosphere.

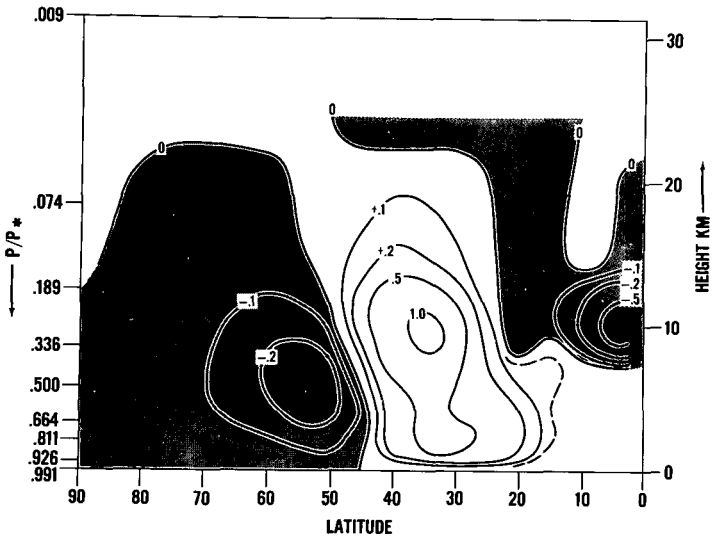

FIGURE 6B2.—Latitude-height distribution of vertical transport of angular momentum by the large-scale eddies. Unit is 10^{13} gm. sec.$^{-1}$ day.$^{-1}$

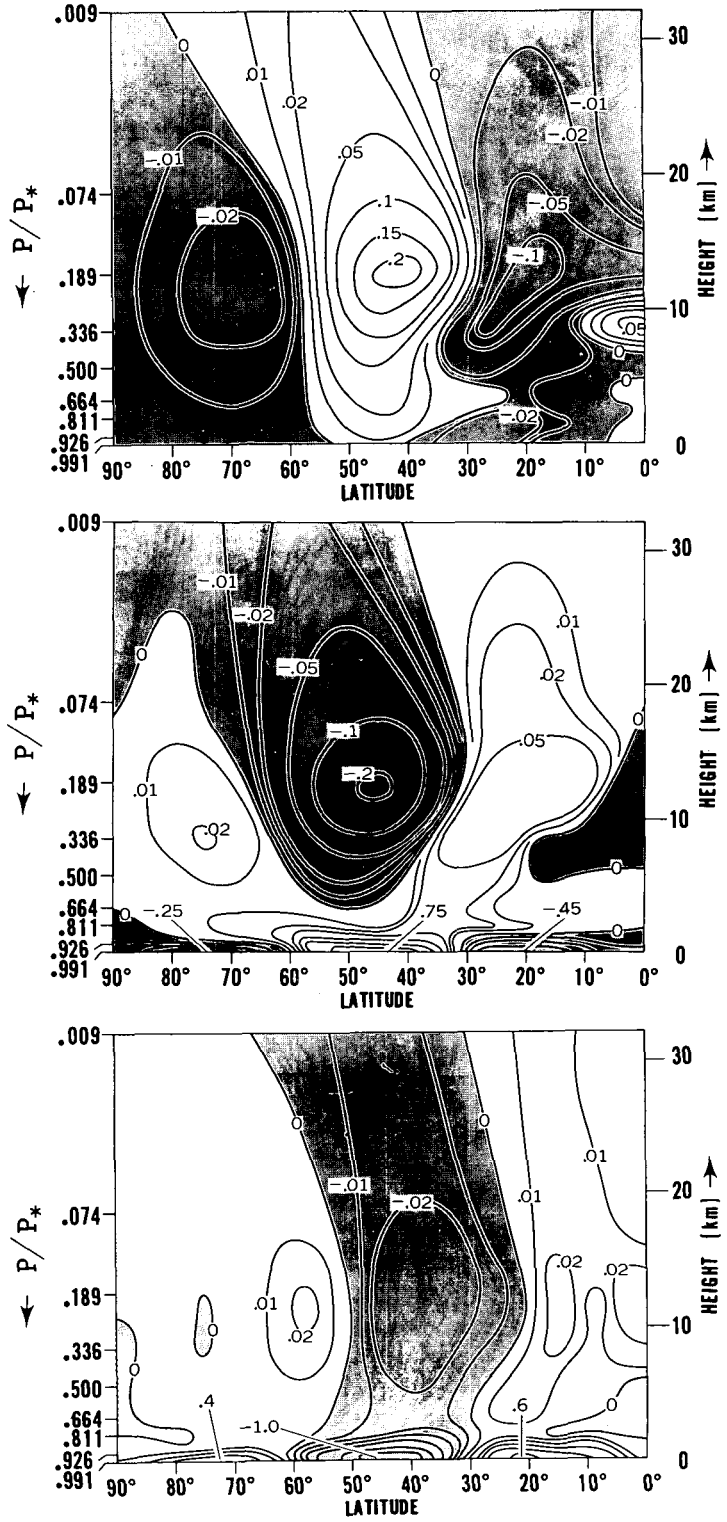

FIGURE 6B3.—The latitude-height distribution of the rate of change of relative angular momentum due to the large-scale eddies, the meridional circulation, horizontal and vertical subgrid-scale mixing are shown in the upper, middle, and lower parts of the figure, respectively. Units are 10^{12} gm. cm.^{2} sec.$^{-1}$. mb.$^{-1}$ day^{-1}.

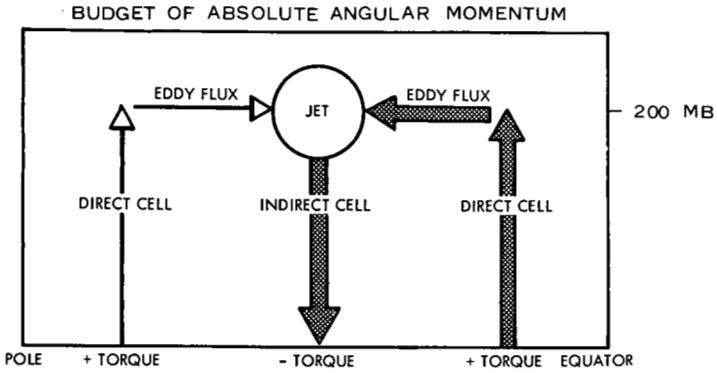

FIGURE 6B4.—Schematic representation of the flow of absolute angular momentum in the model atmosphere.

which is obtained in our model, does not appear clearly in these data for actual atmosphere. However, the results obtained by Obasi [22] for the Southern Hemisphere show significant negative transport at about 62° S.

The latitude-height distribution of vertical flux of angular momentum by large-scale eddies is shown in figure 6B2. It is interesting to note that the angular momentum is transported upward in middle latitudes where the jet stream predominates. In other words, it is transported against the gradient of momentum below the jet stream. Since this flux decreases with increasing altitude at the level of the jet stream, it supplies the momentum to the zonal current. The relative magnitude of this contribution is about 30 percent of that of the horizontal eddy transport.

In figure 6B3 the latitude-height distributions of the rate of the change of relative angular momentum due to the large-scale eddies, the meridional circulation, the horizontal subgrid-scale mixing, and the vertical mixing are shown. According to this figure, the absolute angular momentum created by surface torque in the tropical region is transported upward by the direct tropical cell and supplies the relative angular momentum in the upper troposphere near the equator. This relative angular momentum then is transported northward by the large-scale eddies. (Note that the eddy transport of angular momentum is at a maximum in the upper troposphere.) This eddy northward flux of relative angular momentum converges in middle latitudes, counterbalances the sink of relative angular momentum resulting from the indirect meridional circulation in middle latitudes, and thereby helps maintain the jet stream. Figure 6B4 gives a schematic representation of the flow of absolute angular momentum described here.

Finally, we should comment on the dependence of our results upon the vertical mixing coefficient adopted for our computation. As figure 6B3 shows, the change of angular momentum attributed to vertical mixing is very large in the planetary boundary layer and is compensated for mainly by the change of relative angular momentum due to the meridional circulation. This is why the very narrow belt of the meridional component of the wind sticks to the earth's surface as figure 4B3 shows. In other words, the degree of eccentricity of the meridional circulation of the atmosphere is mainly dominated by the thickness of the boundary layer or by the specified distribution of the vertical mixing coefficient near the earth's surface.

7. BUDGET OF KINETIC ENERGY AND AVAILABLE POTENTIAL ENERGY

The release of available potential energy in the troposphere has been the subject of many studies [42], [43], [11], [35]. According to Jensen [8] the maximum release takes place at about the 500-mb. level. It is very important to know how the energy, which is converted from potential energy, is distributed in the atmosphere. In connection with this problem, the mechanism for maintaining the kinetic energy in the stratosphere has received a great deal of attention recently. (See, for example, Barnes [2], Oort [24], Reed et al. [32], Miyakoda [21].) According to these authors, the release of eddy potential energy is negative and the kinetic energy of the stratospheric motion is maintained against dissipation by action from the troposphere. In this section we shall analyze the budget of available potential energy and that of kinetic energy in the model atmosphere in detail and compare them with those in the actual atmosphere whenever it is possible. It is hoped that the present analysis is useful for forming a coherent picture of the energy balance of the atmosphere.

A. ENERGY BALANCE FOR THE WHOLE ATMOSPHERE

Before becoming immersed in a detailed study of the energetics of the atmosphere, we constructed an energy diagram similar to the four-box diagram constructed by Phillips [27] and Smagorinsky [37]. Figure 7A1 shows the comparison among the energy diagram for our result,[3] that obtained by Smagorinsky and Phillips, and that compiled by Oort for the actual atmosphere. According to this comparison there is general qualitative agreement between the energy flow of the model atmosphere and that of the actual atmosphere. There are, however, the following quantitative discrepancies.

(1) The generation of available potential energy, and therefore the conversion of potential energy into kinetic energy, in the model atmosphere is significantly larger than that obtained by Oort [25] for the actual atmosphere. This discrepancy results from the absence of poleward transport of latent heat, of condensation, and of the ocean heat transport. All these act to decrease the latitudinal temperature gradient. Although the model of Phillips does not incorporate these effects, his heating function is deliberately modified to partially take these effects into

[3] The available potential energy adopted for the construction of this energy diagram is linearized and is defined by equation (4F1). This linearization is probably responsible for the relatively poor balance between the net generation and the conversion of the available potential energy because the non-linearized version, which is defined by equation (AII8), maintains a very good balance as table 3.2 shows.

792-517 O—65——4

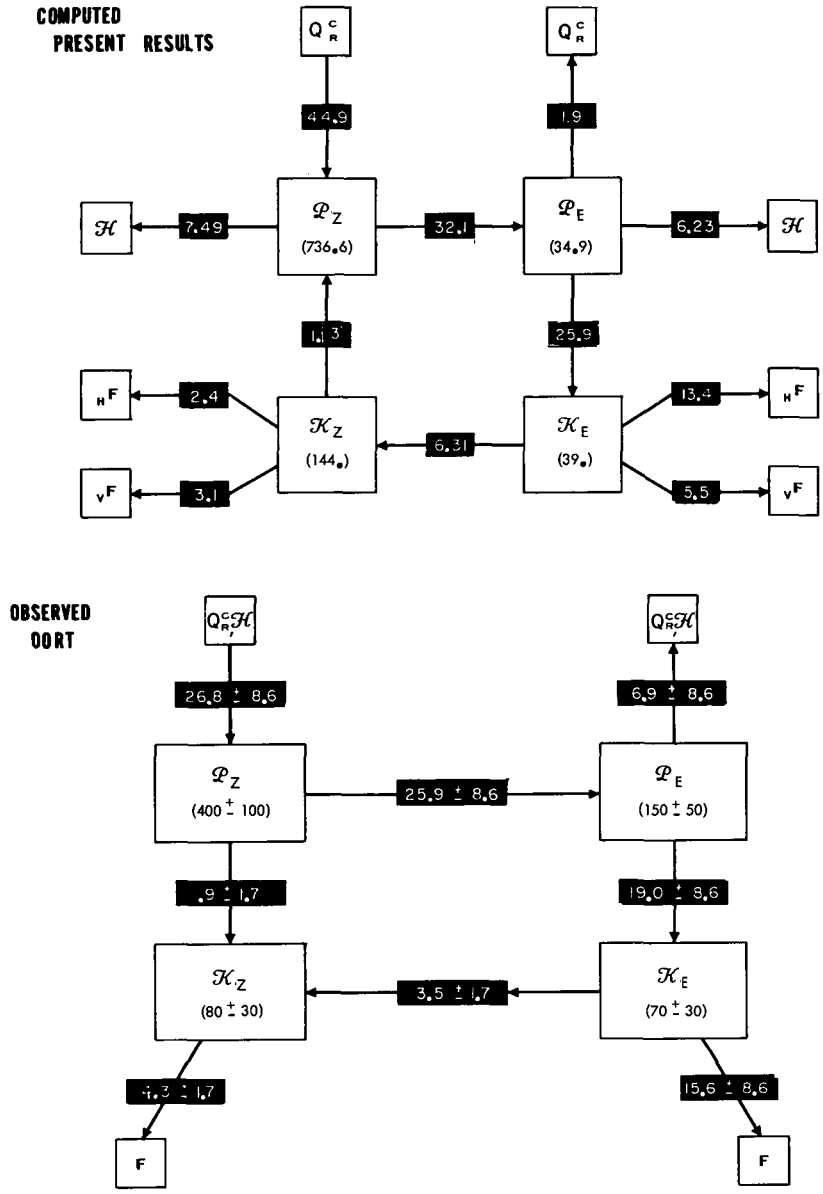

FIGURE 7A1.—In the upper and middle parts of the figure the energy diagram of the model and that compiled by Oort [25] for the actual atmosphere are shown. In the lower part the energy diagram obtained by Smagorinsky [37] is compared with that obtained by Phillips [27] (in parentheses in black boxes). $\mathcal{P}_Z$ and $\mathcal{P}_E$ are hemispheric means of zonal and eddy available potential energy, $\mathcal{K}_Z$ and $\mathcal{K}_E$ are hemispheric means of zonal and eddy kinetic energy, Q_R^C denotes the change of available potential energy by radiation and convection, $\mathcal{H}$ denotes the destruction of available potential energy by horizontal subgrid-scale mixing, and F, ${}_HF$, and ${}_VF$ indicate the total dissipation, dissipation by horizontal mixing, and that by vertical mixing respectively. The unit of energy transformation is 10^{-3} joule cm.$^{-2}$ mb.$^{-1}$ day^{-1} and that of energy itself is joule/cm.^{2}

account. Accordingly, the magnitude of the generation of available potential energy of his model is somewhat smaller than in our model atmosphere.

(2) The ratios $\mathcal{K}_E/\mathcal{K}_Z$ and $\mathcal{P}_E/\mathcal{P}_Z$ are computed to be much smaller than the observed values, although they are somewhat larger in our results than in the earlier two-level calculations (Smagorinsky [37]). One of the reasons for this discrepancy may be the absence of surface asymmetries as discussed earlier.

(3) The transfer of eddy kinetic energy into zonal kinetic energy in our model atmosphere is larger than that estimated by Oort [25] for the actual atmosphere, though it is somewhat smaller than the energy transfer obtained by either Phillips or Smagorinsky. This result is consistent with the very strong jet stream which we obtained in our computation. (See section 4B.)

B. TOTAL KINETIC ENERGY BUDGET

For the sake of simplicity of interpretation of results, a pressure coordinate system is used instead of a σ-coordinate system. The equation for the rate of change of kinetic energy in the pressure coordinate system is

$$\frac{\partial K}{\partial t}=-\nabla\cdot(\mathbf{V}K)-\frac{\partial}{\partial P}(\omega K)-\mathbf{V}\cdot\nabla\phi+\mathbf{V}\cdot\mathbf{F} \quad (7B1)^4$$

where $\mathbf{V}$ is earth velocity, $\mathbf{F}$ is frictional force, and

$$K=\tfrac{1}{2}\mathbf{V}^2 \quad (7B2)$$

Using the continuity equation, we obtain

$$-\mathbf{V}\cdot\nabla\phi=-\omega\alpha-\left(\nabla\cdot(\mathbf{V}\phi)+\frac{\partial}{\partial P}(\omega\phi)\right) \quad (7B3)$$

The equation for the rate of change of hemispheric mean of K is

$$\frac{\partial\overline{K}^H}{\partial t}=-\frac{\partial}{\partial P}\overline{(\omega K)}^H-\overline{\omega\alpha}^H-\frac{\partial}{\partial P}\overline{(\omega\phi)}^H+\overline{\mathbf{V}\cdot\mathbf{F}}^H \quad (7B4)$$

where $\overline{(\ )}^H$ denotes the hemispheric mean; α is the specific volume of air, ϕ is geopotential height on an isobaric surface.

In equation (7B1) we shall refer to $-\mathbf{V}\cdot\nabla\phi$ and $\mathbf{V}\cdot\mathbf{F}$ as the source term and the sink term of kinetic energy respectively. In equation (7B4) the term $-\frac{\partial}{\partial P}\overline{(\omega\phi)}^H$ and the term $-\frac{\partial}{\partial P}\overline{(\omega K)}^H$ may be called the pressure interaction term and the transport term of total kinetic energy, respectively, and the term $-\overline{\omega\alpha}^H$ will be referred to as the conversion term of potential energy. Figure 7B1 displays the vertical distribution of the contribution of these terms to the rate of change of total kinetic energy. According to this figure the level of the maximum release of potential energy occurs at about 500 mb. As figure 7B2 shows the energy thus converted is transferred upward to the level of the jet stream and downward to the level of the surface

[4] This equation applies to isobaric surfaces uninterrupted by the earth's surface.

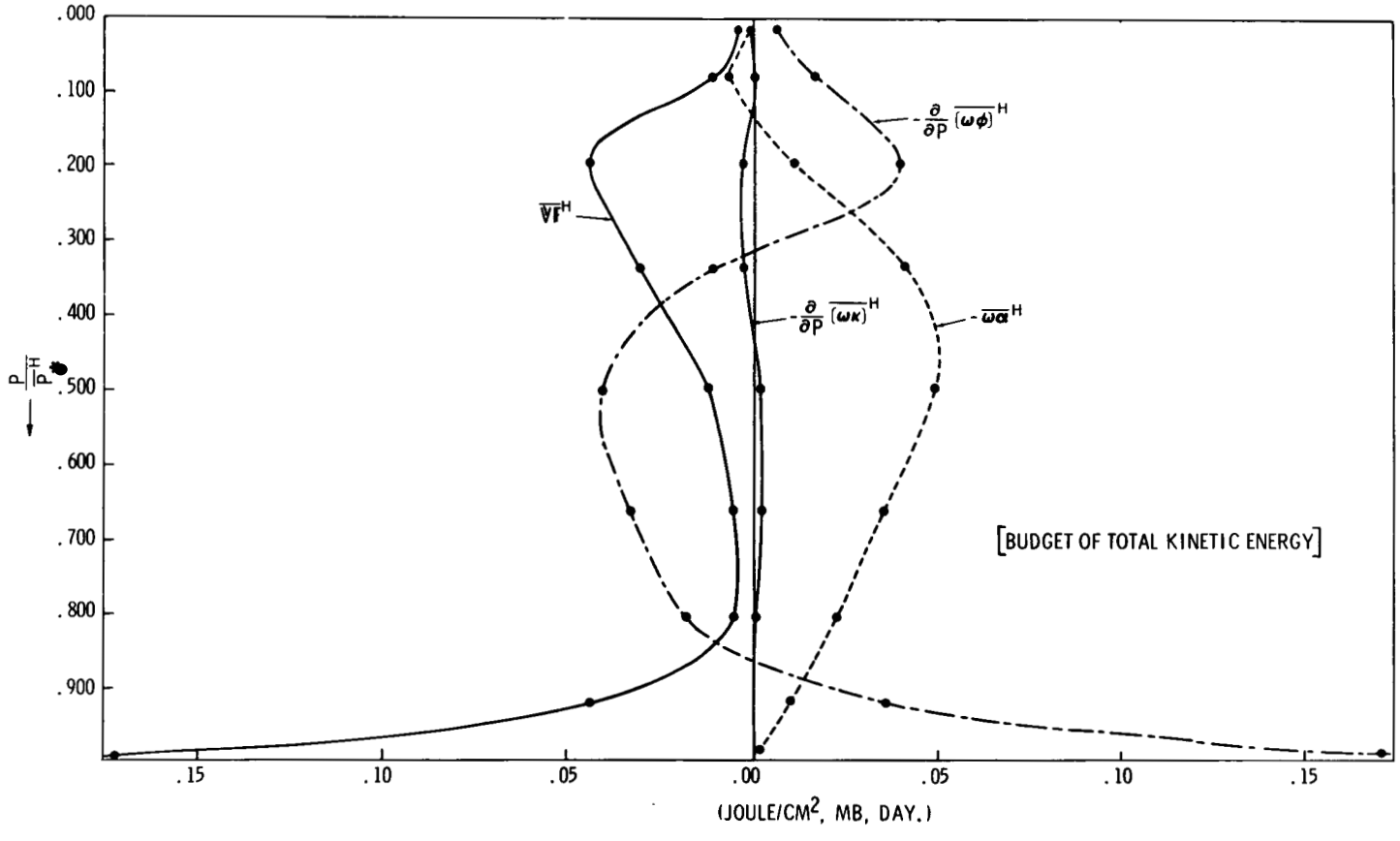

FIGURE 7B1.—Vertical distributions of the rate of change of kinetic energy on each isobaric surface due to various mechanisms.

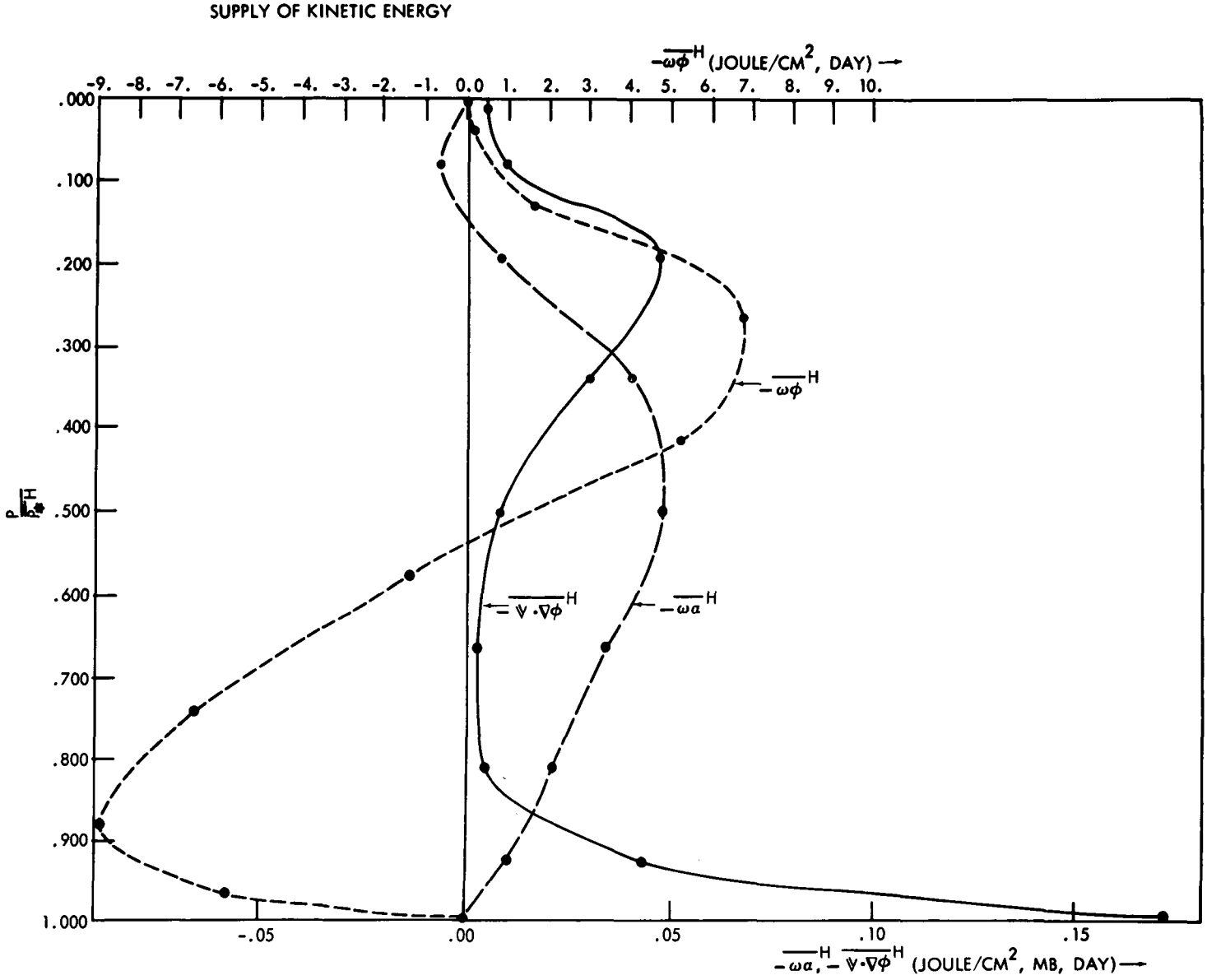

FIGURE 7B2.—Vertical distribution of $-\overline{\nabla\cdot\nabla\phi}^H$, $-\overline{\omega\phi}^H$, and $-\overline{\omega\alpha}^H$ on an isobaric surface.

boundary layer by the mechanism corresponding to the pressure interaction term $-\overline{\omega\phi}^H$. As a result of these energy transfers, the source term of kinetic energy $-\overline{\nabla\cdot\nabla\phi}^H$ is a maximum at these two levels. According to figure 7B1 these sources of kinetic energy are almost exactly compensated for by the sink of kinetic energy $\overline{\nabla\cdot\mathbf{F}}^H$, i.e., by dissipation. The effect of vertical transport of kinetic energy is negligibly small. Recently, Kung [12] computed the vertical distribution of the source term of kinetic energy over the North American Continent from observed wind data. It is encouraging that his results have a clear double maximum in the source term at the level of the jet stream and in the boundary layer as we predicted. According to Brunt [3] the dissipation of kinetic energy in the free atmosphere is approximately equal to that in the boundary layer. In the model atmosphere, the ratio of the dissipation above the 811-mb. level to that below the 811-mb. level is 1.60 to 1.00.

The equation for the change of the vertically integrated kinetic energy is

$$\frac{\partial\overline{\overline{K}^P}^\lambda}{\partial t}=-\frac{1}{a\cos\theta}\frac{\partial}{\partial\theta}\left(\overline{\overline{vK}^P}^\lambda\cos\theta\right)-\overline{\overline{\nabla\cdot\nabla\phi}^P}^\lambda+\overline{\overline{\nabla\cdot\mathbf{F}}^P}^\lambda \quad (7B5)^5$$

where v is the meridional component of the earth wind velocity and $\overline{(\ )}^P$ and $\overline{(\ )}^\lambda$ denote the mean operation with respect to pressure and longitude, respectively. In the

[5] Instead of equation (7B5), the following equation on the Q-coordinate system is adopted for the actual computation

$$\frac{\partial\overline{P_*\overline{K}^Q}^\lambda}{\partial t}=-\frac{1}{a\cos\theta}\frac{\partial}{\partial\theta}\left(\overline{\overline{P_*vK}^Q}^\lambda\cos\theta\right)-\overline{\overline{[P_*\nabla\cdot\nabla\phi+RT\nabla\cdot\nabla P_*]}^Q}^\lambda+\overline{\overline{\nabla\cdot\mathbf{F}}^Q}^\lambda \quad (7B6)$$

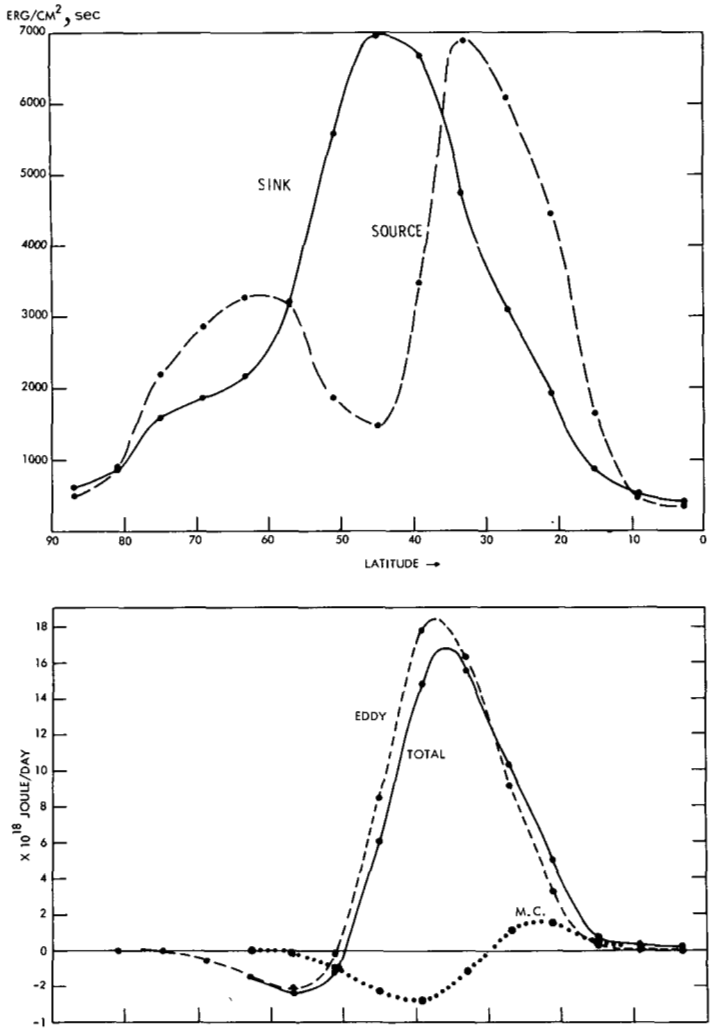

FIGURE 7B3.—In the upper part of the figure the distribution of the source term and sink term (dissipation) of total kinetic energy are shown as functions of latitude. In the lower part of the figure, the latitudinal distributions of northward flux of total kinetic energy due to the meridional circulation (M.C.), due to the large-scale eddies (EDDY), and due to both effects (TOTAL) are shown.

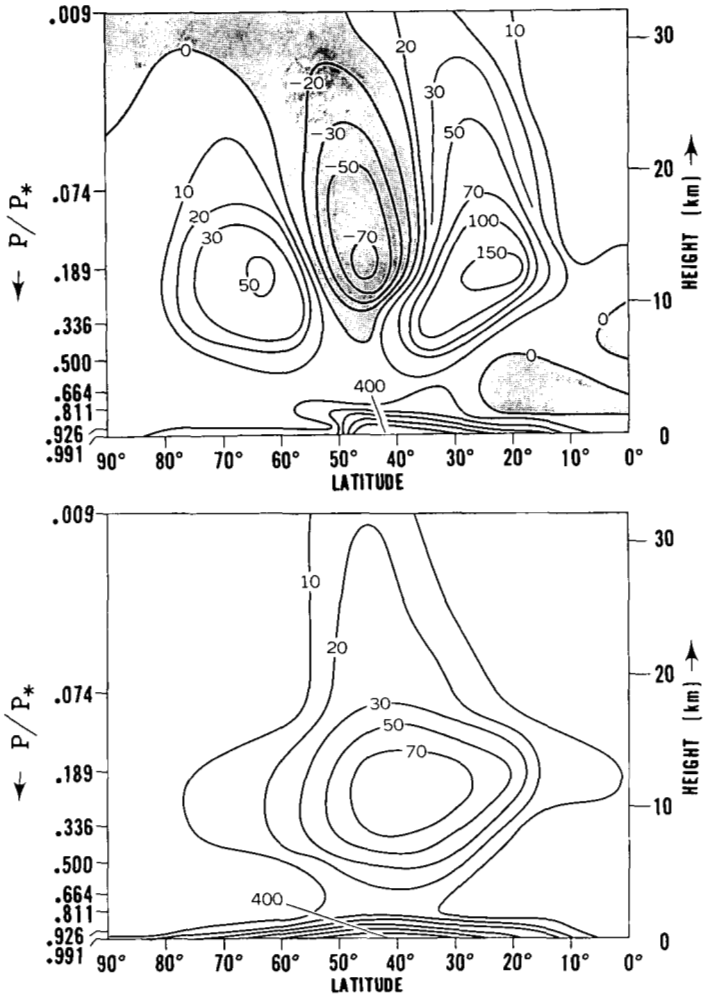

FIGURE 7B4.—The latitude-height distribution of the source term of kinetic energy is shown in the upper part of the figure. That of the sink term (dissipation) is shown in the lower part of the figure. Unit: 10^{-3} joule mb.$^{-1}$ day^{-1}.

upper and lower parts of figure 7B3 the latitudinal distribution of the source and the sink of kinetic energy are shown respectively. According to this figure, the latitude of maximum dissipation is about 45° N., and the latitudes of the primary and secondary maxima of the source term are about 32° N. and 62° N. As one may expect, the latitudinal distribution of the northward transport of kinetic energy, shown in figure 7B3, is very similar to that of the angular momentum shown in figure 6A1. Accordingly, the kinetic energy is transferred from the source region in the subtropics (or from high latitudes) into the sink region in middle latitudes. This transport compensates for the imbalance between the source and sinks of kinetic energy. Saltzman, Gottuso, and Fleisher [34] computed the latitudinal distribution of the northward transport of kinetic energy by the large-scale eddies at the 500-mb. level of the actual atmosphere. Their latitude of maximum poleward transport is approximately 40° N. and coincides with that of the model atmosphere. However, the weak southward transport, which appears in the model atmosphere around the latitudes of 50° to 70°, is missing in their distribution. The magnitude of maximum poleward transport is about 6×10^{15} joules day^{-1} mb.$^{-1}$ (annual mean) and coincides reasonably well with that of the model atmosphere at 500 mb. in which it is approximately 8×10^{15} joules day^{-1} mb.$^{-1}$ (See fig. 7B5.)

The latitude-height distribution of the sink of kinetic energy ($\mathbf{V}\cdot\mathbf{F}$) which is shown in the lower half of figure 7B4 is very similar to that of the eddy kinetic energy shown by figure 4E2 except in the area near the earth's surface, where the dissipation in the boundary layer predominates. It is interesting that the source term has a negative value in the upper troposphere of the middle latitudes. The kinetic energy is transported into

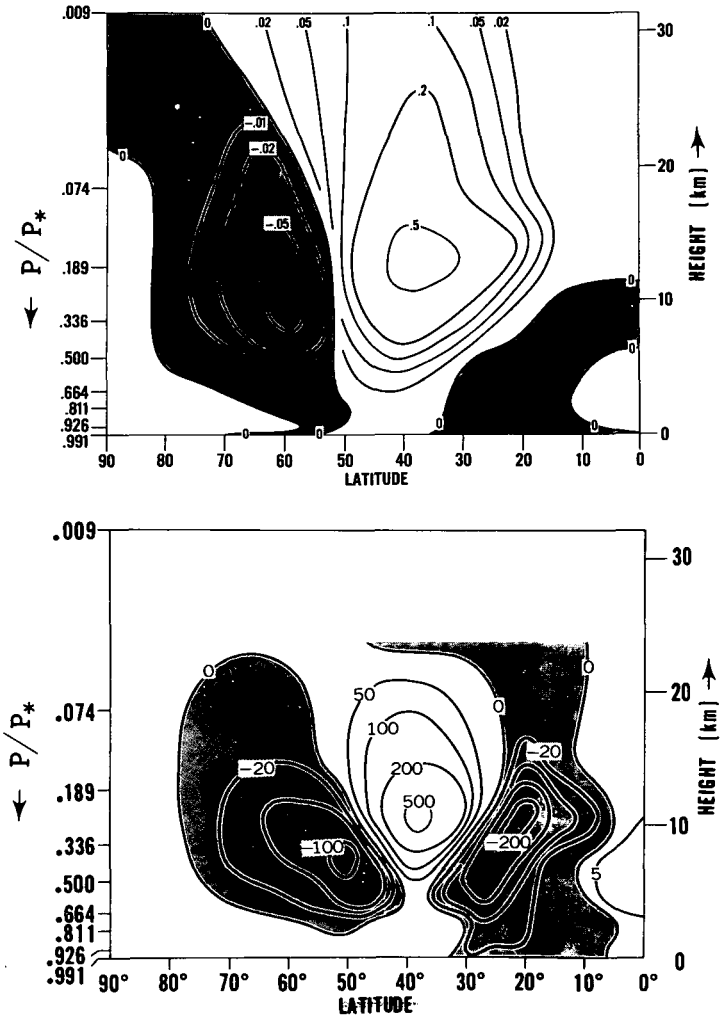

FIGURE 7B5.—The latitude-height distribution of the northward transport of total kinetic energy due to large-scale eddies is shown in the upper part of this figure (Unit: 10^{17} joule mb.$^{-1}$ day^{-1}) and that of the vertical transport of total kinetic energy due to large-scale eddies is shown in the lower part (Unit: 10^{-2} joule cm.$^{-2}$ day^{-1}).

this sink region from the source regions located on both sides. For comparison, the distribution of the poleward and vertical transports of total kinetic energy by the large-scale eddies is shown in figure 7B5.

C. EDDY AND ZONAL KINETIC ENERGY BUDGET

The equations for the rate of change of the hemispheric mean of eddy kinetic energy and of zonal kinetic energy may be written as follows:

$$\frac{\partial \overline{K_E}^H}{\partial t} = -\frac{\partial}{\partial P}\overline{(\omega K_E)}^H - \overline{\omega'\alpha'}^H - \frac{\partial}{\partial P}\overline{(\omega'\phi')}^H + \overline{\mathbf{V}'\cdot\mathbf{F}'}^H + \langle K_Z\cdot K_E\rangle_1 + \langle K_Z\cdot K_E\rangle_2 \quad (7C1)$$

$$\frac{\partial \overline{K_Z}^H}{\partial t} = -\frac{\partial}{\partial P}\overline{(\omega K_Z)}^H - \overline{\bar{\omega}^\lambda\bar{\alpha}^\lambda}^H - \frac{\partial}{\partial P}\overline{(\bar{\omega}^\lambda\bar{\phi}^\lambda)}^H + \overline{\bar{\mathbf{V}}^\lambda\cdot\bar{\mathbf{F}}^\lambda}^H - \langle K_Z\cdot K_E\rangle_1 - \langle K_Z\cdot K_E\rangle_2 \quad (7C2)$$

where $(\ )'$ denotes the deviation from zonal mean $\overline{(\ )}^\lambda$ and

$$K_E = \tfrac{1}{2}[(u')^2+(v')^2] \quad (7C3)$$

$$K_Z = \tfrac{1}{2}\left[\left(\bar{u}^\lambda\right)^2+\left(\bar{v}^\lambda\right)^2\right] \quad (7C4)$$

$$\langle K_Z\cdot K_E\rangle_1 \approx -\overline{\overline{u'v'}^\lambda \cos\theta \frac{1}{a}\frac{\partial}{\partial\theta}\left(\bar{u}^\lambda\sec\theta\right)}^H - \overline{\overline{\omega'u'}^\lambda\frac{\partial \bar{u}^\lambda}{\partial P}}^H \quad (7C5)$$

$$\langle K_Z\cdot K_E\rangle_2 \approx \frac{\partial}{\partial P}\overline{\left(\bar{u}^\lambda\cdot\overline{u'\omega'}^\lambda\right)}^H \quad (7C6)$$

where u is the zonal component of the earth wind velocity. We shall refer to $-\overline{\omega'\alpha'}^H$ and $-\overline{\bar{\omega}^\lambda\bar{\alpha}^\lambda}^H$ as the eddy conversion term and the zonal conversion term, $-\overline{\mathbf{V}'\cdot\mathbf{F}'}^H$ and $-\overline{\bar{\mathbf{V}}^\lambda\cdot\bar{\mathbf{F}}^\lambda}^H$ as the eddy dissipation and the zonal dissipation, and $-\overline{\omega'\phi'}^H$ and $-\overline{\bar{\omega}^\lambda\bar{\phi}^\lambda}^H$ as the eddy pressure interaction and zonal pressure interaction term, respectively. $\langle K_Z\cdot K_E\rangle_2$ represents the energy transfer from zonal kinetic energy into the eddy kinetic energy attributed to the vertical interaction term (Reynolds stress by the large-scale eddies) and $\langle K_Z\cdot K_E\rangle_1$ represents the remaining part of the transfer from K_Z to K_E.

In the upper part of figure 7C1, the vertical distributions of these terms contributing to the change of eddy kinetic energy are shown. As the upper part of figure 7C2 shows, the net effects of the eddy conversion of potential energy and the eddy pressure interaction term create double maxima in the distribution of the source of eddy kinetic energy at the level of the jet stream (200-mb. level) and in the boundary layer. According to figure 7C1, the upper tropospheric maximum in the source of eddy kinetic energy is mainly compensated for by dissipation through horizontal mixing and the maximum in the boundary layer is mainly compensated for by dissipation through vertical mixing. Although the magnitude of the eddy pressure interaction term decreases remarkably with increasing altitude at the level of the jet stream, it supplies a significant amount of energy to the stratosphere and constitutes a major source of kinetic energy there.

In the lower half of figure 7C1 are the vertical distributions of the terms contributing to the change of zonal kinetic energy. As we stated already, the maximum transfer from eddy kinetic energy into zonal kinetic energy takes place at about the 200-mb. level and constitutes a major source of zonal kinetic energy. Part of this zonal kinetic energy is dissipated at the same level and part is transferred by the zonal pressure interaction term into the surface boundary layer where dissipation predominates. (See the lower half of fig. 7C2.) Since the zonal pressure interaction term is estimated as a small difference between two larger quantities, the accuracy of the computation of its contribution is rather low. It is hoped, however, that the general qualitative features of its contribution are correctly evaluated. Figure 7C3 shows the summary of the budget which we have described so far.

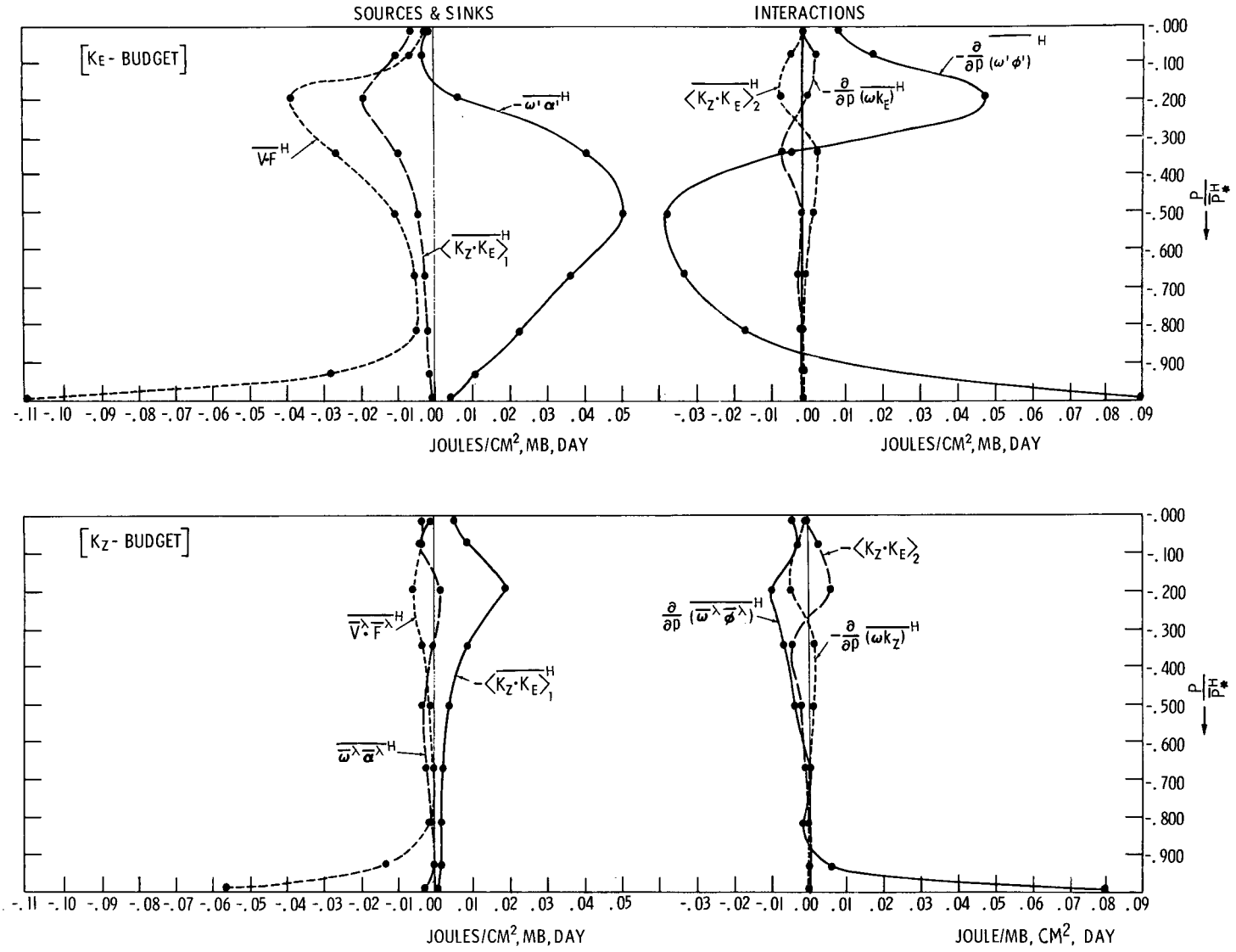

FIGURE 7C1.—The vertical distributions of the rate of change of eddy kinetic energy due to various terms on an isobaric surface are shown in the upper part of the figure, and those of the rate of change of zonal kinetic energy are shown in the lower part.

Finally, we shall examine the latitude-height distribution of some of these terms. In the upper and lower parts of figure 7C4, the latitude-height distribution of the eddy conversion term and that of the eddy pressure interaction term are shown, respectively. According to this figure, the eddy conversion of potential energy to kinetic energy has a maximum at about the 500-mb. level in middle latitudes. In the stratosphere, it has a small negative value except around 50° latitude where some very weak positive conversion appears. Similar distributions of the eddy conversion term were obtained by Jensen [8] and Miyakoda [21]. In the tropical troposphere, there are regions of extremely weak conversion of potential energy. Further study is desirable to determine how significant these negative regions are. It is reasonable that the eddy interaction term $-\overline{\omega'\phi'}^H$ has a maximum value in the upper troposphere of middle latitudes or just below the region of maximum eddy kinetic energy where dissipation may predominate.

D. TOTAL AVAILABLE POTENTIAL ENERGY BUDGET

The equation for the rate of change of the hemispheric mean values of A_T (see equation 4F1) in the pressure coordinate system may be written as follows:

$$\frac{\partial \overline{A_T}^H}{\partial t} = -\frac{\partial}{\partial P}\overline{(\omega A_T)}^H + \overline{\omega\alpha}^H + \frac{\gamma}{c_p}\overline{T'''\cdot\dot{q}'''}^H + (CR) \qquad (7D1)^6$$

where

$$\dot{q} = \dot{q}_C + \dot{q}_{RAD} + \dot{q}_{HD} \qquad (7D2)$$

$$(CR) = \overline{\omega A_T}^H \left\{ \frac{\partial}{\partial P} \log_e \left[\gamma \left(\frac{T}{\Theta} \right)^2 \right] \right\} \qquad (7D3)$$

[6] This equation and equations (7E1) and (7E2) apply to isobaric surfaces uninterrupted by the earth's surface. The part of the change of A_T due to the change of γ is neglected.

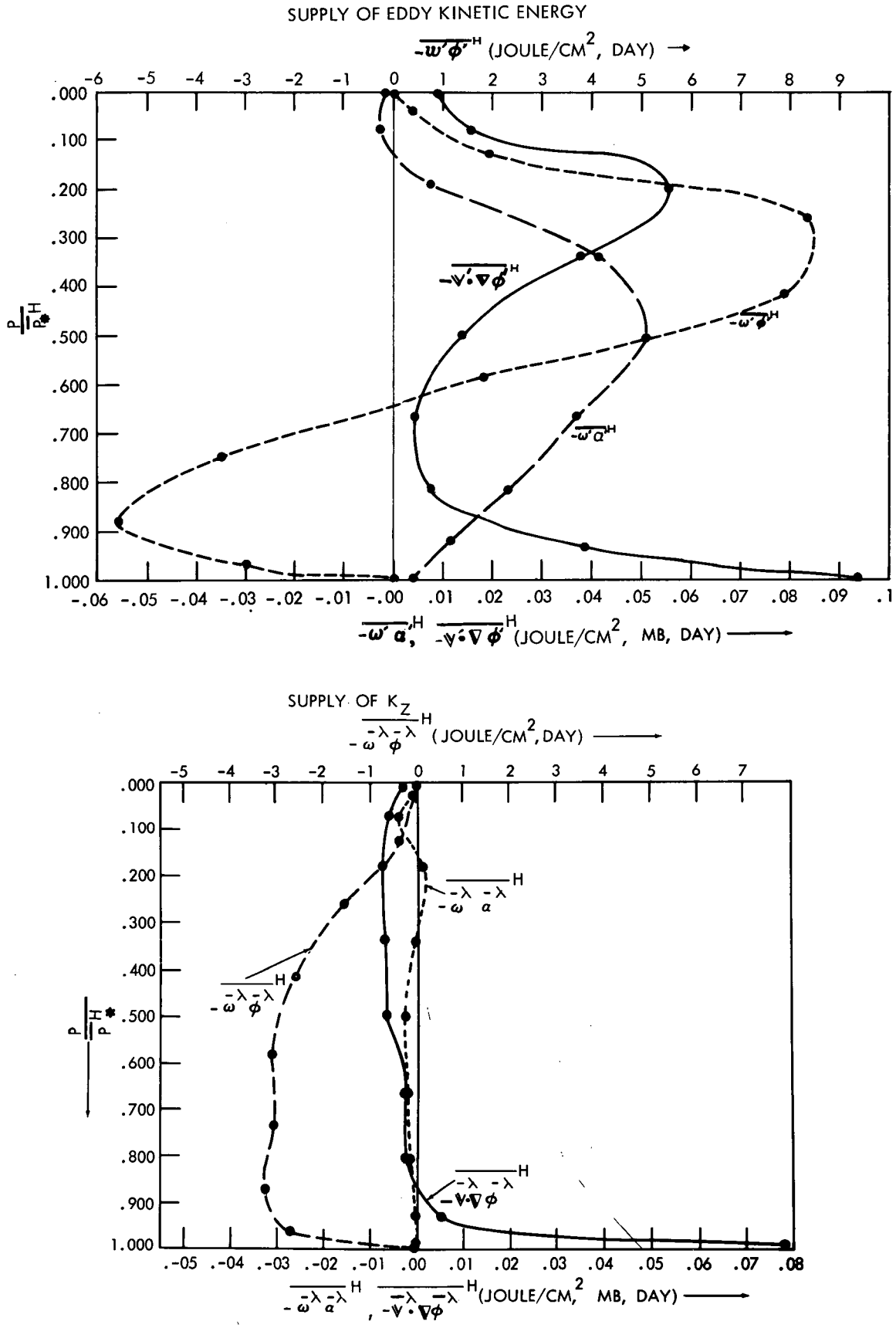

FIGURE 7C2.—The vertical distributions of $-\overline{\nabla'\cdot\nabla\phi'}^H$, $-\overline{\omega'\alpha'}^H$, and $-\overline{\omega'\phi'}^H$ are shown in the upper part of the figure and those of $-\overline{\overline{\nabla}^{\lambda}\cdot\nabla\overline{\phi}^{\lambda}}^H$, $-\overline{\overline{\omega}^{\lambda}\overline{\alpha}^{\lambda}}^H$, and $-\overline{\overline{\omega}^{\lambda}\overline{\phi}^{\lambda}}^H$ are shown in the lower part of the figure. These terms are on isobaric surfaces.

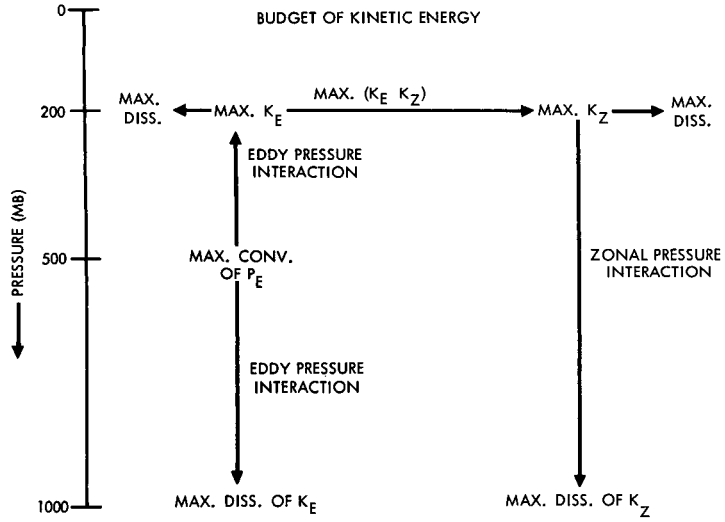

FIGURE 7C3.—Schematic diagram showing the vertical distributions of the budget components of kinetic energy.

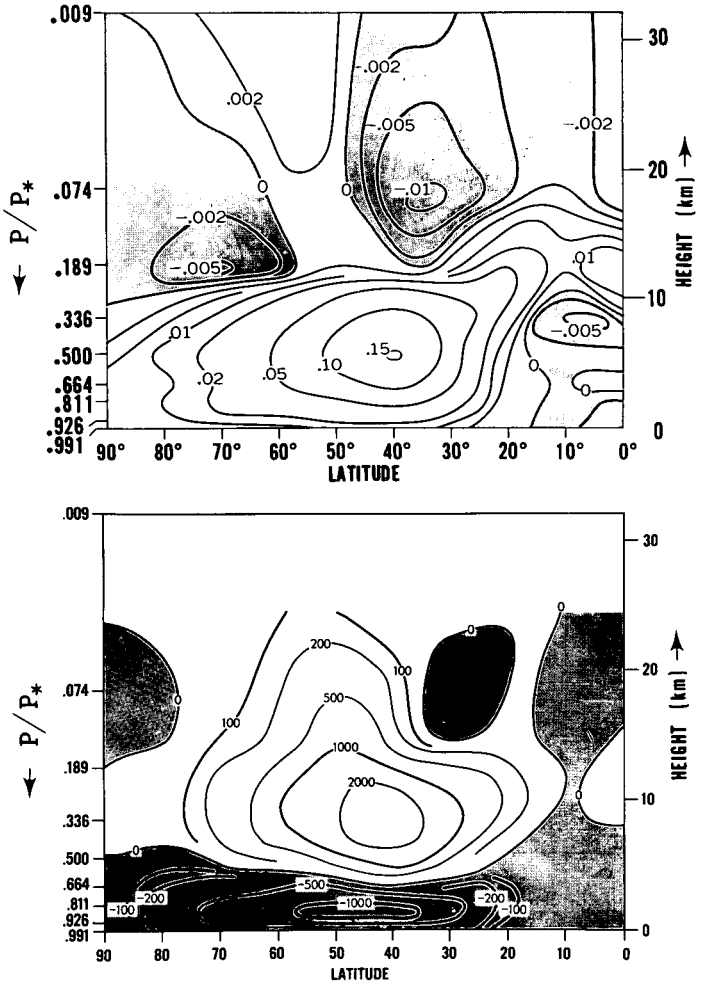

FIGURE 7C4.—The latitude-height distributions of $-\overline{\omega'\alpha'}^H$ (in units of joule cm.$^{-2}$ mb.$^{-1}$ day^{-1}) and that of $-\overline{\omega'\phi'}^H$ (in units of 10^{-2} joule cm.$^{-2}$ day^{-1}) on the isobaric surface are shown in the upper and lower parts of the figure, respectively.

( )'' denotes the deviation from the hemispheric mean. The first term on the right-hand side of equation (7D1) corresponds to the effect of the redistribution of total available potential energy by vertical motion. The third term denotes the net generation of available potential energy caused by the effect of radiation, convection, and horizontal diffusion. (CR) is the extra term which arises from the simplified definition of available potential energy. In general, this term is very small and, therefore, it will be excluded from further discussion.

In the upper part of figure 7D2 are shown the vertical distributions of the net generation of total available potential energy by convection, radiation, and subgrid-scale horizontal mixing. According to this figure, convection generates the available potential energy and radiation and subgrid-scale diffusion destroy it. Figure 7D1 shows that the net generation by these three processes is mostly compensated by the conversion of total available potential energy, i.e., by $\overline{\omega\alpha}^H$. The conversion term has a maximum value at about the 500-mb. level which is somewhat lower than the level of maximum net generation. Vertical transport of A_T adjusts the imbalance between them.

E. ZONAL AND EDDY AVAILABLE POTENTIAL ENERGY BUDGET

The equations for the rate of change of the hemispheric means of A_Z and A_E (see equations 4F2 and 4F3) in a pressure coordinate system may be written as follows:

$$\frac{\partial \overline{A_Z}^H}{\partial t} = -\frac{\partial}{\partial P}\overline{(\omega A_Z)}^H + \overline{\bar{\omega}^\lambda \bar{\alpha}^\lambda}^H + \frac{\gamma}{c_p}\overline{(\bar{T}^\lambda)'' \cdot (\bar{q}^\lambda)''}^H - \overline{\langle A_Z \cdot A_E \rangle}^H + (CRZ) \quad (7E1)$$

$$\frac{\partial A_E}{\partial t}^H = -\frac{\partial}{\partial P}\overline{(\omega A_E)}^H + \overline{\omega'\alpha'}^H + \frac{\gamma}{c_p}\overline{T' \cdot \dot{q}'}^H + \overline{\langle A_Z \cdot A_E \rangle}^H + (CRE) \quad (7E2)$$

where

$$\overline{(A_Z \cdot A_E)}^H = -\gamma\left[\overline{\overline{v'T'}^\lambda \frac{\partial(\bar{T}^\lambda)''}{a\partial\theta}}^H + \overline{\overline{\omega'T'}^\lambda \cdot \left(\frac{\partial(\bar{T}^\lambda)''}{\partial P} + \kappa\frac{(\bar{T}^\lambda)''}{P}\right) - \frac{\partial}{\partial P}\left\{(\bar{T}^\lambda)'' \cdot \overline{\omega'T'}^\lambda\right\}}^H\right] \quad (7E3)$$

$$(CRZ) = \overline{\omega \cdot A_Z}^H \left\{\frac{\partial}{\partial P}\log_e\left[\gamma\left(\frac{T}{\theta}\right)^2\right]\right\} \quad (7E4)$$

and

$$(CRE) = \overline{\omega \cdot A_E}^H \left\{\frac{\partial}{\partial P}\log_e\left[\gamma\left(\frac{T}{\theta}\right)^2\right]\right\} \quad (7E5)$$

The third terms on the right-hand sides of equations (7E1) and (7E2) are the zonal and eddy generation of available potential energy, and $\overline{\langle A_Z \cdot A_E \rangle}^H$ is the conversion

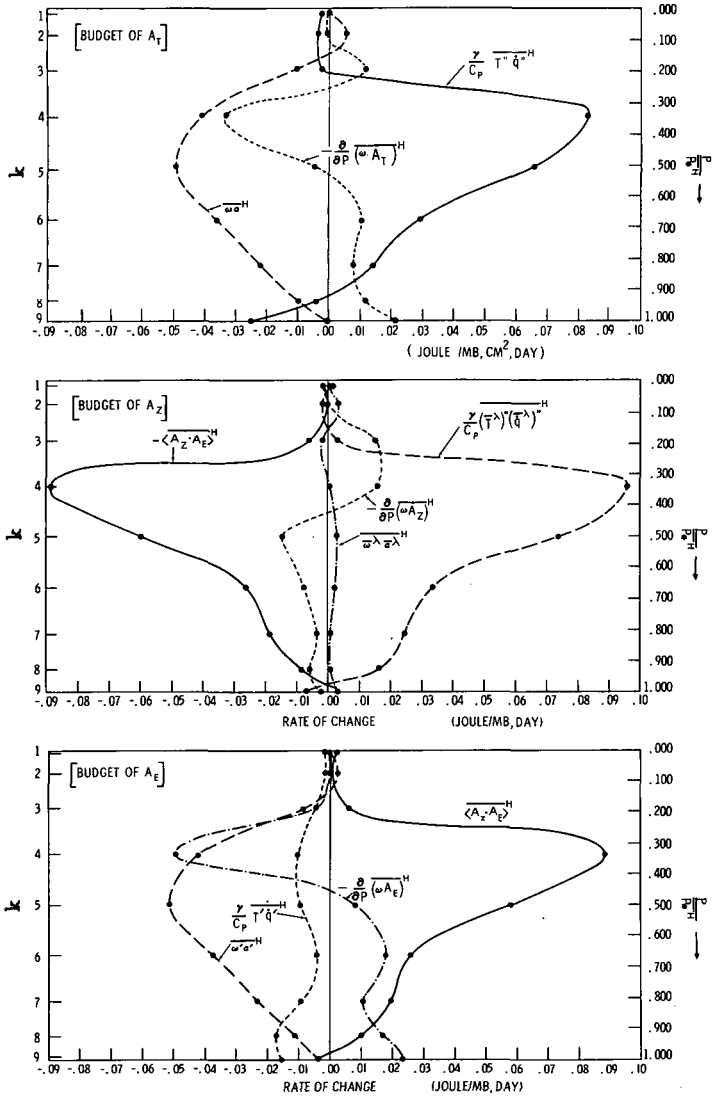

FIGURE 7D1.—The vertical distribution of the budget components of total available potential energy, of zonal available potential energy, and of eddy available potential energy on an isobaric surface are shown in the upper, middle, and lower parts of the figure, respectively.

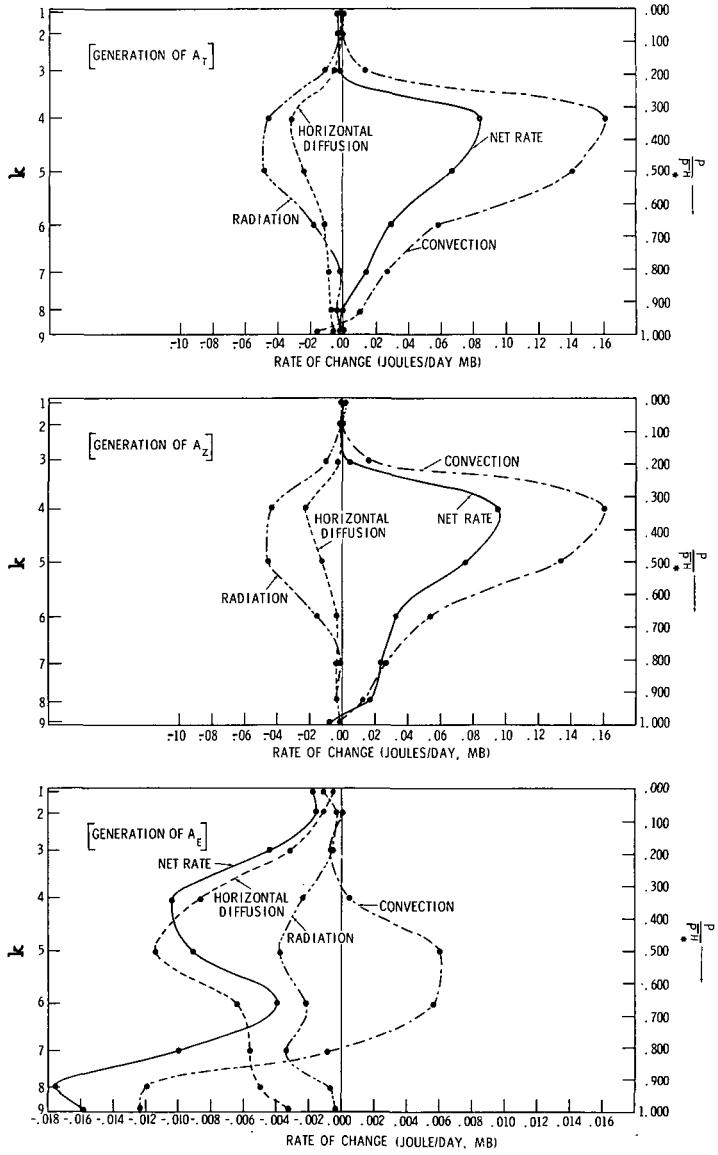

FIGURE 7D2.—The vertical distribution of the generation or destruction of available potential energy due to convection, radiation, and horizontal subgrid-scale mixing. The distributions for the total available potential energy, zonal available potential energy, and eddy available potential energy are shown in the upper, middle, and lower parts of the figure, respectively. Note the change of horizontal scale on the eddy graph.

from zonal to eddy available potential energy. (*CRZ*) and (*CRE*) are terms arising from the assumption adopted for the linearization of the definition of available potential energy. Again, we shall disregard these terms in the following discussion.

According to figure 7D1, the net generation of zonal available potential energy has a maximum in the upper troposphere. This generation is mostly compensated for by the transformation of zonal available potential energy into eddy available potential energy, which is also at a maximum in the upper troposphere. Figure 7D2 shows that the major mechanism which generates the zonal available potential energy is the heating caused by vertical convective mixing (conduction from the earth's surface and moist convective adjustment).

The budget components of eddy available potential energy are shown in figure 7D1. According to this figure the energy supply from the zonal available potential energy constitutes a major source of eddy available potential energy. On the other hand, major sinks are the transformation into eddy kinetic energy and the net destruction by radiation, convection, and horizontal diffusion. Figure 7D2 shows that the convective adjustment destroys some of the eddy available potential energy near the earth's surface. The vertical transport of A_E (see equation 4F3) compensates for the height difference between the level of maximum supply and that of maximum loss.

Because the latitudinal temperature gradient is too large in the upper troposphere of our model, the sharp maximum of energy transfer between zonal available potential energy and eddy available potential energy in the upper troposphere may be exaggerated in our calculation. The general qualitative features of the energy budget described above, however, may not be too far from reality. It would be desirable to carry out a similar study of the vertical distribution of energy budget for the real atmosphere.

F. ENERGY BALANCE OF THE STRATOSPHERE

In order to investigate the energetics of the stratosphere obtained from our model, we constructed energy diagrams for a stratospheric layer (P/P_*=0.034 to 0.126, i.e., the second layer from the top). Figure 7F1 shows the two-box energy diagram. The terms which are written outside the domain enclosed by dashed lines represent the interaction with other layers. Since the interaction between the second layer and the lower layer is much larger than that between the second layer and the top layer, we may regard these terms outside the domain as the interaction between this stratospheric layer and the lower layers of the atmosphere. According to this figure, the energy transfer from below is mainly accomplished by the pressure interaction term $-\overline{\omega\phi}^H$. This energy supply counterbalances the loss of kinetic energy by the conversion from kinetic energy to potential energy and by dissipation. The available potential energy thus converted from kinetic energy is destroyed by the subgrid-scale thermal diffusion and by radiation. These results are in qualitative agreement with the conclusion obtained by Barnes [2], Miyakoda [21], and Oort [24] for the actual atmosphere.

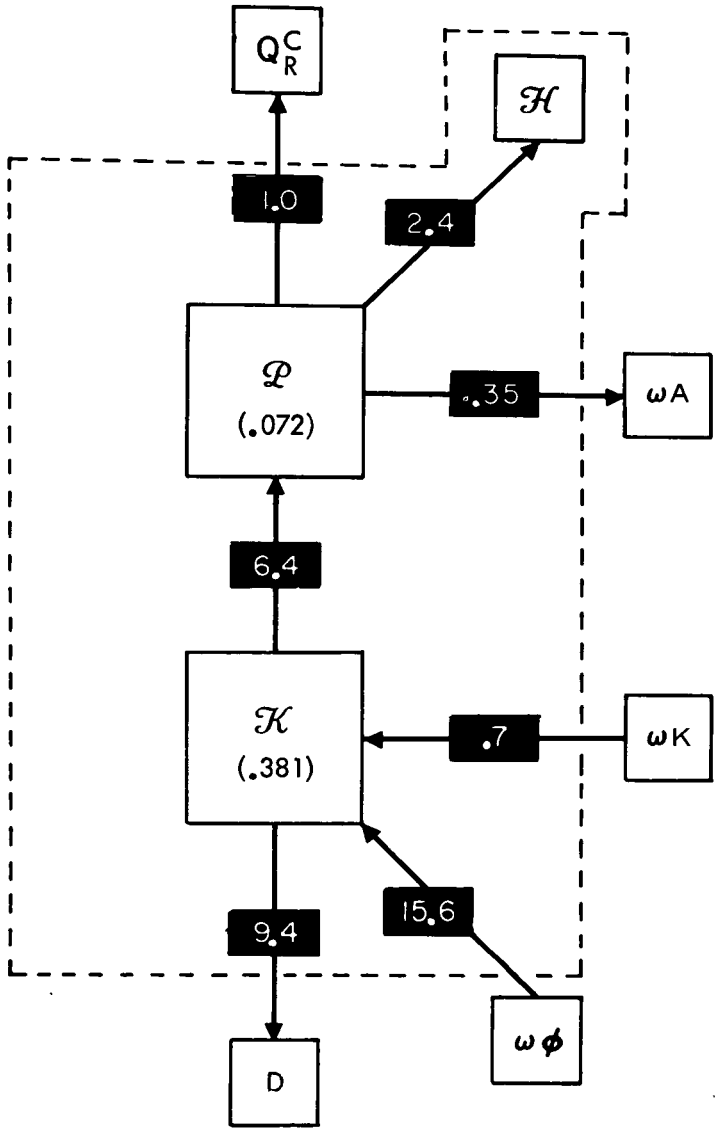

FIGURE 7F1.—Two-box energy diagrams for the model stratosphere (approximately the 34–126-mb. layer). Q_R^C, generation of available potential energy due to radiation and convection from the earth's surface. ωA, the effect of the vertical transport of available potential energy. ωK, the effect of vertical transport of kinetic energy. $\omega\phi$, effect of the pressure interaction term. The unit of energy transformation is 10^{-3} joule mb.$^{-1}$ cm.$^{-2}$ day^{-1} and the unit of energy itself is joule cm.$^{-2}$ mb.$^{-1}$. For further explanation refer to figure 7A1. NOTE: Value of $\mathcal{P}_Z$ should be .064 instead of .072.

In order to compare our results with the energy diagram obtained by Oort [24] for the actual atmosphere, a four box energy diagram is shown in figure 7F2 together with the diagram of Oort [24]. According to this diagram, the eddy kinetic energy of the stratosphere is supplied by the lower atmosphere through the eddy pressure interaction term. The eddy kinetic energy thus produced is trans-

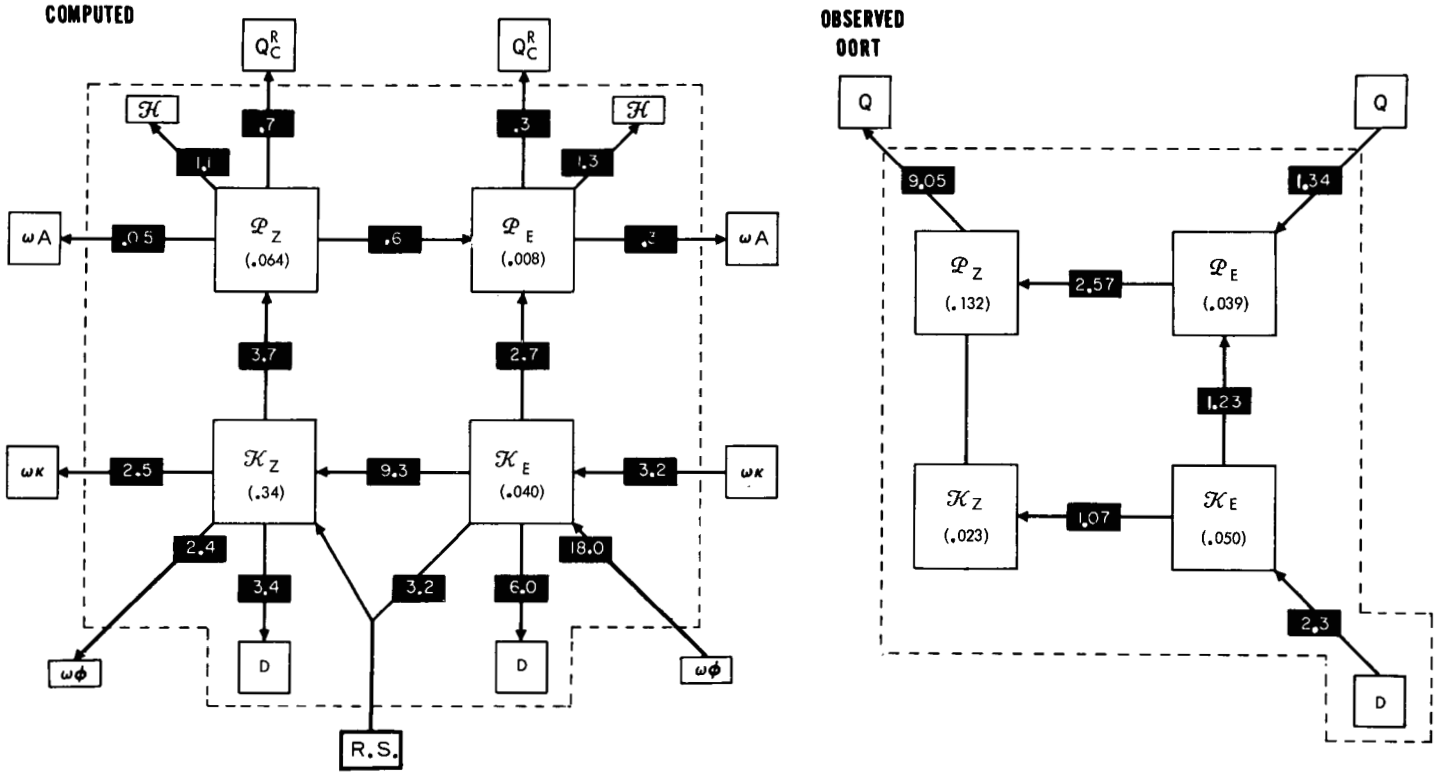

FIGURE 7F2.—Four-box energy diagram for the stratosphere of the model atmosphere (approximately 34–126-mb. layer) and of the actual atmosphere (30–100-mb. layer) as compiled by Oort [24] are shown in the left and right-hand sides of the figure, respectively. The energy exchange with the other layers of the atmosphere is shown by extending the arrow outside the domain enclosed by the dashed line. R.S.=the mass integral of the Reynolds stress term $<K_Z \cdot K_E>_2$ (see equation (7C6).). The unit of energy transformation is 10^{-3} joule mb.$^{-1}$ cm.$^{-2}$ day^{-1}, and the unit of energy itself is joule cm.$^{-2}$ mb.$^{-1}$ For further explanation, refer to figures 7A1 and 7F1. NOTE: value of $\mathcal{P}$ should be .056 instead of .064.

ferred into zonal kinetic energy and then into the zonal available potential energy. The transfer of energy described so far is in qualitative agreement with the results of Oort [24] obtained for the actual atmosphere. Quantitatively, the magnitude of the eddy pressure interaction from the lower atmosphere and that of energy exchange between zonal and eddy kinetic energy are much larger for our model atmosphere than for the actual atmosphere. There are other disagreements. According to this diagram, small amounts of zonal available potential energy are transferred into eddy available potential energy, in qualitative disagreement with the results Oort [24] obtained for the actual atmosphere. Also, the degree of destruction of zonal available potential energy by radiation is much smaller than that for the actual atmosphere.

These comparisons suggest that the energy cycle in the model stratosphere is significantly different from, at least, Oort's results for the stratosphere despite some qualitative similarity. In order to simulate the stratosphere more realistically, the following improvements of the model are being planned:

(1) Improvement of vertical resolution of the model in the neighborhood of the tropopause. This improvement may enable us to represent the vertical variation of the pressure interaction term more accurately.

(2) Incorporation of the effect of condensation. This improvement may significantly alter the meridional temperature gradient of the atmosphere and therefore change the magnitude of the zonal kinetic energy in the stratosphere as well as in the troposphere.

(3) Incorporation of the seasonal variation of radiation. Since the condition of the stratosphere varies drastically from one season to another, it is essential to include this effect for the successful simulation of the climatology of the stratosphere.

8. CONCLUDING REMARKS

In this study, we achieved a reasonable degree of success in simulating the vertical structure of the atmosphere by adopting a model with a relatively high vertical resolution. The general thermal structure of stratosphere-troposphere system is simulated. The pole-to-equator difference in the height of the tropopause turned out to be approximately 7 km., which is reasonably close to the observed difference of 10 km. The latitude of the tropospheric jet coincides with the observation. The general features of the distributions of radiative flux and convective flux are very similar to what London obtained for the actual atmosphere. Also, the characteristic features of wave disturbance are successfully simulated. The wave

number of these disturbances decreases very sharply with increasing altitude around the level of the tropopause, and very long waves predominate in the stratosphere. The level of maximum eddy kinetic energy is around the 200-mb. level and coincides with the level of maximum in the actual atmosphere. The vertical distribution of the budget of kinetic energy is in qualitative agreement with the recent results of analyses of the actual atmosphere. For example, the kinetic energy of our model stratosphere is maintained by the supply of energy from the troposphere through the pressure interaction term in agreement with the results obtained by analysis of the actual atmosphere.

On the other hand, there are many discrepancies between our model atmosphere and the actual atmosphere. Many of the discrepancies pointed out by Phillips [27] and Smagorinsky [37] in their numerical experiments are still present. For example, the ratio of eddy kinetic energy to the zonal kinetic energy and that of eddy available potential energy to its zonal value are much smaller for our model atmosphere than for the actual atmosphere. Also, the latitudinal gradient of temperature of our model in middle latitudes is much larger than the observed gradient. Accordingly, the intensity of the jet stream which we obtained from our model is much too strong.

In the stratosphere, the latitudinal increase of temperature with increasing latitude is insufficient. Thus, the stratospheric westerlies of our model atmosphere turned out to be much stronger than the observed annual mean. The amount of energy supplied from the troposphere into the stratosphere also seems to be much larger for the model than for the actual atmosphere. The eddy kinetic energy created by this energy supply is used to maintain the very large zonal kinetic energy of our model stratosphere. These features of the stratosphere obtained from our computation are much closer to those of the winter stratosphere than to those of the annual mean stratosphere despite the fact we adopted the annual mean insolation for our computation.

One of the major factors which may be responsible for these discrepencies is that the condensation process in the atmosphere is missing in the model. For example, the modification of the latitudinal distribution of heating by condensation could alter significantly the temperature gradient in middle latitudes and accordingly the intensity of the zonal current. Recently, we have completed a preliminary integration of the general circulation model which includes a simple hydrologic cycle. The comparative result is discussed in a companion paper [18].

Also, the effects of the asymmetries of the lower boundary such as mountains and land-sea distribution could be important. Recently, Mintz [20] successfully similated the longitudinal as well as latitudinal distributions of temperature and pressure at the earth's surface by incorporating these effects. As we discussed already, they may significantly increase the ratio of eddy to zonal kinetic energy.

Another factor of importance is the horizontal and vertical resolution of the model. According to the preliminary results of an integration of our model with higher horizontal resolution ($N=40$), the magnitude of the northward transport of total energy (or momentum) due to the meridional circulation and that due to the large-scale eddies are significantly different from the results obtained from the present model ($N=20$). Recently, Smagorinsky and staff members [38] performed a series of forecast experiments with real initial data and concluded that the increase of resolution greatly improves their forecasts. Therefore, it seems mandatory to perform experiments with greater resolution; otherwise, the quantitative comparison of our results with the features of the actual atmosphere will be of limited value.

In this study, a great deal of effort is devoted to the analysis of the budget of kinetic energy of our model atmosphere. We attempted to show how the kinetic energy of the jet stream, the large eddy kinetic energy in the upper troposphere, and the kinetic energy of the stratosphere are maintained against dissipation. Although some of the results we obtained are in qualitative agreement with analyses of observed data, further study of the budget of kinetic energy of the actual atmosphere is needed for the satisfactory verification of simulation.

Finally, it must be pointed out that part of the success in simulating the atmosphere is due to the fact that we adopted the climatological distribution of atmospheric absorbers for the computation of radiative transfer. It is a further goal of our study to perform the numerical integration without assuming the climatological distribution of water vapor, ozone, and clouds.

APPENDIX I.—FINITE DIFFERENCE EQUATIONS

A. SPACE DIFFERENCE

The finite difference representation of the non-linear term, which satisfies some of the integral requirements of inertia terms and avoids some of the possibilities of nonlinear instability (pointed out by Phillips [29]) was recently proposed by Arakawa [1]. Basing it upon the same principle, Lilly[7] proposed a general energy and momentum conserving representation of the non-linear term which we adopted for the present study.

In order to facilitate the display, we shall first define the following sum and difference operators adopted by Shuman and Vanderman [36] and Lilly [13].

$$\delta_X\phi=\left[\phi\left(X+\frac{\Delta}{2}\right)-\phi\left(X-\frac{\Delta}{2}\right)\right] \qquad \text{(AI1)}$$

$$\bar{\phi}^X=\frac{1}{2}\left[\phi\left(X+\frac{\Delta}{2}\right)+\phi\left(X-\frac{\Delta}{2}\right)\right] \qquad \text{(AI2)}$$

where ϕ is any function of the variable X. For example, the notation $\bar{\phi}^Q$ signifies that the value of ϕ at the adjacent levels is averaged.

[7] Personal communication.

Error

An error occurred while processing this page. See the system log for more details.

(MTQ) and (STQ) are torque due to mountains and surface drag, respectively. θ, ϕ_* and $(\tau_{XZ})_{Q=1}$ denote latitude, the geopotential of the earth's surface, and the surface stress respectively. In the present computation (MTQ) is zero.

C. AVAILABLE POTENTIAL ENERGY

According to Lorenz [15], the available potential energy can be defined as follows

$$\mathfrak{A}=(E+I)-(\tilde{E}+\tilde{I}) \qquad \text{(AII8)}$$

where E and I denote potential and internal energies respectively. The operator $\sim$ denotes the quantities which would be obtained after redistributing the atmosphere until the isentropic surfaces are horizontal. The equation describing the change of available potential energy is

$$\frac{\partial \mathfrak{A}}{\partial t}=-C+G \qquad \text{(AII9)}$$

where

$$C=-\int\left(\int_0^1 \frac{P_*}{g}\,\omega\alpha\, dQ\right)dA-\int\left(\frac{\phi_*}{g}\frac{\partial P_*}{\partial t}\right)dA \qquad \text{(AII10)}$$

$$G=\int\left(\int_0^1\left[1-\left(\frac{\tilde{P}}{\bar{P}}\right)^{\kappa}\right](\dot{q}_{RAD}+\dot{q}_{HD}+\dot{q}_{CV})\frac{P_*}{g}\,dQ\right)dA - \int\frac{\phi_*}{g}\frac{\widetilde{\partial P_*}}{\partial t}\,dA \qquad \text{(AII11)}$$

G is the net generation of available potential energy by radiative heating $\dot{q}_{RAD}$, by convection $\dot{q}_{CV}$, and by $\dot{q}_{HD}$, which is the equivalent heat source corresponding to the effect of horizontal diffusion. Second terms on the right-hand side of the equations (AII10) and (AII11) are zero in the present computation because of the lack of mountains.

D. GROSS STATIC STABILITY

Modifying slightly the definition given by Lorenz, we can define static stability of the atmosphere as follows

$$\mathcal{G}=-(E+I)+(\tilde{\tilde{E}}+\tilde{\tilde{I}}) \qquad \text{(AII12)}$$

where $\approx$ denotes the quantities of the idealized atmosphere whose potential temperature is constant everywhere and whose mean potential temperature is equal to that of the actual atmosphere.

The equation describing the change of gross static stability of the atmosphere is

$$\frac{\partial \mathcal{G}}{\partial t}=C-GG \qquad \text{(AII13)}$$

where GG is the net rate of destabilization of the gross static stability of the atmosphere by $\dot{q}_{RAD}$, $\dot{q}_{CV}$, and $\dot{q}_{HD}$, and is represented by the following equation

$$GG=\int\left(\int_0^1\left[1-\frac{1}{1+\kappa}\frac{\int\tilde{\tilde{P}}_*^{1+\kappa}dA}{\left(\int P_* dA\right)P^{\kappa}}\right](\dot{q}_{RAD}+\dot{q}_{CV}+\dot{q}_{HD})\frac{P_*}{g}\,dQ\right)dA-\int\frac{\phi_*}{g}\frac{\partial\tilde{\tilde{P}}_*}{\partial t}\,dA \qquad \text{(AII14)}$$

Again, the second term on the right-hand side of the equation is zero in the present calculation.

APPENDIX III.—SUBGRID-SCALE MIXING COEFFICIENT

The coefficient of diffusion K_H in the subgrid-scale mixing used in the model is computed from the relation:

$$K_H=2k_0^2\left(\frac{\Delta}{2m}\right)^2|D|$$

where the notation is that of section 2(B). The only factor in this equation not exactly specified by the theory is the Karman constant k_0. We used a value of 0.4 in the long-time integration reported on here. However, we performed extensive test integrations using a simple two-level stereographic model with four values of k_0 around 0.4 to make sure we adopted a reasonable value for this parameter. The simplified model was essentially the same as used in the general circulation experiment except for modifications to the surface drag and convective adjustment made necessary because of the low resolution in the vertical. A simple parametric heating function was used instead of the explicit radiation computation of the regular nine-level model.

The model was started from rest and an isothermal state and run with $k_0=0.4$ until a more-than-adequate pole-to-equator temperature gradient had developed and baroclinic waves were beginning to form. Then an arbitrary time step was chosen as an initial condition, and the model was run 11 days beyond this point four times with four different values of k_0 (0.2, 0.283, 0.4, and 0.566) but with no other changes.

After 11 days an inspection of the maps of winds, pressure, and temperature indicated that those computed with $k_0=0.4$ exhibited the best compromise between too much "noodling" in small-scale features and too little development of baroclinic waves. Space does not permit the printing of all the maps that contributed to this decision, but figure A-III shows cross-sections of temperature and meridional wind at the top level (250 mb.) along a great circle passing through the North Pole. Certainly it is clear from these curves that $k_0=0.566$ gives too much smoothing and $k_0=0.2$ not enough. However, whether $k_0=0.4$ is the optimum value is still in doubt, but this value was chosen for the longtime integration because of its historical precedent.

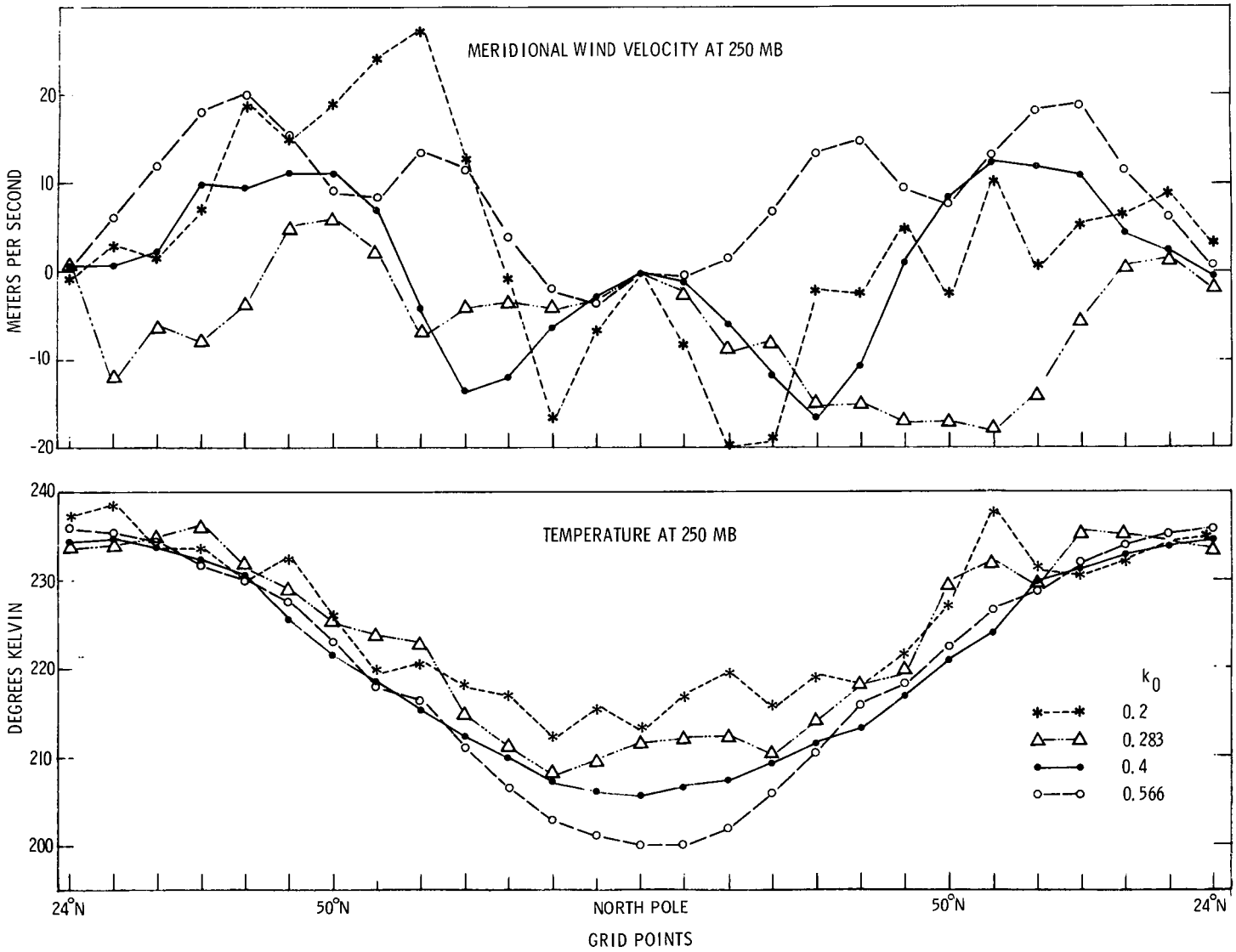

FIGURE A–III.—Cross-sections of meridional wind and temperature at 250 mb. along a great circle passing through the North Pole computed in a simple two-level baroclinic model solved on a stereographic projection. Four runs of 11 days each were made in which the only difference in the model was the value of the Karman constant (k_0) used in the horizontal diffusion of momentum and heat. These four values were 0.2 (short-dashed curves with stars), 0.283 (dash-dotted curves with triangles), 0.4 (solid curves with solid circles), and 0.566 (long-dashed curves with open circles).

ACKNOWLEDGMENTS

The research reported on here was such a large undertaking that it could only have been accomplished by extraordinary teamwork on the part of a great number of talented and conscientious workers. It would be utterly impossible in a few words to acknowledge properly the superlative assistance we have received during the preparation of this paper.

We are especially indebted to Dr. Patrick H. Sterbenz, Dr. Donald A. Quarles, Jr., Dr. Kurt Spielberg, and other members of the Mathematics and Applications Department of the I.B.M. Corporation for planning and writing the original machine-language STRETCH computer program for the time integration.

The following present or former members of the Geophysical Fluid Dynamics Laboratory staff contributed substantially to the success of this project: Mr. Robert F. Strickler who provided very knowledgeable assistance with the radiation codes and related phases of the program; Mrs. W. M. Carlton and Mrs. E. A. Staley who gave meticulous attention to details in the systems programing; Mrs. C. J. Hiland and Mrs. E. C. Arnold who wrote the extensive diagnostic programs for analysis of our results; Dr. Kirk Bryan whose many useful questions and suggestions influenced the course of our research a great deal; Dr. Douglas Lilly who developed the modified version of the energy-conserving system of equations suitable for our model; Drs. Yoshio Kurihara and Kikuro Miyakoda who made many useful suggestions regarding numerical techniques and methods of analysis; Mr. J. M. Kennedy who programed small models for test computations described in the Appendix; Mr. John Young who assisted with the formulation of the energy integrals; Mr. H. H. Engelbrecht and his computer operators who worked around the clock expertly running our machine programs; Mrs. Marylin Varnadore who made very accurate and fast hand calculations and data analysis; Mr. R. D. Graham who handled the innumerable administrative details which a project of this size

encounters; and Mrs. J. A. Snyder and Mr. E. W. Rayfield who assisted with the preparation of the manuscript and figures, respectively.

Finally, we are indebted to Dr. Sidney Teweles of ESSA for kindly supplying the results of harmonic analyses of the wind.

REFERENCES

1. A. Arakawa, "Computational Design for Long Term Numerical Integrations of the Equations of Atmospheric Motion," Paper presented at 44th Annual Meeting, American Geophysical Union, Washington, D.C., Apr. 1963.
2. A. A. Barnes, Jr., "Kinetic and Potential Energy Between 100 mb and 10 mb during the First Six Months of the IGY," *Final Report*, Contract No. AF 19(604)-5223, Planetary Circulation Project, Dept. of Meteorology, Massachusetts Institute of Technology, 1963, pp. 8-131.
3. D. Brunt, "Energy in the Earth's Atmosphere," *Philosophical Magazine*, vol. 7, No. 1, 1926, pp. 523-532.
4. H. S. Buch, "Hemispheric Wind Conditions During the Year 1950," *Final Report*, Part 2, Contract No. AH 19-122-153, General Circulation Project, Dept. of Meteorology, Massachusetts Institute of Technology, 1954, 126 pp.
5. J. G. Charney and J. Pedlosky, "On the Trapping of Unstable Planetary Waves in the Atmosphere," *Journal of Geophysical Research*, vol. 68, No. 24, Dec. 15, 1963, pp. 6441-6442.
6. P. A. Davis, "An Analysis of the Atmospheric Heat Budget," *Journal of the Atmospheric Sciences*, vol. 20, No. 1, Jan. 1963, pp. 5-22.
7. H. G. Houghton, "On the Annual Heat Balance of the Northern Hemisphere," *Journal of Meteorology*, vol. 11, No. 1, Jan. 1954, pp. 1-9.
8. C. E. Jensen, "Energy Transformation and Vertical Flux Processes Over the Northern Hemisphere," *Journal of Geophysical Research*, vol. 66, No. 4, Apr. 1961, pp. 1145-1156.
9. J. S. Kennedy, "Energy Generation Through Radiative Processes in the Lower Stratosphere," Report No. 11, Contract AT(30-1)2241, Dept. of Meteorology, Massachusetts Institute of Technology, 1964, 116 pp.
10. A. Kochanski, "Cross Sections of the Mean Zonal Flow and Temperature along 80°W," *Journal of Meteorology*, vol. 12, No. 2, Apr. 1955, pp. 95-106.
11. A. F. Kreuger, J. S. Winston, and D. A. Haines, "Computation of Atmospheric Energy and Its Transformation for the Northern Hemisphere for a Recent Five-Year Period," *Monthly Weather Review*, vol. 93, No. 4, Apr. 1965, pp. 227-238.
12. E. C. Kung, "A Preliminary Study of the Kinetic Energy Dissipation in the Large-Scale Atmospheric Circulation," (Paper in preparation.)
13. D. K. Lilly, "On the Computational Stability of Numerical Solutions of Time-Dependent Non-Linear Geophysical Fluid Dynamical Problems," *Monthly Weather Review*, vol. 93, No. 1, Jan. 1965, pp. 11-26.
14. J. London, "A Study of the Atmospheric Heat Balance," *Final Report* on Contract AF19(122)-165 (AFCRC-TR-57-287), Dept. of Meteorology and Oceanography, New York University, July 1957, 99 pp.
15. E. N. Lorenz, "Available Potential Energy and the Maintenance of the General Circulation," *Tellus*, vol. 7, No. 2, May 1955, pp. 157-167.
16. S. Manabe and F. Möller, "On the Radiative Equilibrium and Heat Balance of the Atmosphere," *Monthly Weather Review*, vol. 89, No. 12, Dec. 1961, pp. 503-532.
17. S. Manabe and R. F. Strickler, "On the Thermal Equilibrium of the Atmosphere with Convective Adjustment," *Journal of the Atmospheric Sciences*, vol. 21, No. 4, July 1964, pp. 361-385.
18. S. Manabe, J. Smagorinsky, and Robert F. Strickler, "Physical Climatology of a General Circulation Model with a Hydrologic Cycle," *Monthly Weather Review*, vol. 93, No. 12, December 1965, pp. 769-798.
19. Y. Mintz and J. Lang, "A Model of the Mean Meridional Circulation," *Final Report*, AF 19(122)-48, General Circulation Project, University of California at Los Angeles, Paper No. VI, 1955.
20. Y. Mintz, "Very Long-Term Global Integration of the Primitive Equations of Atmospheric Motion," *WMO Technical Note* No. 66, "WMO-IUGG Symposium on Research and Development Aspects of Long Range Forecasting, Boulder, Colo., 1964," Geneva, 1965, pp. 141-167.
21. K. Miyakoda, "Some Characteristic Features of Winter Circulation in the Troposphere and Lower Stratosphere," Technical Report No. 14 to National Science Foundation (Grant NSF-GP-471), Dept. of Geophysical Sciences, The University of Chicago, Dec. 1963.
22. G. O. P. Obasi, "Poleward Flux of Atmospheric Angular Momentum in the Southern Hemisphere," *Journal of the Atmospheric Sciences*, vol. 20, No. 6, Nov. 1963, pp. 516-528.
23. G. Ohring, "The Radiation Budget of the Stratosphere," *Scientific Report* No. 1, Contract AF19(604)-1738, Dept. of Meteorology and Oceanography, New York University, June 1957, 42 pp.
24. A. H. Oort, "On the Energetics of the Mean and Eddy Circulations in the Lower Stratosphere," *Tellus*, vol. 16, No. 4, 1964, pp. 309-327.
25. A. H. Oort, "On Estimates of the Atmospheric Energy Cycle," *Monthly Weather Review*, vol. 92, No. 11, Nov. 1964 pp. 483-493.
26. J. P. Peixoto, "Hemispheric Temperature Conditions During the Year 1950," *Scientific Report* No. 4, Contract AF19(604)-2242, Dept. of Meteorology, Massachusetts Institute of Technology, 1960, 211 pp.
27. N. A. Phillips, "The General Circulation of the Atmosphere: A Numerical Experiment," *Quarterly Journal of the Royal Meteorological Society*, vol. 82, 1956, pp. 123-164.
28. N. A. Phillips, "A Coordinate System Having Some Special Advantages for Numerical Forecasting," *Journal of Meteorology*, vol. 14, No. 2, Apr. 1957, pp. 184-185.
29. N. A. Phillips, "An Example of Non-Linear Computational Instability," *The Atmosphere and the Sea in Motion*, Rockefeller Institute Press in Association with Oxford University Press, New York, 1959, pp. 501-504.
30. N. A. Phillips, "Numerical Integration of the Primitive Equations on the Hemisphere," *Monthly Weather Review*, vol. 87, No. 9, Sept. 1959, pp. 109-120.
31. C. H. B. Priestley, "A Survey of the Stress Between the Ocean and Atmosphere," *Australian Journal of Scientific Research*, Ser. A, vol. 4, No. 3, Sept. 1951, pp. 315-328.
32. R. J. Reed, J. L. Wolfe, and H. Nishimoto, "A Spectral Analysis of the Energetics of the Stratospheric Sudden Warming of Early 1957," *Journal of the Atmospheric Sciences*, vol. 20, No. 4, July 1963, pp. 256-275.
33. C.-G. Rossby and R. B. Montgomery, "The Layer of Frictional Influence in Wind and Ocean Currents," *Papers in Physical Oceanography and Meteorology*, vol. 3, No. 3, Massachusetts Institute of Technology and Woods Hole Oceanographic Institution, Apr. 1935, 101 pp.
34. B. Saltzman, R. M. Gottuso, and A. Fleisher, "The Meridional Eddy Transport of Kinetic Energy at 500 mb.," *Tellus*, vol. 13, No. 2, May 1961, pp. 293-295.
35. B. Saltzman, "Spectral Statistics of the Wind at 500 mb.," *Journal of the Atmospheric Sciences*, vol. 19, No. 2, Mar. 1962, pp. 195-206.
36. F. Shuman and L. W. Vanderman, "Truncation Errors in

792-517 O--65----6

Numerical Weather Prediction," Paper presented at 45th Annual Meeting, American Geophysical Union, Washington, D.C., Apr. 1961.

37. J. Smagorinsky, "General Circulation Experiments with the Primitive Equations: I. The Basic Experiment," *Monthly Weather Review*, vol. 91, No. 3, Mar. 1963, pp. 99–164.
38. J. Smagorinsky and Staff Members, "Prediction Experiments with a General Circulation Model," *Proceedings* of the International Symposium on Dynamics of Large Scale Processes in the Atmosphere, Moscow, USSR, June 23–30, 1965.
39. V. Starr and R. M. White, "Balance Requirements of General Circulation," *Studies of the Atmospheric General Circulation*, Final Report, Part I, Contract AF19(122)–153, Dept. of Meteorology, Massachusetts Institute of Technology, 1954, pp. 186–242.
40. V. P. Starr and J. M. Wallace, "Mechanics of Eddy Processes in the Tropical Troposphere," Paper sponsored by the Air Force Cambridge Research Laboratory, under Contract Nos. AF 19(604)–6108 and AF 19(628)–2409.
41. S. Teweles, "Spectral Aspects of the Stratospheric Circulation During the IGY," Report No. 8, Planetary Circulation Project, Massachusetts Institute of Technology, 1963, 191 pp.
42. R. M. White and B. Saltzman, "On Conversion Between Potential and Kinetic Energy in the Atmosphere," *Tellus*, vol. 8, No. 3, Aug. 1956, pp. 357–363.
43. A. Wiin-Nielsen, "Some New Observational Studies of Energy and Energy Transformations in the Atmosphere," *WMO Technical Note* No. 66, "WMO–IUGG Symposium on Research and Development Aspects of Long Range Forecasting, Boulder, Colorado, 1964," Geneva, 1965, pp. 177–202.

[*Received August 9, 1965; revised October 18, 1965*]